Universitá degli Studi di Padova

Luca Cirino

Multi-objective shape optimisation of a Transonic Fan Rotor downstream of an S-duct

Dipartimento di Ingegneria Industriale

MSc Aerospace Engineering

MSc Thesis

Academic Year: 2018 - 2019

Supervisors:

Prof. Ernesto Benini

Dr. Timoleon Kipouros

April 2020

Universitá degli Studi di Padova

MSc Aerospace Engineering

MSc Thesis

Academic Year: 2019-2020

Luca Cirino

Multi-objective shape optimisation of a Transonic Fan Rotor downstream of an S-duct

Supervisors:

Prof. Ernesto Benini

Dr. Timoleon Kipouros

April 2020

UNIVERSITÁ DEGLI STUDI DI PADOVA

Abstract

Dipartimento di Ingegneria Industriale

MSc Aerospace Engineering

Multi-objective shape optimisation of a Transonic Fan Rotor downstream of an S-duct

by Luca Cirino

This master's degree thesis aims to optimize a transonic fan following an S-duct through the use of all the tools necessary for an optimization process. Among these I can mainly mention the optimization algorithm, the parameterization framework and the automatic optimization loop based on CFD analysis. Optimization is a way to improve the performance of a generic system and mostly it can be a powerful tool that helps to obtain information on the physical phenomena underlying the observed improvements.

As for the optimization engine, a genetic algorithm was used for multi-objective optimization problems, namely GA. In order to perform the required analysis, an automatic CFD based optimization circuit built around GA was built. Specifically, a dedicated parameterization framework was created for 3D blades. This framework had already been developed and was adapted for the operation of this particular case taken into consideration.

The effectiveness of both the CFD based automatic loop and the parameterization was verified on the multi-objective optimization of the NASA Rotor 67 placed following an S-duct. To better understand the results of the optimization process, a large section has been dedicated to supersonic flows and their behaviour regarding transonic cascade. The results obtained demonstrated the effectiveness of the constructed optimization approach and provided excellent information on the physics of transonic and supersonic flows. In the results obtained it can also be seen how the optimization of NASA Rotor 67 gives better results than expected, despite the flow problems created by the S-duct.

Sommario

"Set-up and run a fan multiply robust design optimisation study" raccoglie la ricerca svolta dall'autore nel periodo di Erasmus Traineeship condotto presso l'Università di Cranfield della durata complessiva di 6 mesi. Il lavoro è stato svolto con una duplice finalità: da un lato sviluppare un algoritmo per l'ottimizzazione multi-obiettivo; dall'altro, utilizzare questo motore di ottimizzazione, accoppiato con strumenti di analisi basati sulla fluidodinamica computazionale (CFD), per studiare l'ottimizzazione di un FAN transonico nell'ambito del "high speed turbomachinery".
Gli algoritmi evolutivi presi in esame per svolgere questa ricerca hanno dimostrato una alta affidabilità e una ottima robustezza nel raggiungimento del "Fronte di Pareto" (i.e., è la soluzione di un problema multi obiettivo), necessitando di contro un numero di valutazioni delle funzioni obiettivo veramente molto elevato, talvolta praticamente impraticabile dal punto di vista industriale. Infatti, quando la CFD è coinvolta per valutare le funzioni obiettivo del sistema in esame, il costo computazionale derivante dall'analisi può diventare il vero e proprio collo di bottiglia dell'intero processo. Infatti, per quanto riguarda lo studio effettuato dall'autore, sono state necessarie diverse semplificazioni al sistema in esame essendo esso veramente complesso.
La tesi è costituita da dieci capitoli. Il primo capitolo ha lo scopo di essere di introduzione generale al problema in questione. Il secondo capitolo è dedicato allo stato dell'arte dei compressori transonici in modo da poter avere chiara la teoria alla base del funzionamento di tali tipi di compressori. Nel terzo capitolo è stata svolta l'analisi della baseline con lo scopo di validare il modello preso in esame. Nel quarto capitolo è riportato lo stato dell'arte per quanto riguarda le S-duct. Nel quinto capitolo è stata riportata la procedura di ottimizzazione svolta per quanto riguarda l'S-duct. Deve essere specificato che la geometria della presa dinamica è stata studiata da Dal Magro, prima, ed è stata successivamente irrobustita da Scaramuzzi. Nel sesto capitolo è stata studiata l'interazione della S-duct ottimizzata sviluppata dalla collaborazione tra Dal Magro e Tridente con la baseline del rotore. Questo è stato riportato in modo da poter avere la base di partenza per valutare il miglioramento dei risultati a seguito del processo di ottimizzazione. Nel settimo capitolo viene riportata una introduzione sia ai modelli genetici visti nell'ottica dell'ottimizzazione, sia alle strategie di ottimizzazione che sono state applicate per migliorare il rotore transonico che rappresenta il caso di interesse

studiato in questa Tesi. Nell'ottavo capitolo viene descritto il loop automatico di ottimizzazione sviluppato dall'autore comprendente il ciclo di ottimizzazione, la parametrizzazione della geometria in esame, i modelli CFD, e tutti gli elementi necessari per garantire robustezza a tale procedura automatica. Nello specifico è stata operata l'ottimizzazione del FAN transonico sviluppato dalla NASA e denominato Rotor 67. Nel nono capitolo vengono riportati i risultati derivanti da processo di ottimizzazione del Rotor 67 connesso al sistema completo comprendente l'S-duct. Nel decimo ed ultimo capitolo sono state riportate le conclusioni tratte da questo periodo di ricerca e i futuri lavori che si potranno svolgere sulla base di questo lavoro.

Acknowledgements

I would like to thank my Italian supervisor Dr. Ernesto Benini and my English supervisor Dr. Timoleon Kipouros to give me the opportunity to work in the challenging field of Design Engineering. This experience has been amazing and their help has been essential. A big thank you to my best friends Andrea, Mattia and Alberto, who made this experience unique.
I would like to express my gratitude to Engr. Giovanni Venturelli, without whom I could not have completed my project in the required time. Finally, a special thanks to my family, who has always supported me, despite the distance.

Contents

List of Figures

List of Tables

Abbreviations

AIP	**A**erodynamics **I**nterface **P**lane
AVDR	**A**xial **V**elocity **D**ensity **R**atio
CDF	**C**umulative **D**istribution **F**unction
CFD	**C**omputational **F**luid **D**ynamics
DOE	**D**esign **O**f **E**xperiments
EA	**E**volutionary **A**lgorithm
E-O	**E**fficiency **O**ptimized
GA	**G**enetic-**A**lgorithm
MOEA	**M**ulti-**O**bjective **E**volutionary **A**lgorithm
MOO	**M**ulti-**O**bjective **O**ptimisation
MOOP	**M**ulti-**O**bjective **O**ptimisation **P**roblem
MOTS	**M**ulti-**O**bjective **T**abu **S**earch
NIPC	**N**on-**I**ntrusive **P**oint-**C**ollocation
NISP	**N**on-**I**ntrusive **S**pectral-**P**rojection
ODE	**O**rdinary **D**ifferential **E**quation
PC	**P**olynomial **C**haos
PDF	**P**robability **D**ensity **F**unction
PR	**P**ressure-**R**atio
RANS	**R**eynolds-**A**veraged **N**avier-**S**tokes **E**quations
SOO	**S**ingle-**O**bjective **O**ptimisation
TPR-O	**T**otal-**P**ressure-**R**atio **O**ptimized

Symbols

I_n	Wiener-Askey polynomial chaos of order n
M_∞, M_1, M_2	Free-stream Mach number, section 1, section 2, respectively
h	Specific enthalpy
R	Universal gas constant
Re	Reynolds number
V_∞	Free-stream velocity
X	General second order random process
c_{θ_1}, c_{θ_2}	Tangential velocity components in the absolute frame of reference
f	Functional relationship between input variable and response
f_{min}	Minimum of the function
F	High-fidelity model response
$F(P)$	Fitness functions vector
G, G_1, G_2	Constraint violation function
$\dot{m}$	Mass flow rate
$\dot{m}_{choke}$	Choking mass flow of a generic design
W	Weighting function
N	Number of basis functions
p_1, p_2	Static pressure at station 1 and 2, respectively
p_1^0, p_2^0	Total pressure at station 1 and 2, respectively
$p()$	Generic spline model
p_{base}, p_{mod}, p_{displ}	Spline of baseline geometry, modified geometry, displacement field
P	Optimization design variables vector
Q	Optimization penalty term

β_∞, β_1, β_2	Flow angle at infinite, section 1, section 2, respectively
γ	Specific heat ratio
δ_{ij}	Kronecker delta
Φ	Generic polynomial basis
μ	Mean
Ψ	Hermite polynomial basis
μ	Size of the parents' population
ρ	Density
σ	Standard deviation
ξ	Gaussian standard random variable
ζ	Generic random variable
η_{iso}	Isentropic Efficiency
η_{pol}	Polytropic Efficiency
π_c	Compression Ratio

To Mamma Cristina, Babbo Paolo, all the relatives and my closest friends, my university colleagues and myself...

Chapter 1

Introduction

Modern high-performance aircraft engines require that the compressors operate at very high compression ratios and efficiency. In addition to this, in the latest years efforts have also been made to use engines located inside the aircraft in the civil sector. The reason for all this is that high values of compression ratios are important to reduce weight and size of the engine and also with engine placed inside the plane the frictions are reduced. Thus, both engine costs and operating costs can be reduced. To do this, the aeronautics sector is trying to use transonic compressors. It has also been shown that the use of transonic compressors allows to reduce fuel consumption and increase cruising speed. In fact, a lot of research has been conducted to understand the three-dimensionality of the flow and the structure of the shock waves in the rotors of the transonic compressor.

Many techniques have been developed to improve the compressor performance. Among them, the optimization of the curvilinear stacking and blade sweeping have shown good performance improvement. With the rapid advancement of technology, the increase in power of computers and computational fluid dynamics (CFD), it has finally become possible to apply Navier-Stokes equations to the three-dimensional viscous flow field analysis in turbomachinery. In fact, 3D simulation of a transonic blade was impossible to do with low computing power. The flow in a blade of the transonic compressor is characterized by shock waves. Therefore, the simulation of these blades requires a large number of cells to analyze the flow and obtain plausible results. Recently, research has focused on the complete modification of the blade profile in order to reduce the shock losses, the corner separation in the blade hub, and tip clearance losses.

The aim of this master degree is trying to optimize a transonic compressor blade placed following an S-duct. In particular, the NASA Rotor 67 has been taken into account for the optimization process. Rotor 67 is a rotor with a low-aspect-ratio, and it is the first-stage rotor of a two-stage fan. This work wants to maximize the polytropic efficiency (η_{pol}) and the compression ratio (π_c). The optimization process has been made by changing all the shape of the blade. This choice was made, because the goal was to study all the possibilities of variation of 3D geometry in order to obtain a complete optimization. To do this, the geometry of the Rotor 67 has been discretized in 21 profiles and the blade parameterization is the result of superimposing two deformations: 3D stacking line deformation and 2D profile deformation, each of which is treated independently with B-spline curves. These two deformations are joined together forming the final B-spline surface displacement field.

The genetic algorithm has been used for the optimization. The genetic algorithms are one of the most powerful mechanism for aerodynamic problems, because the GA is able to analyze the whole design space without getting stuck in local minima. Unfortunately, the computational time is very high, in generally for the optimization of the whole blade and in this case the calculation time is even higher because the entire rotor must be studied due to the presence of the S-duct. One way to accelerate the GA is to use the hierarchical GA by using a low-fidelity model for a first optimization. The objective function is evaluated by using less accurate tools, one technique can be reducing the complexity of the analysis or by reducing the weight of the mesh. These models require less computing power, but have a significantly lower accuracy. Each noteworthy individual found on the low fidelity process needs to be reevaluated by the high fidelity process. Consequently, this method should speed up the convergence of the optimization loop. To do this, a coarse mesh and a fine mesh have been used for the optimization of the blade in the first attempt. In this case considered, however, this process did not help much because the low fidelity model does not accurately describe the shock wave dynamics so this model was used only to obtain the correct functioning of the optimization loop. In the second attempt it was therefore chosen to reduce the complexity of the analysis by lowering the iterations. The individuals on the Pareto Front obtained with the least iterations were included in the initial population of the second most accurate optimization. In this way, the simulation time has been reduced. The computer programs used for this optimization process are: Turbogrid to generate the fine mesh and ANSYS CFX for the simulations.

Chapter 2

Literature Review

A propulsion system is "an instrument with which to communicate a thrust to a propelled vehicle". Engines are divided into two families: air-breathing engine and rockets. The main difference is how thrust is produced; in fact, in the former ones the fluid is breathed in from the outside and then, once accelerated, released by the nozzle, instead in the latter ones the fluid is initially stored inside and then exhausted. In the aeronautic sector the air-breathing engine is used and there are several types. Nowadays, the most common and efficient propulsive system is the turbofan, in which a fan is placed upstream of the com- pressor. The fan is a low compression ratio compressor which aims to improve the overall efficiency of the engine. Before proceeding, it is significant to know all the components of engine. The first part is the intake, which has the duty to drive the air to the compressor as either uniform or stable as possible by slowing down the flow speed and by increasing its static pressure. After that, the compressor should provide the right compression to bring the fluid to the combustion chamber, in which there is the injection of the fuel to make the combustion happens. Now, the fluid passes through the turbine to reach the nozzle by which it is expelled generating the thrust.

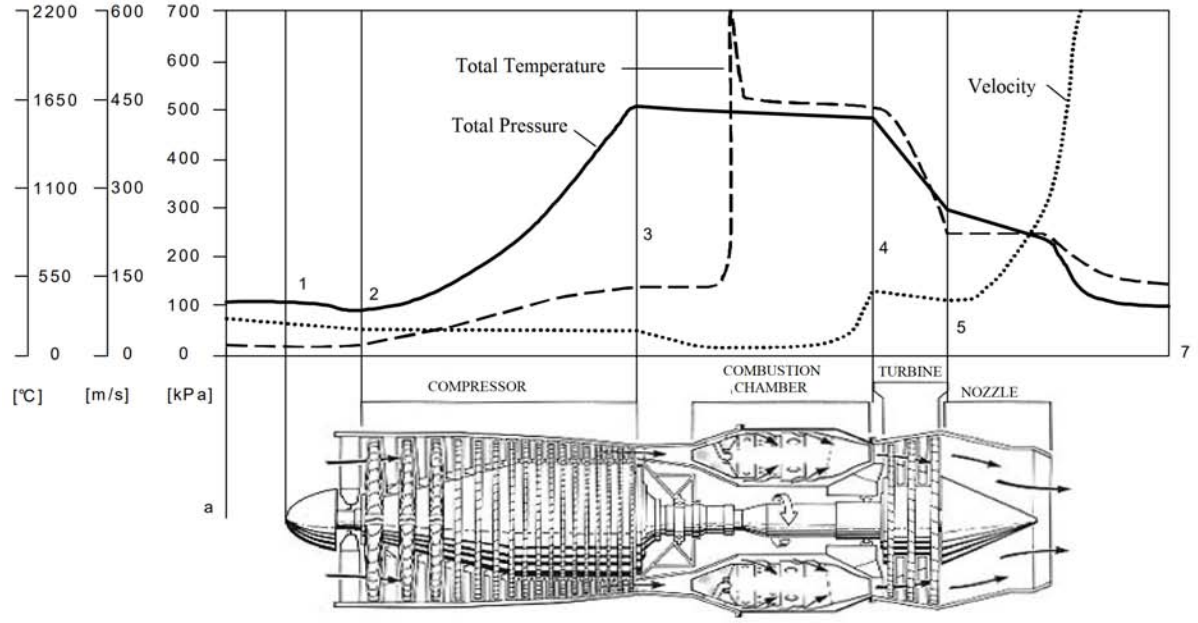

FIGURE 2.1: Properties variation inside a turbojet

The previous figure shows the variation of the various properties inside an aircraft engine. The purpose of this work is the analysis of a fan so we will focus on the turbofan. This is similar to the turbojet, but before the compressor there is the fan and a part of the energy of the turbine is used to move this fan, instead of producing thrust in the nozzle. In this way, the mass flow breathed in increases bringing about a reduction in the specific thrust, but the most significant aspect is that the propulsive efficiency is increased.

2.1 Axial Compressors State-of-Art

As said before, the compressor must increase the pressure of the fluid untill the optimal value for the combustion chamber. Nowadays, in the entire aeronautical sector the axial compressor is used for its ability on working with large mass flow and with high efficiency. As can be understood from the name, the incoming airflow is axial, namely that it is parallel to the axis of rotation. The axial compressor is composed of several stages and each of these in turn consists of two components. The first component is the rotor, which is the moving part of the compressor, and is connected to the central shaft. The second component is the stator which is the static part of the compressor. Its main duty is to straighten up the direction of

the flow and to transform the kinetic energy into static pressure through diffusion. In the following figure all of these features are depicted.

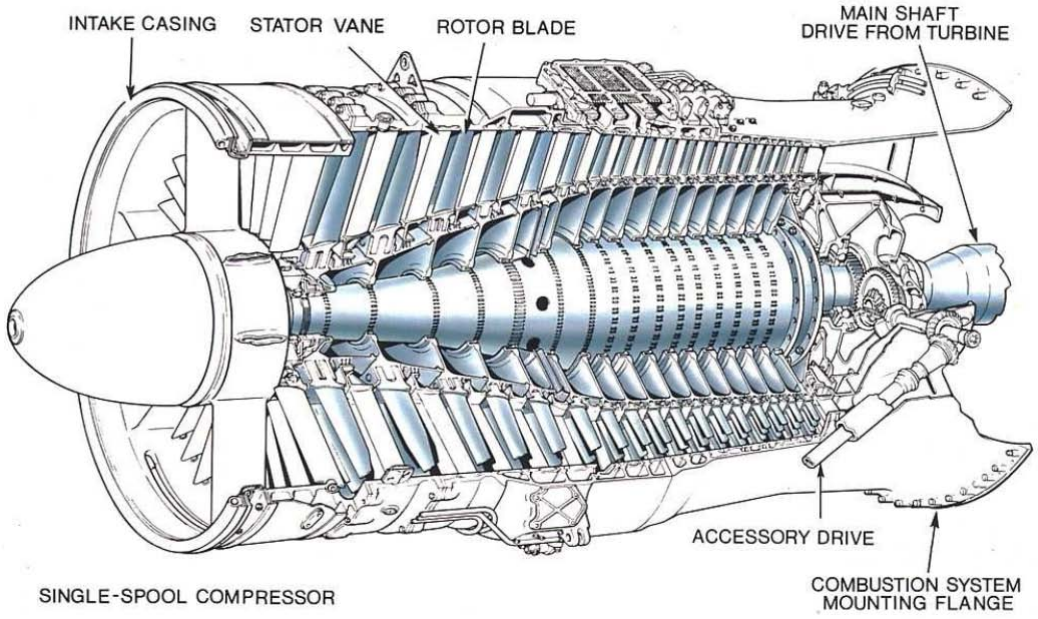

FIGURE 2.2: Sectional view of an axial compressor

In addition to the basic configuration of a compressor, it is possible to use multiple stator arrays, in fact, downstream of the last stage, the use of OGV (Outlet Guided Vanes) could be envisaged for two different reasons:

1. Reduction of the swirl of the fluid before it enters in the channel
2. Structural function for the shell of the engine for the combustion chamber

Furthermore, the use of IGV (Inlet Guide Vanes) is possible at the compressor inlet in order to reduce the relative Mach. Using this component the speed is deviated leaving the axial component constant and decreasing the relative one. In addition, the stacking angle is controlled and varied to improve compressor design performance [2]. All these solutions are generally taken into consideration whenever the number of stages is greater than 5.

2.1.1 Velocity Triangles Theory

The triangles of velocities are usually drawn either to represent the properties of the fluid through the rotor in its system of reference relative and through the stator or to understand how the energy is exchanged within a stage. Generally, the inlet is marked as number 1, the outlet of the rotor as number 2 and the exit of the stage or outlet of the stator as number 3, the behavior of the velocities is shown below, Fig. 2.3.

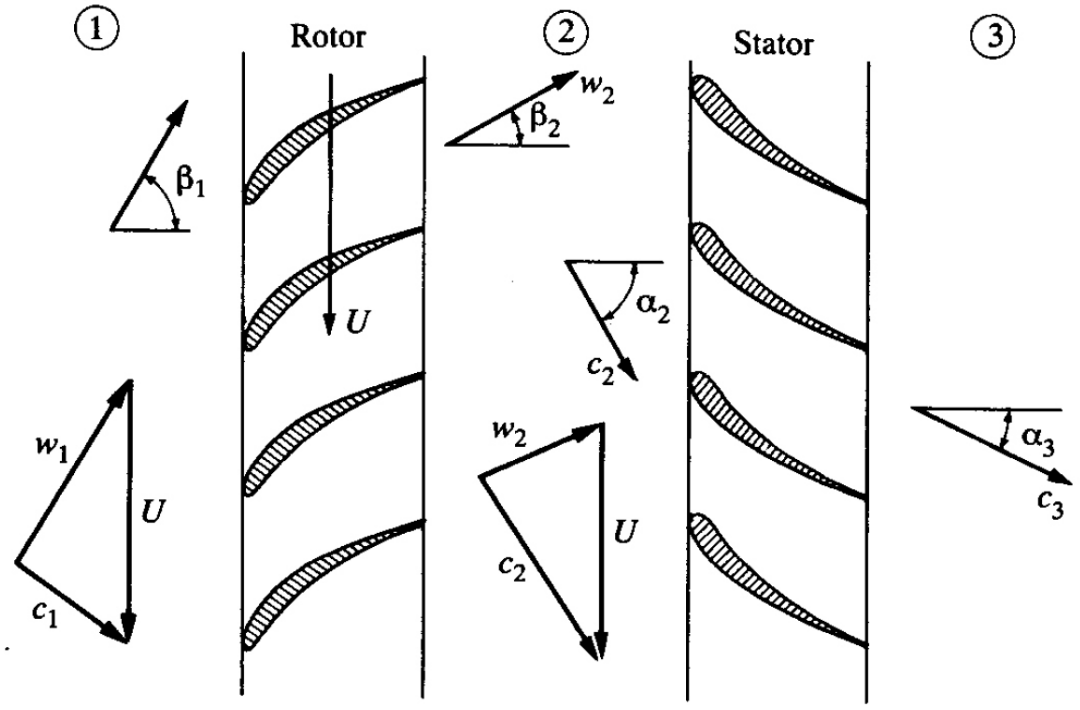

FIGURE 2.3: Triangle of velocities of an axial compressor [1]

The velocities taken into considerations are:

- c absolute flow velocty
- w relative flow velocity
- U tangential blade speed ($U = \omega \wedge r$)

and the relationship between these speed components is:

$$c = w + U \tag{2.1}$$

The Fig. 2.3 is referred to the mean radius of the compressor, but the properties vary similarly for all sections of the blade. Through the rotor the mechanic energy is transformed into fluid enthalpy [2], by bringing about the increase of absolute velocity, static and total temperature. Therefore, as the absolute velocity increases, the relative velocity must decrease to satisfy the equation 2.1 and as a consequence of that the static pressure increases. In the stator blades, instead, the total temperature is conserved, the entire work of the stage is done by the rotor, and the stator's job is to act as a diffuser for the absolute velocity. For that reason, there is only a loss of total pressure due to the friction of the fluid with the blade.

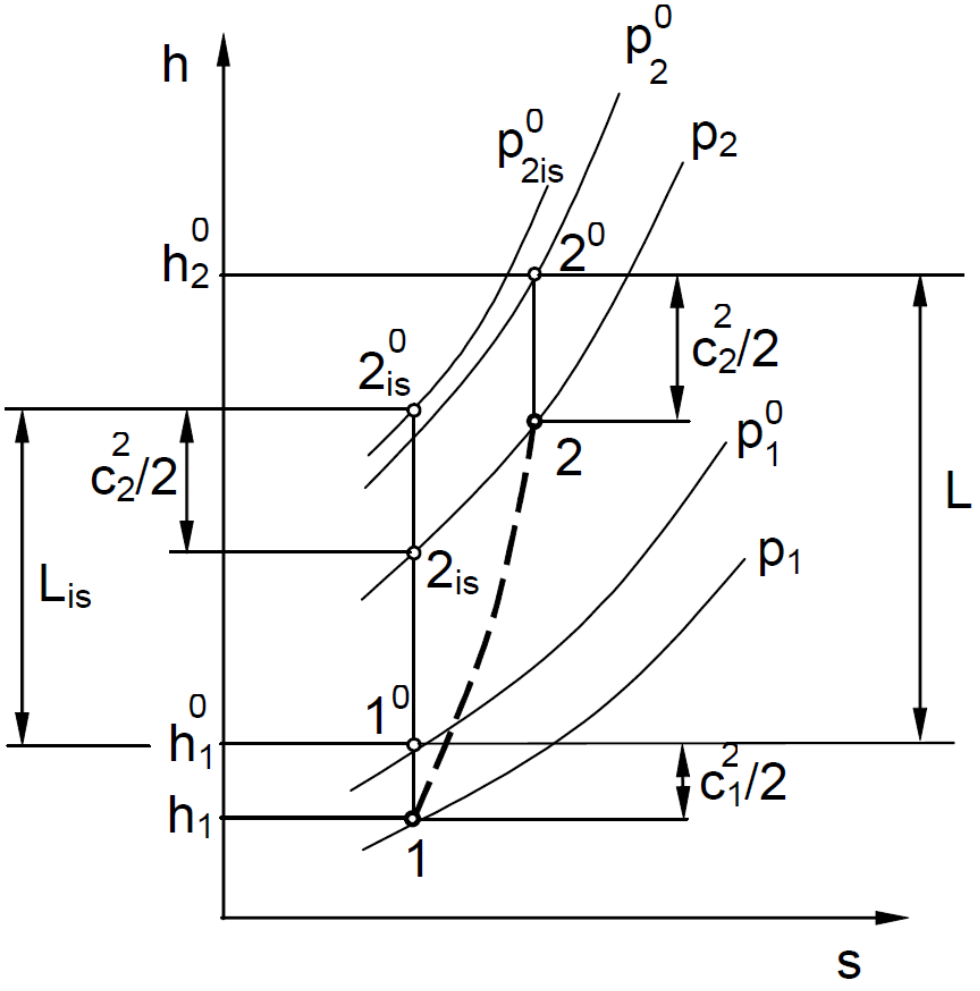

FIGURE 2.4: Thermodynamic properties of a compression process

2.1.2 Isentropic Efficiency

The compression process in the entire compressor must be performed with the greatest possible efficiency, this entails the least absorption of mechanical energy supplied by the shaft [2]. This phenomenon is described from the isentropic efficiency, which is calculated (referring to the compression process of figure 2.4) as:

$$\eta_{is} = \frac{L_{is}}{L} = \frac{h^0_{2is} - h^0_1}{h^0_2 - h^0_1} \tag{2.2}$$

The so defined efficiency in equation 2.2 is defined total-to-total efficiency. There are two ways to describe this property, the first one is the one previously analyzed, whilst the second one is the so-called total-to-static efficiency. What changes is the use of the static enthalpy instead of the total one at the exit. The use of this second form is explained by analyzing the last stage of the compressor the kinetic load is not conserved, it is lost, therefore it does not make sense to use the total form for calculating efficiency.

2.1.3 Polytropic Efficiency

However, the isentropic efficiency is not able to describe carefully how well the compressor works, due to its dependency from the pressure ratio. Due to this link, the previously calculated efficiency decreases as the $\triangle h^0$ increases. Indeed, by looking at Fig. 2.4, the higher the exit temperature is, the higher the real work is and, since it is at the denominator of equation 2.2, the lower the efficiency is. To avoid this problem, another pressure-ratio independent parameter has been studied: the polytropic efficiency. This is defined as the isentropic efficiency of a thermodynamic adiabatic process in which the initial and final pressure present an infinitesimal difference as shown in the following figure.
As shown in the following graph the polytropic efficiency is defined as:

$$\eta_{pol} = \frac{dh_{is}}{dh} = \frac{dp/\rho}{c_p dT} \tag{2.3}$$

which can be easily written in the most-known expression of η_{pol}:

$$\eta_{pol} = \frac{k-1}{k} \frac{ln(\frac{p^0_2}{p^0_1})}{ln(\frac{T^0_2}{T^0_1})} \tag{2.4}$$

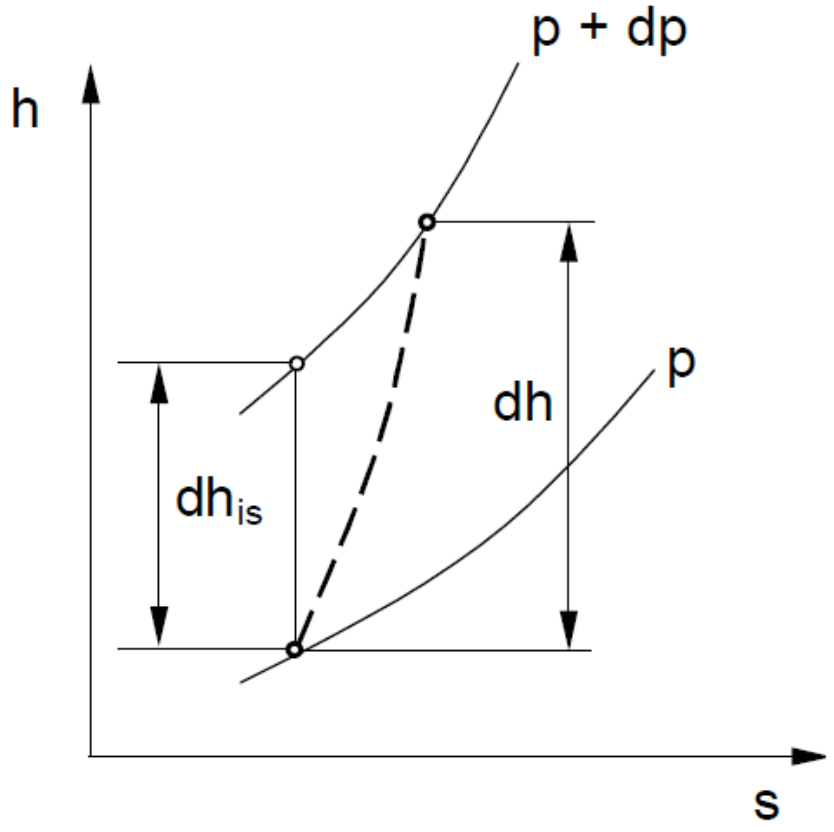

FIGURE 2.5: Definition of polytropic efficiency

2.1.4 Compressor Performance Map

The compressor map is one of the most important graphs through which it is possible to understand how the machine works in terms of correct mass flow, pressure ratio and efficiency. The first line to consider is the surge line, above which the compressor stall. This line is considered as the compressor stability limit, in fact if an operating point is beyond that line the compressor starts to unstably behave and all the performance drastically fall. Later we can see lines that have a vertical asymptote: these lines are called iso-velocity lines. The asymptote is the choke limit, which means that it is physically impossible to reach a mass flow rate greater than that of the rotation speed of the compressor. Another line of fundamental importance is the operating line that defines the behavior of the compressor when connected to the turbine and indicates how the machine is working. Finally, there are the iso-efficiency lines. The designer has the task of bringing the operating line and the most efficient line as close as possible. All the properties shown in the graph below are the result of the dimensionless analysis theory. In fact, the mass flow along the abscissa axis is the correct mass flow $\dot{m_{corr}}$ obtained by the

parameters T_{01} and P_{01}. These two parameters represent the whole temperature and pressure at the compressor inlet. The correct mass flow is used in order to take into account any small variation in conditions.

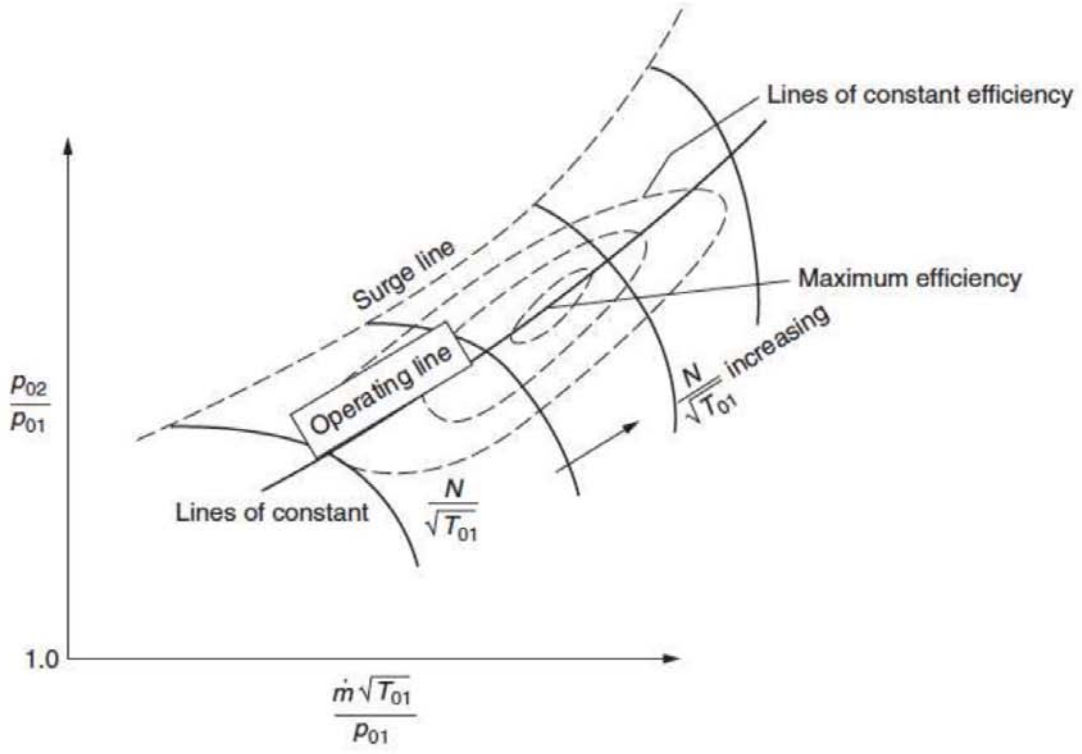

FIGURE 2.6: Compressor performance map [2]

The graphic in Fig. 2.7 shows how the compressor map is affected by multiple factors which cause the variation of the surge line. The aspect that is most interesting at the moment is that of inlet distortion, because as will be discussed later, a property of an S-duct is precisely pressure distortion. The loss in terms of pressure ratio along with the inlet distortion can be quantified as following:

$$\Delta PRS = |(R_{clean} - R_{distorted})/R_{clean}| \tag{2.5}$$

where R is the pressure ratio at surge, as illustrated in Fig. 2.8. All this is important to understand how the compressor stability is influenced by the mentioned parameters.

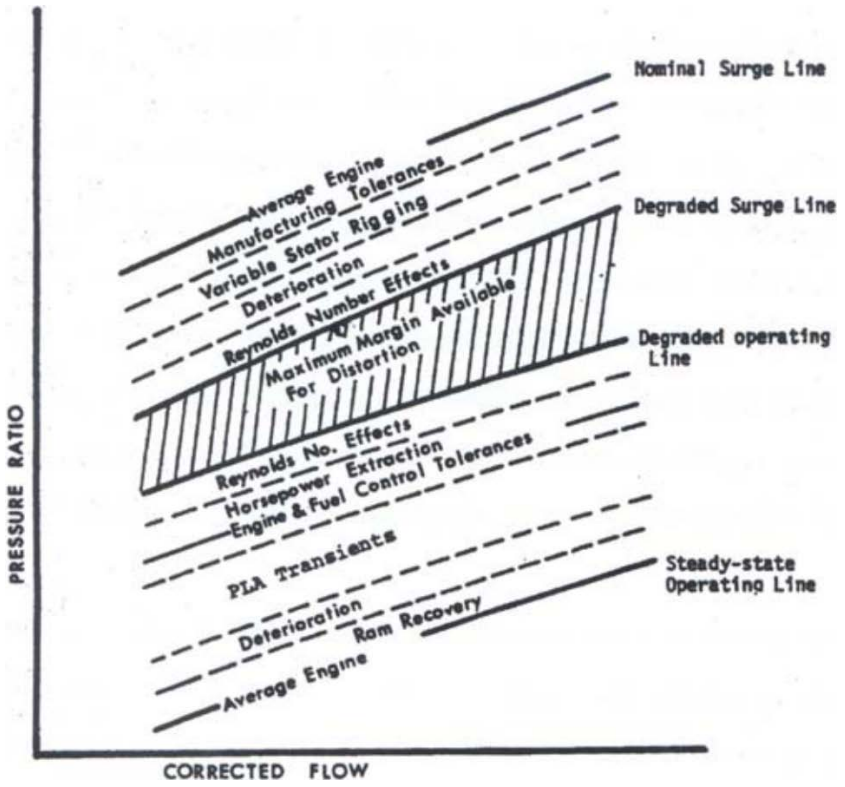

FIGURE 2.7: Destabilizing factors of a axial compressor [3]

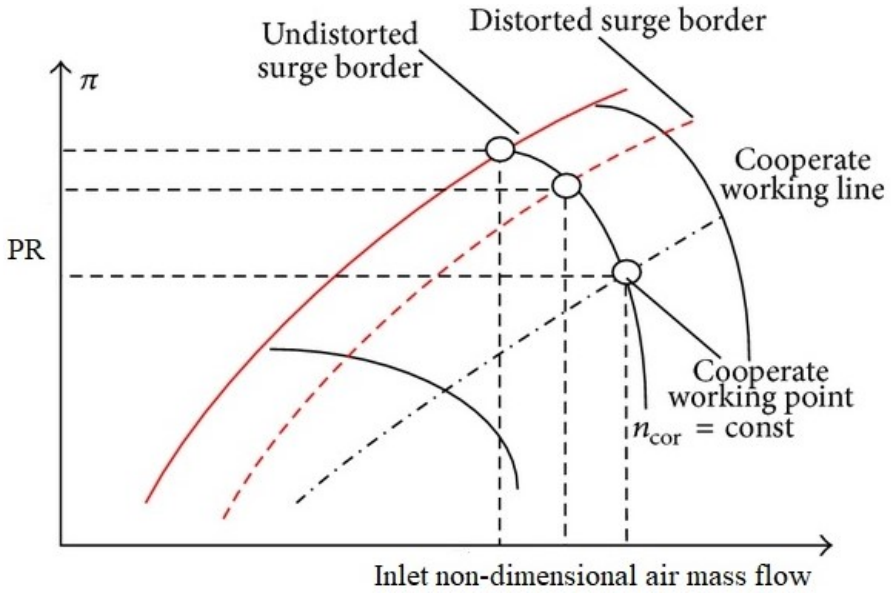

FIGURE 2.8: Surge pressure ratio loss

2.2 Transonic Axial Compressor

A transonic axial compressor is characterized by a relative supersonic inlet flow ($M_{rel} > 1$) that becomes subsonic in outlet ($M_{rel} < 1$). The transonic compressor is derived from the request for high thrust of the future turbofan engines, this determines high rotational speed. [16] Nowadays, the interest in these machines has increased extremely due to the desire to obtain a high compression ratio and a high efficiency. An increase in efficiency in general could save a lot of fuel by reducing the costs of use, it would produce less environmental pollution. All this can determine a key factor for the success of this product [17]. Furthermore, if the compression ratio increases, this implies the reduction of the dimensions (overall dimensions and weight) of the engine with a reduction of the production costs. For these reasons, research on this type of compressor is widespread and is expected to further increase. As stated in [18], the PR can easily exceed values of 2 (despite the maximum of 1.3 of the subsonic compressor), and on the other hand the efficiency rises up to about 90% or more.
There are drawbacks, however, in the use of transonic compressors such as the high complexity of the flow field that is created inside the compressor and the need to use materials capable of resisting the engine speeds and the required efforts. The presence of shock waves also creates a serious problem in operation outside the design conditions because when the shock waves move, the operation of the entire compressor totally changes and the performance collapses.

2.2.1 Interpalar Flow Analysis

The supersonic profile, due to the presence of shock waves cannot be similar as the subsonic one. This one, indeed, if it is invested by a flow with Mach over 0.7-0.75, it is going to accelerate the flow due to its rounded leading edge. This acceleration of the flow will create a sonic bubble (as shown in Fig.2.9) in which the flow is at a $M > 1$, and hence the profile is defined as transonic.

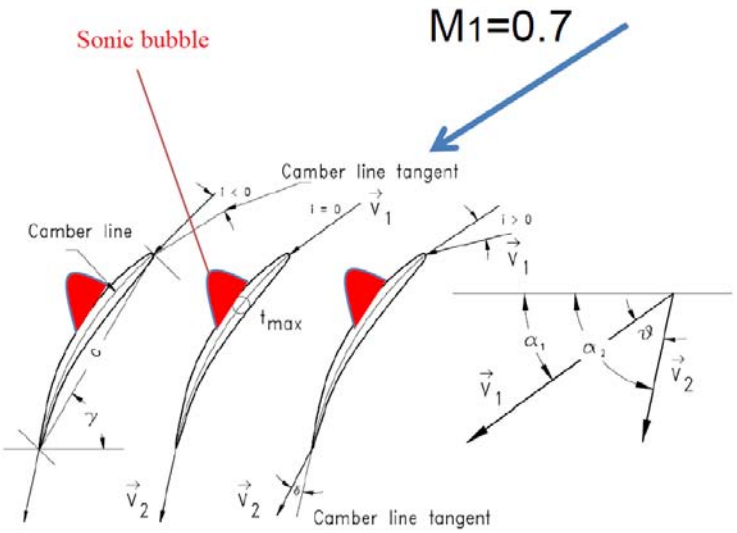

FIGURE 2.9: Sonic bubble over a subsonic profile [4]

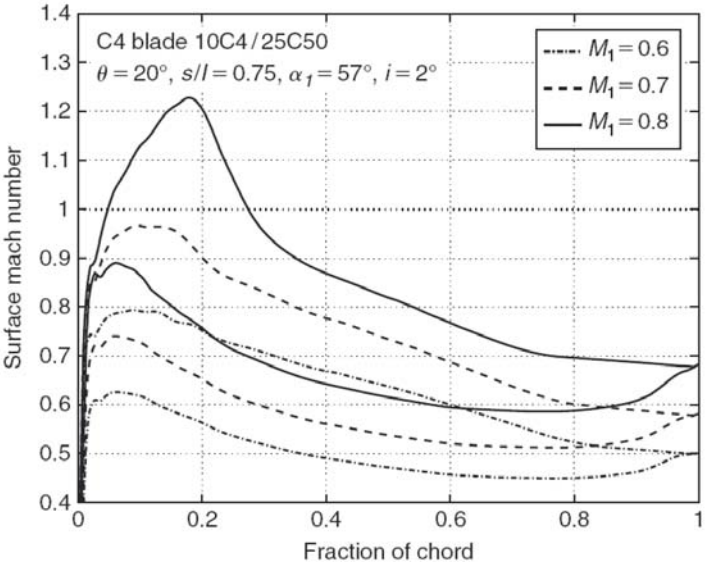

FIGURE 2.10: Variation of surface Mach number with different Mach at the inlet [4]

From Fig. 2.11 it is shown how the supersonic flow behaves while meeting a subsonic profile. A detached shock wave is formed which creates two different zone zones. The first is subsonic and the shock wave is almost normal, while the second zone that is formed away from the leading edge is supersonic because the shock wave is too weak.

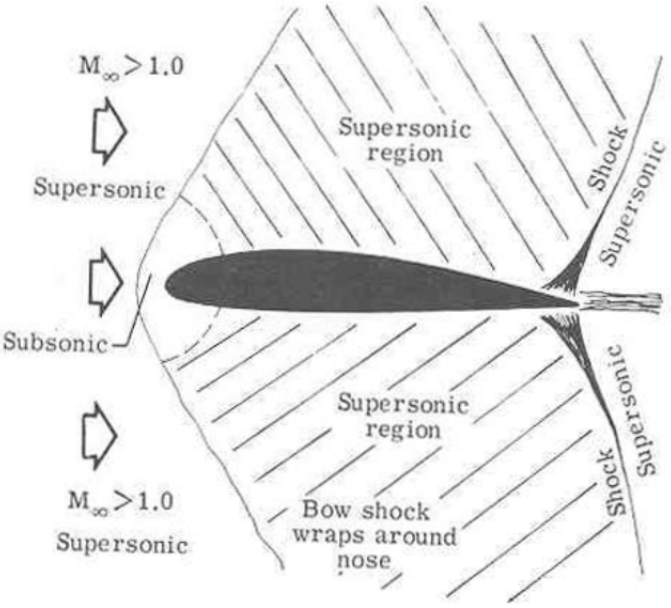

FIGURE 2.11: Subsonic profile with a supersonic flow

The aim of supersonic blades is to create an oblique shock wave attached and to do this the LE must be spiky. In fact, as you can see from the images shown, the shape is way different from the conventional ones (see Fig.2.12 and Fig. 2.13). To obtain such a thin profile the ratio between maximum thickness and the chord ($\frac{s_{max}}{l}$) is around a value of 0.04.

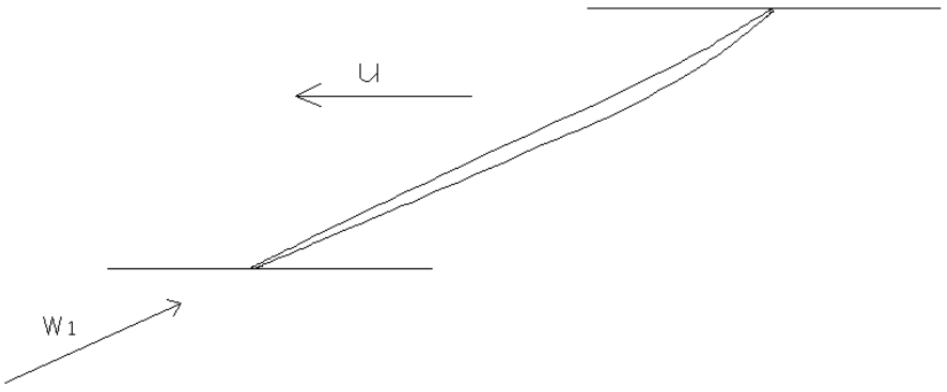

FIGURE 2.12: Supersonic profile

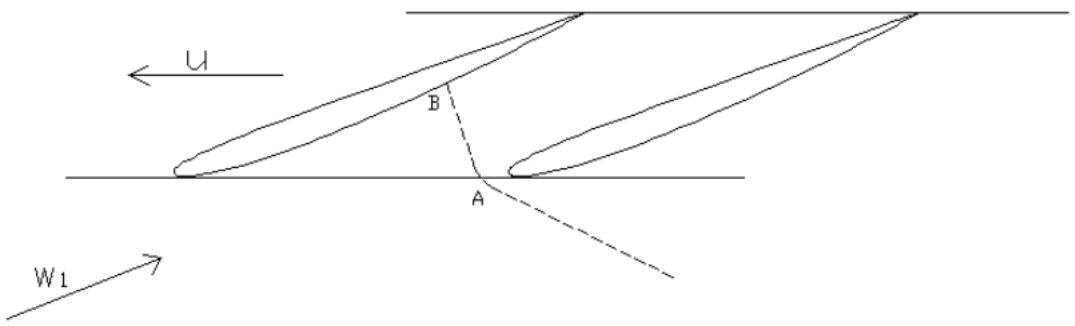

FIGURE 2.13: Subsonic profile

The differences between the two profiles are easily visible, in fact, the Fig.2.12 is highly more thin than Fig.2.13 with the maximum thickness situated over the 50% of the chord length.

2.3 Shock Wave Theory

Shock waves are irreversible processes, which occur in extremely thin regions [5]. Through a shock wave the temperature, pressure and density instantaneously increase, by maintaing the total temperature and enthalpy costant (at least in the normal shock). This occurs due to the fact that either the shock wave is a no-work process and there is no heat input. There are three different types of shock waves:

- Normal shock wave
- Oblique shock wave
- Bow shock

The normal shock wave is characterized by the fact that the postion of the wave is perpendicular to the flow direction, like it is shown in the Fig. 2.15 and, in this phenomenon, the flow properties vary radically; in particular the supersonic condition upstream of the shock is instantaneously turned into a subsonic condition downstream. Furthermore, as can be deduced from the equation 2.6, the Mach downstream (M_2) depends only by the Mach upstream of the shock. By studying the limit of the equation we can see that, more the Mach increases ahead of the wave, more it decreases after the shock; the limit results to 0.378 when $M \longrightarrow \infty$.

$$M_2^2 = \frac{1 + [(\gamma - 1)/2]M_1^2}{\gamma M_1^2 - (\gamma - 1)/2} \tag{2.6}$$

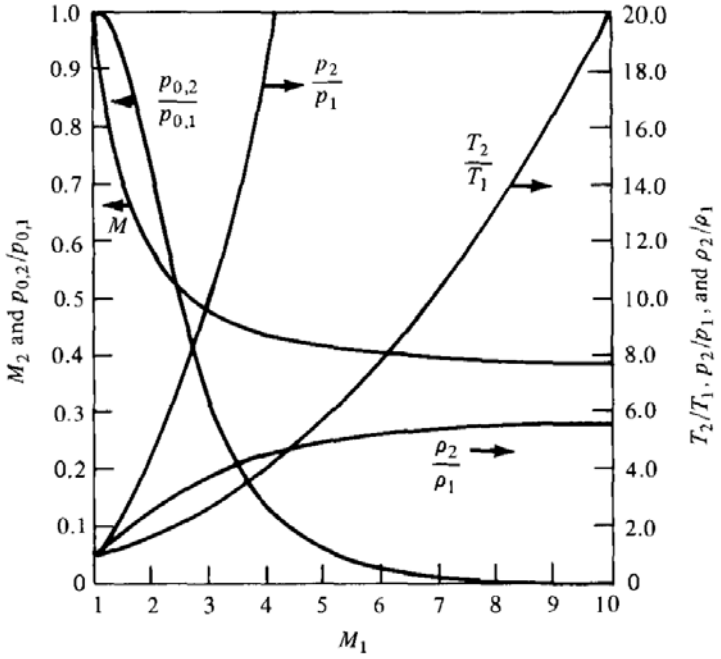

FIGURE 2.14: Variation of properties through a normal shock wave as a function of the upstream Mach number [5]

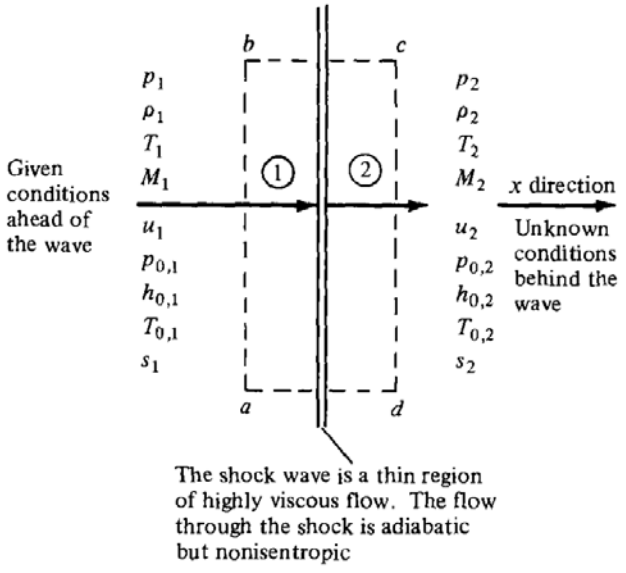

FIGURE 2.15: Normal shock wave [5]

The calculation of the variation of properties through a shock wave is not of interest to us in this Thesis, therefore it only be said that all the relationship between the properties are tabulated in tables with the parametric value of γ.

Speaking now of oblique shock waves, these are occuring when the angle between the flow and the wave is not 90°, but, as stated in [5] "the shock wave will make an oblique angle with respect to the upstream flow". What is interesting to note is that when a supersonic flow meets an angle there are two different behaviors, based on the shape of the angle itself. In fact, a distinction can be made between an oblique shock wave and an expansion wave. If the acute angle leads to an obstruction to the flow experiences an oblique shock with a continuous rise of the pressure, otherwise, if the acute angle involves an enlargement of the section the flow is accelerated and the pressure continuously decreases as can be seen in the following figure.

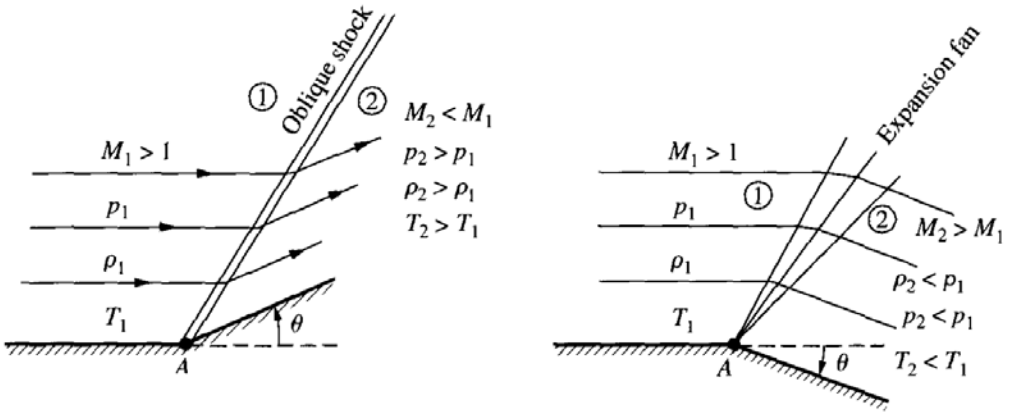

FIGURE 2.16: Interaction of a supersonic flow with an obstacle [5]

It is possible to see how the flow is deflected by an angle θ from is axial direction, and therefore thanks to this the velocity can be split into the tangential and normal components. From the equation of continuity along the tagential direction, it is possible to understand that the tangential component of the velocity remains constat across an oblique shock ($w_1 = w_2$) [5]. Even for this phenomenon all the relations of the properties are tabulated and, there is an equation for the Mach number downstream of the shock wave similar to the eq. 2.6.

$$M_2^2 = \frac{M_{n,2}}{sin(\beta - \theta)} \tag{2.7}$$

Eq. 2.7 and 2.6 are resembling each other; in fact they both show the variation of the Mach number. In the case of an oblique shock, the Mach downstream is governed only by both the normal component of the upstream Mach and the two angle β (wave angle) and θ (deflection angle).

Finally, to conclude the review of the oblique shocks there is the $\theta - \beta - M$ relation. From the continuity equation and recalling the constancy of the tangential components the relation is given by equation 2.8.

$$tan\theta = 2cot\beta \frac{M_1^2 sin\beta - 1}{M_1^2(\gamma + cos2\beta) + 2} \tag{2.8}$$

The previous equation gives us the values of the deflection angle as a function of M_1 and β and it can be plotted as in Fig. 2.17. Two principal areas are found in the $\theta - \beta - M$ diagram because once θ and Mach are set, there are only two possibilities of β. This is related with strong and weak shock (see Fig. 2.18); above the red line the flow field becomes subsonic (strong shock), whilst below that line the flow remains supersonic (weak shock). There is a second line (blue one) that is called sonic line and it divide the zone in which $M < 1$ and $M > 1$. Between the two lines there is a small area, in which even if the weak shock occurs, sometimes it can happen that the downstream Mach is subsonic.

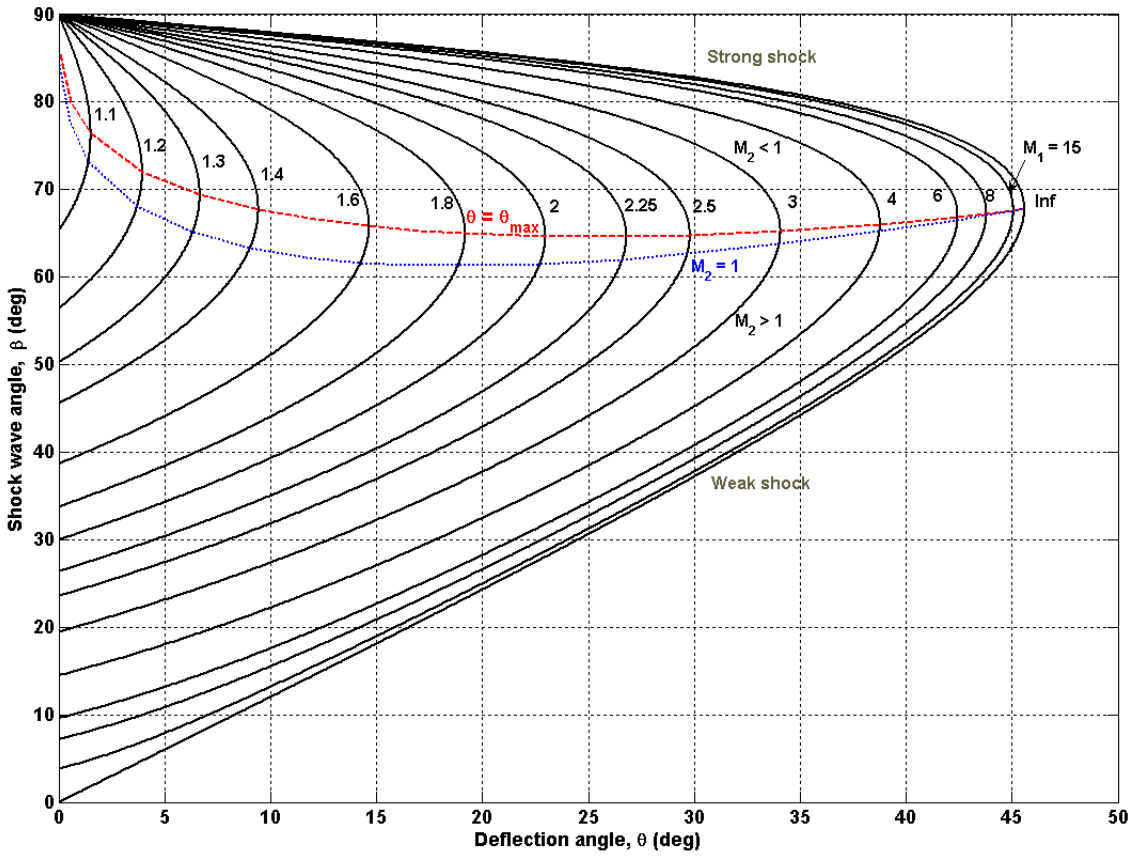

FIGURE 2.17: $\theta - \beta - M$

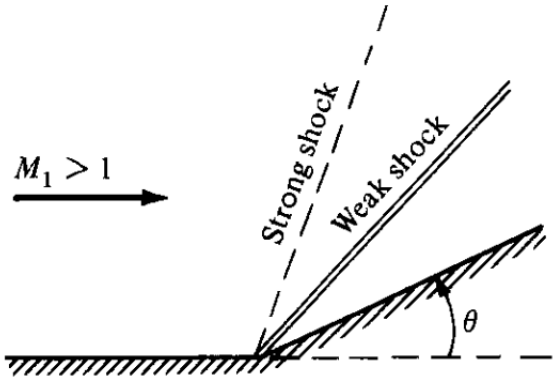

FIGURE 2.18: Weak and strong shock waves [5]

The red line connects all the maximum deflection angles of each iso-Mach line; in fact for every Mach number a maximum value of θ (θ_{max}) is set. The physics tells us that there is no solution when $\theta > \theta_{max}$: in particular no attached oblique shock is established, but, the new phenomenon that is created is a bow shock (detached from the blunt body).

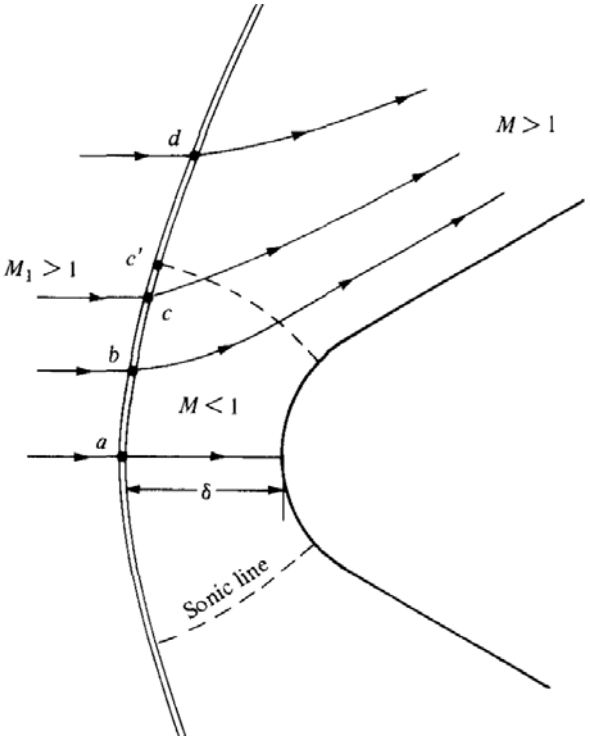

FIGURE 2.19: Supersonic flow on a rounded body [5]

The distance between the wave and the body is δ and it is called shock detachment distance. It is interesting to understand how the shock is developing along the wave. The point a is the point in which the shock wave is normal and it represents the strongest decelaration of the flow. Once the flow encounters the wave away from point a, the shock becomes weaker and curved, and sometimes it reaches the condition of the Mach wave. In the point b, instead, the shock is oblique and it is a strong wave as it is shown in Fig. 2.20, therefore the Mach becomes subsonic; the point c is the point of maximum deflection angle above which (from c to d) the Mach pertains in its supersonic flow field. Finally the parameters of the shock (δ, shape and flow field) are only function of the upstream Mach number and the shape of the body.

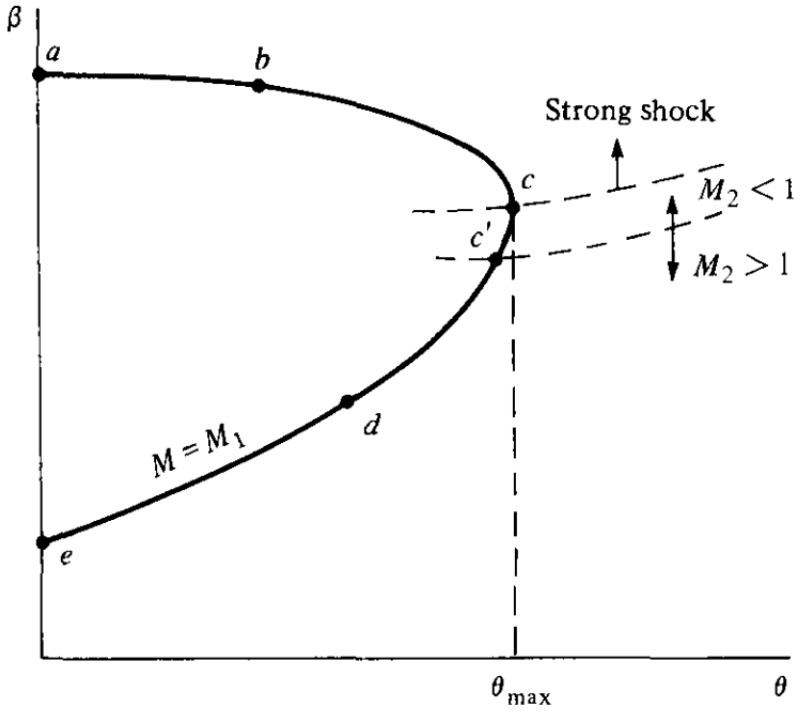

FIGURE 2.20: $\theta - \beta - M$

2.3.1 Shock waves in a Transonic Axial Compressor

As shown in the previous pages, a supersonic flow under certain conditions brings about a shock wave. These shock waves have a three-dimensional structure and it is the main cause of the rise of the pressure along the compressor. Furthermore, when there are shock waves, the blade is subjected to two different flows; the suction side is overwhelmed by a supersonic flow, while the pressure side is subsonic. This is caused because of the particular configuration of the waves (see Fig. 2.21). However, the presence of shock waves causes a disadvantage that is the penalizes the efficiency of the rotor; and in severe cases this shock waves might create problem as it is concerned with the stall. As it might be understood, the flow is extremely complex inside a transonic compressor, and the designers must take into consideration all the possible effects that occur (shock waves, seconday flows, boundary layer/shock interaction [6]).
The configuration of the shock waves inside a transonic compressor cascade is the one shown in Fig. 2.21.

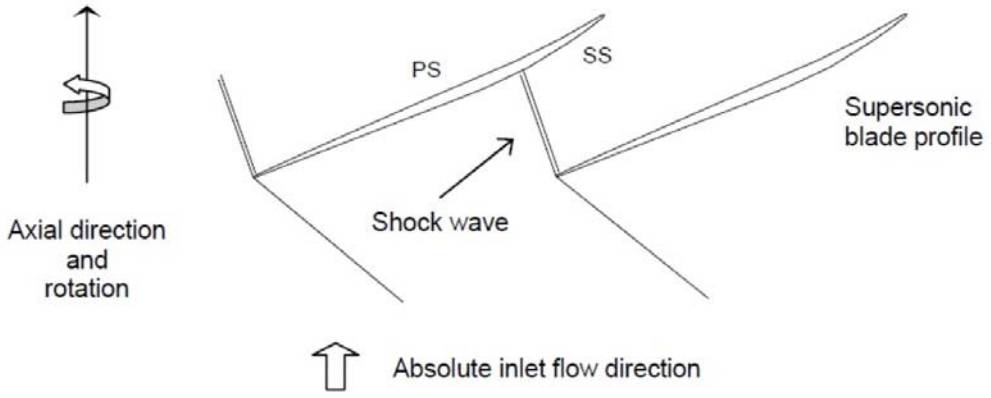

FIGURE 2.21: Shock waves in an interpalar canal

From the figure it can be seen as an oblique shock appears attached to the LE, that is called bow shock, whilst, inside the channel betweeen two blades, there is the creation of a normal shock wave called passage shock. The normal shock wave produces a major rise in the pressure and, as explained in the previous section, it is much stronger than the oblique and the therefore the pressure increases much more. When the flow meets the first wave, it still remains supersonic because the oblique shock wave is a weak shock; then however, when the flow arrives in the interpalar canal it creates a normal shock, downstream of which the flow becomes subsonic.

The configuration shown in Fig. 2.21 depicts a optimal condition that is the design operating condition. Once the compressor moves along the speed line the configuration changes by varying the position of the shock waves. One possibility is that if the back pressure increase, the operating point is moving towards the stall limit and in this case the bow shock is detached from the LE (Fig. 2.23). Contrarywise, if the back pressure is lowered, there is the choke condition. Briefly, when the operating moves from the choke condition to the surge line, the position of the shock wave is shifted upstream resembling to a normal shock. This happens because the mass flow rate diminishes and, therefore, the incidence of the flow is increased. All of this is summed up in the following Fig. 2.22 and Fig.2.23.

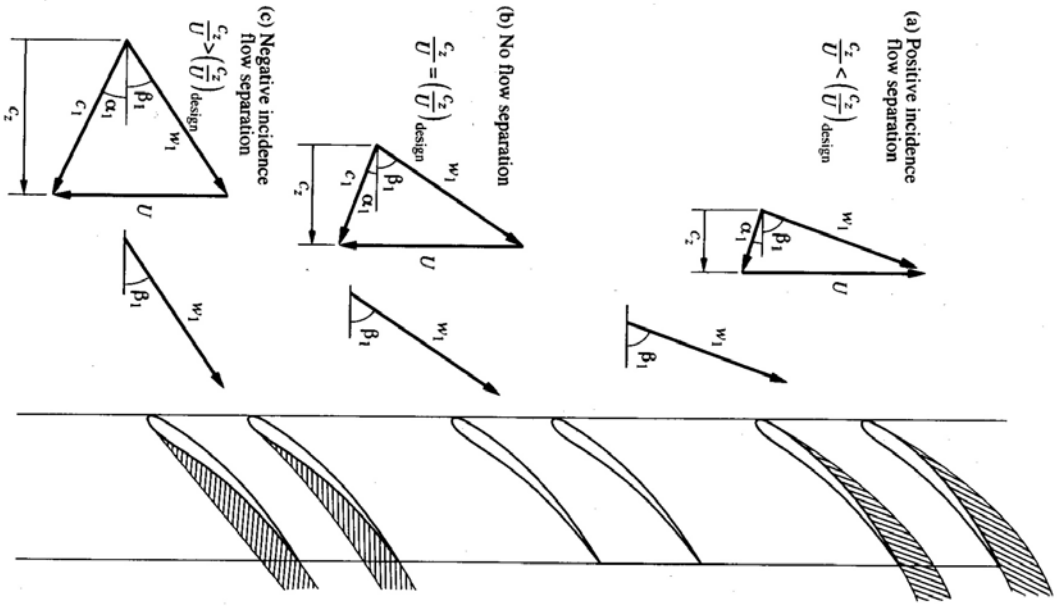

FIGURE 2.22: Behavior of the blade inside and outside the design conditions

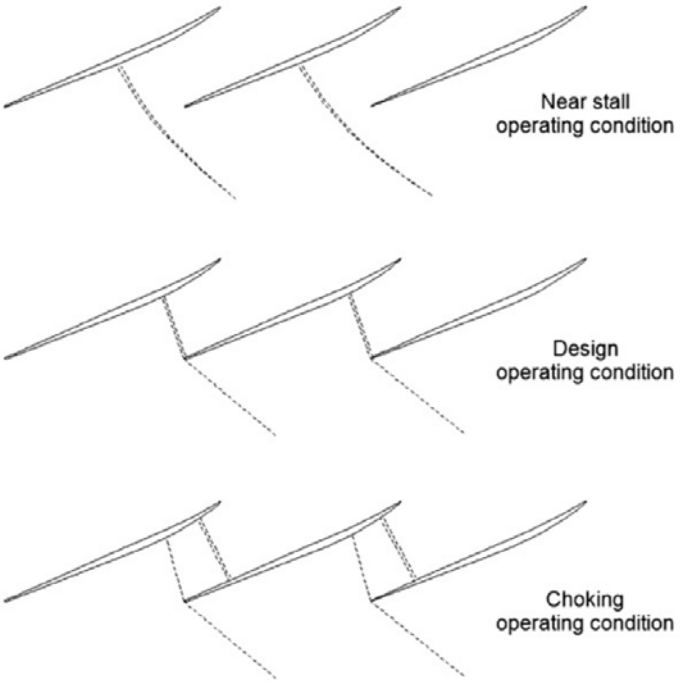

FIGURE 2.23: Impact of operating condition on a transonic axial compressor (constant wheel speed) [6]

Figure 2.22 show that it is possible that the shock wave negatively interacts with the boundary layer of the suction side of the blade. This provoke the thickening of the local boundary layer, which brings about the creation of a bubble (Fig. 2.24). In this case the aerodynamic losses are consistent and the efficiency collapses [6].

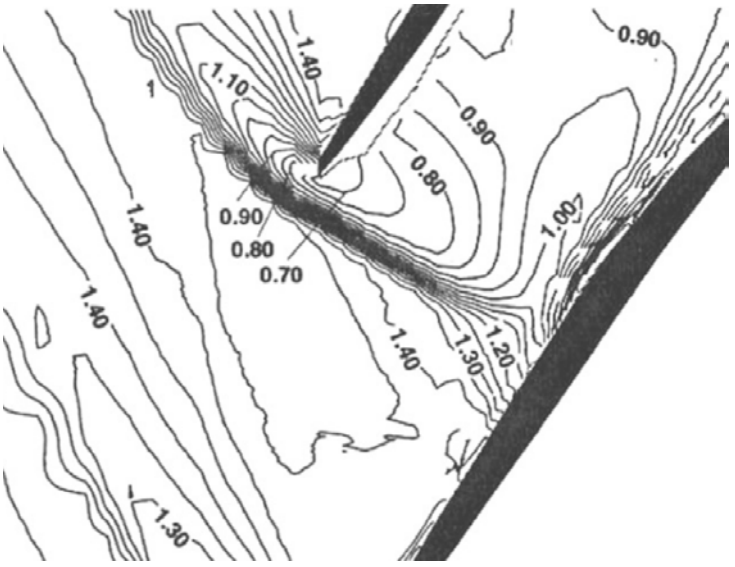

FIGURE 2.24: M_{rel} in a transonic axial compressor [7]

2.4 Three-Dimensional Losses

The transonic compressor it is a very complex machine due to the complexity of its inner flow field. As a cause of that, the estimation of loss in supersonic compressor blades has been a subject of major concern [19]. The losses, indeed, are not comparable with the one of a subsonic cascade in fact in this case are considered of primarly importance for the correct study of the machine.
The factors that render the flow process in a turbomachinery stage irreversible are:

- End wall losses
  - Secondary flow losses
  - Tip clearance loss
  - Labyrinth seal and leakage flow losses
- Shock losses
  - Total pressure loss
  - Shock-boundary layer interaction
- Blade wake losses
  - Viscous profile drag (from cascade experiments)
  - Induced drag losses
  - Radial flow losses
- Unsteady flow losses
  - Upstream wake interaction
  - Vortex shedding in the wake
- Turbolent mixing

Although the above list seems like a formidable assortment of flow losses, there is a possibility of counting a loss (or a part of it) twice or three times. The "list" in fact is made only as a tool to help our understanding of complex flow phenomena in broad categories, such as:

- Compressibility effects
- Viscous and turbulent dissipation
- Unsteadiness
- Three dimensionality

A transonic rotor creates a shock, which is weakened by suction surface expansion Mach waves and propagates upstream of the rotor row [20]. Note that since the upstream flow is subsonic in the absolute frame of reference, there is no zone of silence preventing the propagation of the rotor created waves. Fig.2.25 shows a typical flowfield. The broad category of "end wall" losses encompasses the annulus boundary layer, corner vortex, tip clearance flow, and the seal leakage flow. The tip clearance flow is a pressure-driven phenomenon that relieves the fluid on the pressure side towards the suction surface, as shown in Fig.2.26.

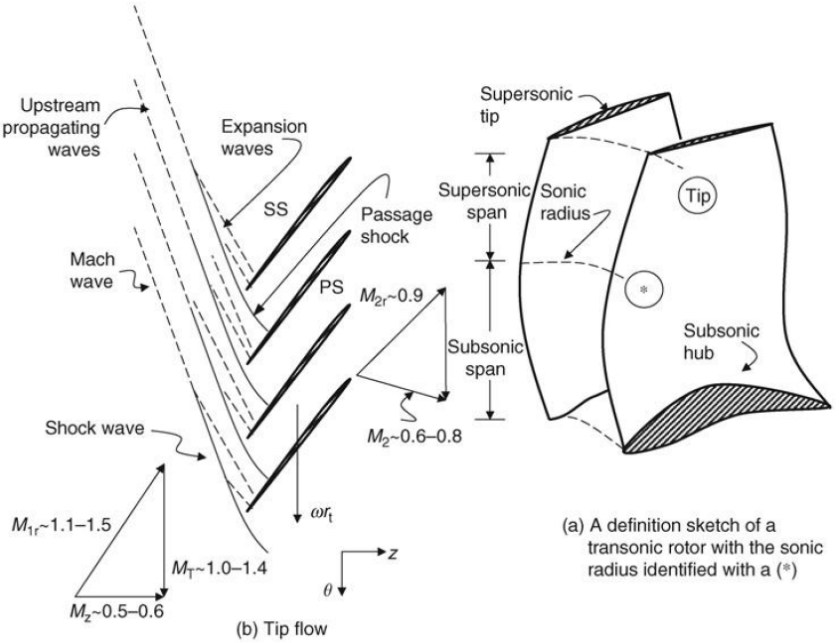

FIGURE 2.25: Transonic rotor and it's tip flow field/wave pattern (bow shock and expansion waves) [8]

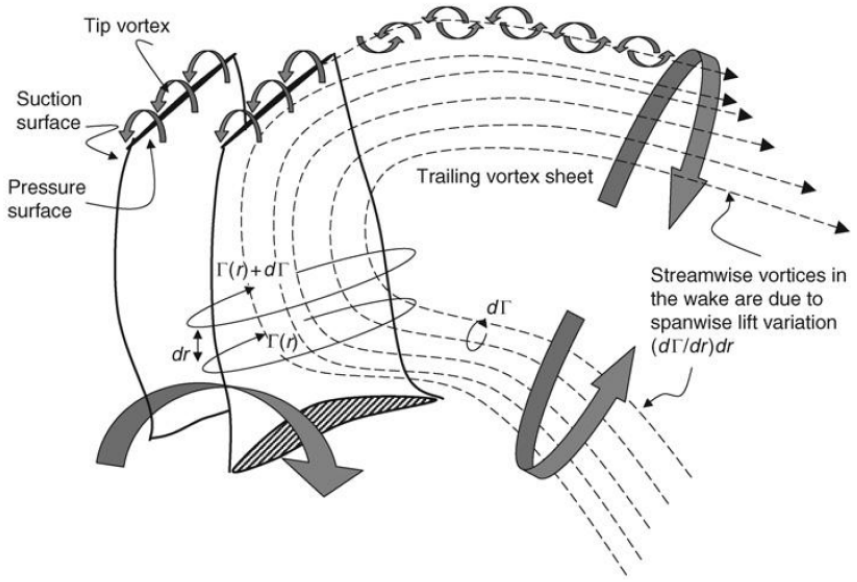

FIGURE 2.26: Schematic drawing of tip vortex roll up and the inviscid wake composed of streamwise vortices due to spanwise lift variation on the blade [8]

The boundary layer formation on the entire annulus is expected to grow in response to an adverse pressure gradient and with distance. The increase of the boundary layer with the number of stages is shown by the data of [9], where the axial velocity distribution continually deforms and by the exit of the second stage there is no resemblance to the inlet flowfield characterizes [8]. The formation of corner vortices and the associated total pressure loss may be deducted from Howell data, as shown in Fig. 2.27(a). Modern blade design takes into account for this difference in the relative flow angle in the boundary layer and bends the blade ends to minimize incidence loss. A schematic drawing of an end-bender blade is shown in Fig. 2.28.

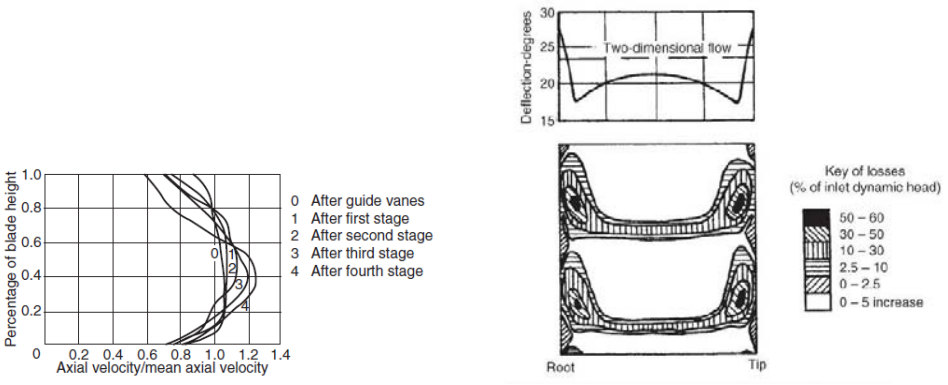

(a) (b)

FIGURE 2.27: An aspect of end wall flow losses [8]

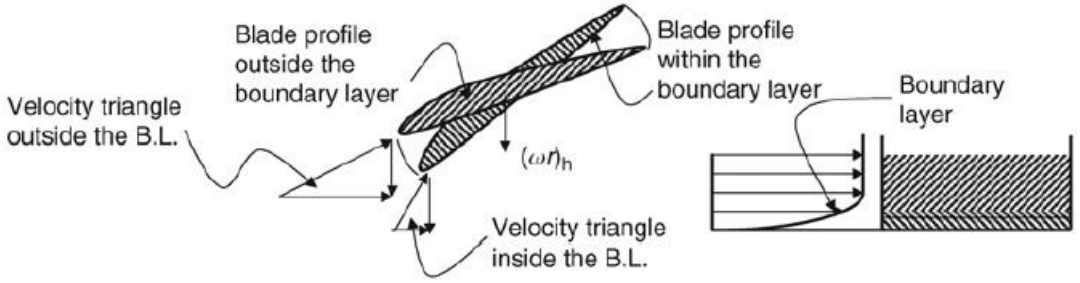

FIGURE 2.28: Bent tip blade to account for a larger boundary layer incidence due to a streamwise momentum deficit [8]

A flow turning within the blade passages of a compressor leads to a migration of the boundary layer fluid from the pressure surface toward the low-pressure side, namely, the suction surface. A flow pattern normal to the primary flow direction is then set up, which is called a secondary flow. A schematic drawing is shown in Fig. 2.29. The best work on the formulation of secondary flows is due to [21] and a optimal engineering formulation is due to [22]. The upstream wake interaction with the following blade row is one source of unsteadiness [23]. This interaction results in a shed vortex of opposite spin in the wake. Another source of unsteadiness to a blade row is its relative motion with respect to a downstream blade row. Indeed, the blade is not engaged in a viscous wake chopping activity, as in the previous case, but it is operating in an unsteady pressure field created by the downstream blade row. Blade vibration in bending, twist or combined bending, and torsion is inevitable for elastic cantilevered structures.

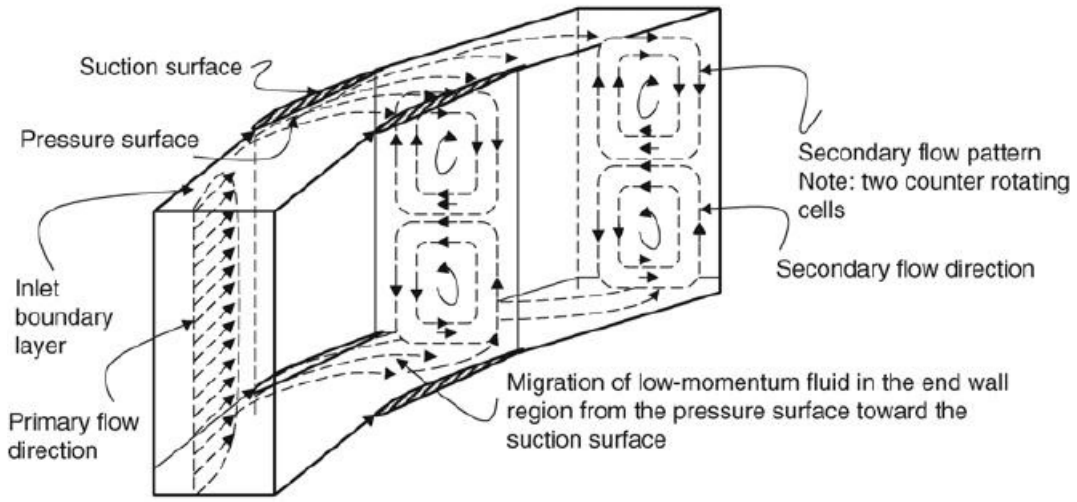

FIGURE 2.29: Viscous flow in a bend creates a pair of counterrotating streamwise vortices, which set up a secondary flow pattern [8]

Therefore, blade vibration induces a spanwise variation of the incidence angle, hence an unsteady lift with a subsequent vortex shedding in the wake [8].

The unsteady vortex shedding phenomenon is schematically shown in Fig. 2.30.

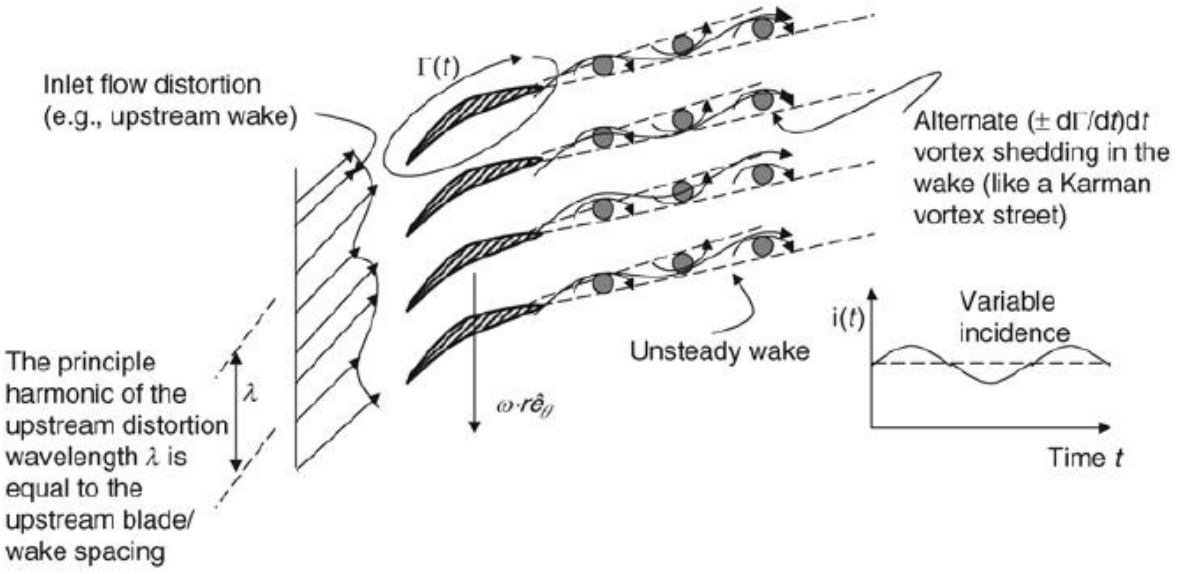

FIGURE 2.30: Unsteady flow interaction with a blade row causes periodic vortex shedding in the wake [8]

The individual losses and their contributions to the overall loss are depicted in Fig. 2.31. We note that at the design point the overall losses are near minimum and in low flow, the compressor enters surge and at the high flow rates profile losses dominate due to flow separation.

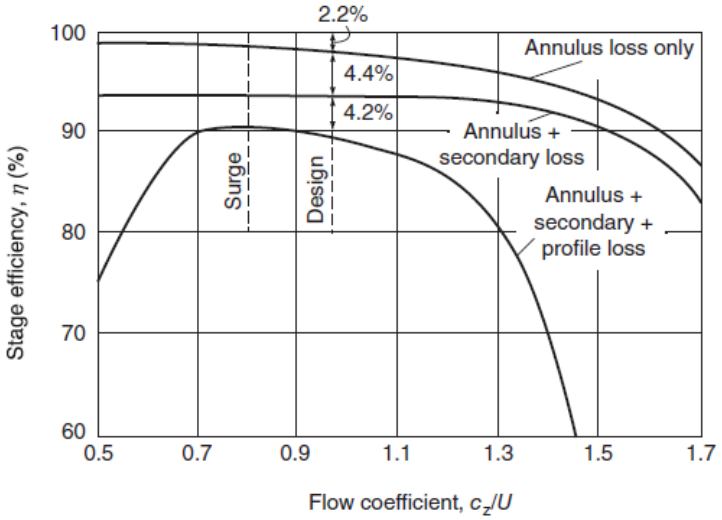

FIGURE 2.31: Contributions of different losses in a compressor stage [9]

Chapter 3

Baseline Validation

This chapter contains the analysis of the baseline geometry of the NASA Rotor 67. First of all, the analysis of the single channel was carried out. To carry out this analysis, several meshes were taken into consideration in order to understand which was the most correct mesh to describe the physics of the rotor. The next step was to analyze the entire rotor in order to verify that its operation corresponded to the analysis of the single channel. For the analysis of the whole rotor, in fact, a lighter mesh was used for each channel because a too heavy mesh meant the analysis failed. The ogive built by [24] was then added to the analysis of the entire rotor.
The software used for all of the simulations are:

- CFX-TurboGrid for the generation of the mesh of the rotor
- CFX-Pre-Solver to set the parameters for the simulation
- CFD-Post to visualize the results and to the post-processing
- SolidWorks to create the geometry of the ogive
- ANSYS Workbench to create the mesh of the ogive

All of these analyzes are done by exploiting the Delta cluster of Cranfield University, which was very useful because a normal personal computer does not have the necessary computing power. Unfortunately, however, as will be explained later, the Delta cluster, due to the limitations of use for each student, was not entirely sufficient for all analyzes. This problem was caused by the considerable complexity of the complete analyzes.

3.1 NASA Rotor 67

The Rotor 67 (R67) is a transonic low aspect-ration fan developed by NASA and it represents the first stage rotor of a two stage fan.

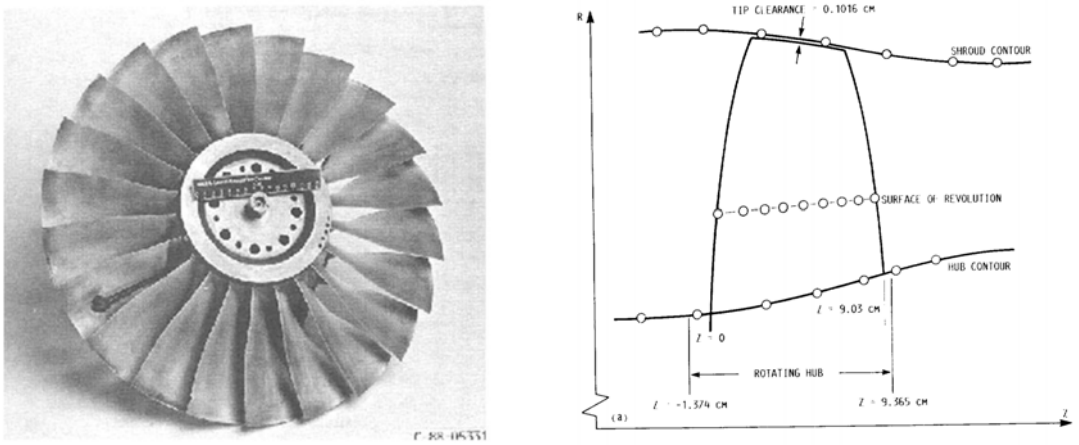

(a) Nasa Rotor 67 (b) Meridional projection of the blade

FIGURE 3.1: Features of the NASA Rotor 67 [10]

The properties of the R67 are reported in Table 3.1 and they are referred to the design operative point. This rotor was developed by NASA as a test case and numerous studies have been conducted on it over the years. Many of these studies, like the one addressed in this thesis, aim to optimize the geometry of the blades so as to obtain an improvement in performance.

TABLE 3.1: Properties of R67

Properties	Value
Compression Ratio (PR)	1.64
Mass Flow Rate	33.25 $[\frac{kg}{s}]$
Rotational Velocity	16043 $[rpm]$
Tip Velocity	429 $[\frac{m}{s}]$
M_{rel} at inlet	1.38
Number of Blades	22
Inlet Diameter	51.4 $[cm]$
Outlet Diameter	48.5 $[cm]$
Shroud Tip	0.1016 $[cm]$

3.1.1 Original NASA Analysis

This section contains the original rotor analyzes carried out by NASA in 1991. It is possible to see in the images and graphs below the comparisons made at the time between the data obtained from experimental measurements and the data obtained from fluid dynamic simulations carried out on the computer.

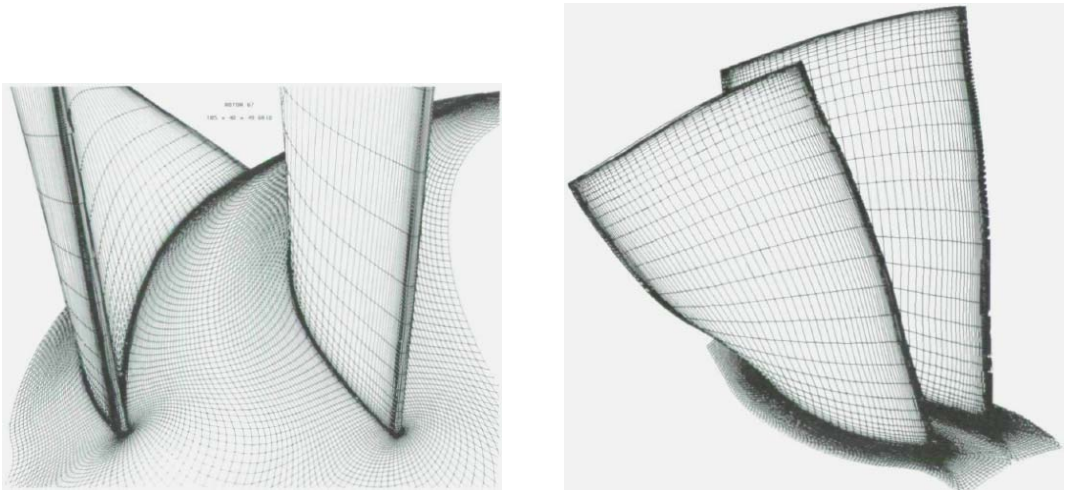

(a) Grid leading edge enlargement

(b) Computational grid. 185 C x 40 tangential x 49 spanwise points.

FIGURE 3.2: Mesh grid of the palar canal [11]

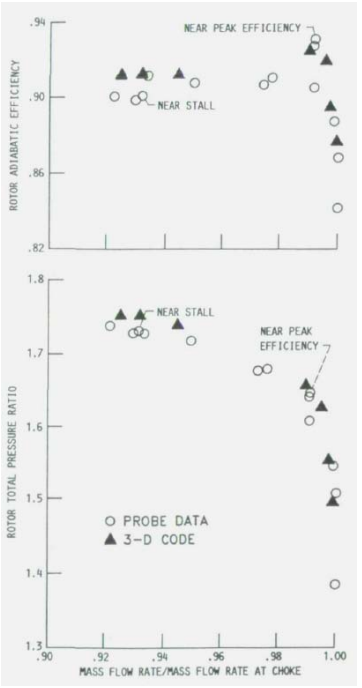

FIGURE 3.3: Comparison of computed and measured adiabatic efficiency and total pressure ratio characteristic at 100 % speed

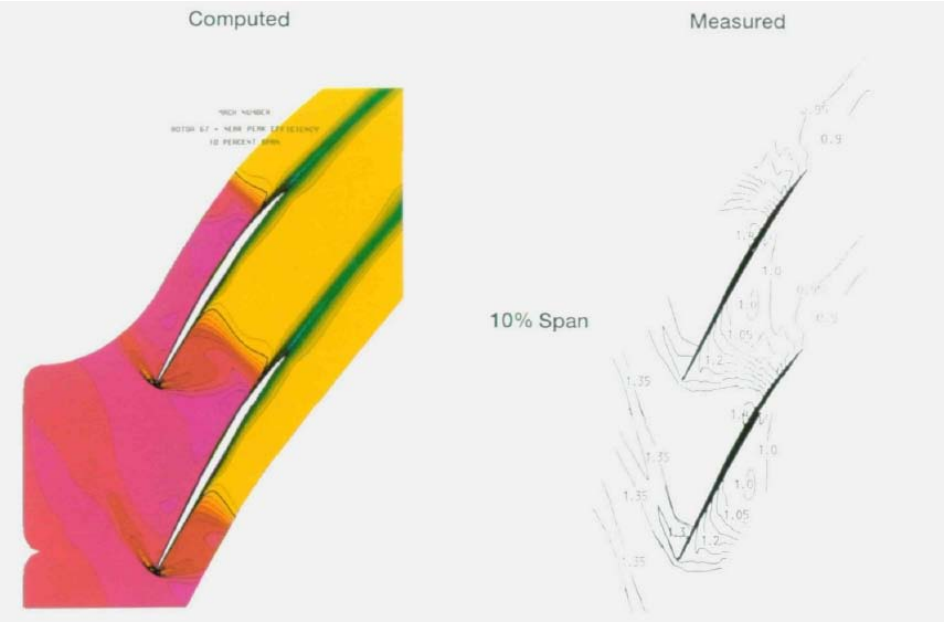

(a) 10 % span

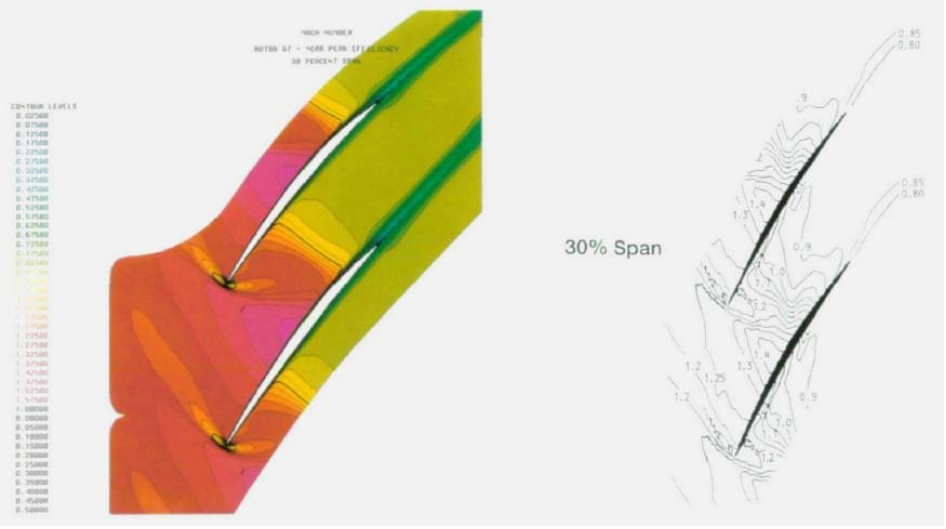

(b) 30 % span

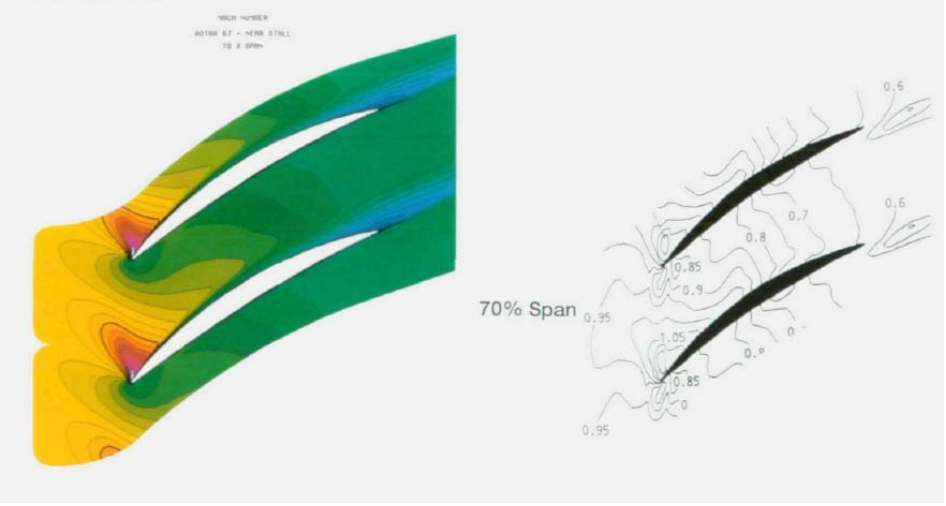

(c) 70 % span

FIGURE 3.4: Contours of relative Mach number, near peak efficiency. In computed plots heavy line is M = 1.0, and contour increment is 0.05. [11]

3.2 Computational set-up of the analysis

The aim of this computational analysis is to validate the model. This means comparing the results obtained from the analysis with the experimental results obtained through measurements. To consider the validated model, the deviation of the results must not be too high compared to the real ones, if not, in fact the model could not be used for further research because it does not represent reality. The problem is that variance in results could be caused by multiple factors. As you can easily guess, the simulation highly depends on the initial parameters such as boundary conditions. To cite some examples of critical boundary conditions there are the entry and exit conditions, the order used to solve the Navier-Stokes equations, the turbulence models used and the number of iterations taken into consideration.

In order to obtain a correct geometry of the rotor blade, the data from the domain [10] published by NASA were extrapolated. In this document there are the original laser measurements carried out in 1989. From this data the hub, shroud and profile files have been created in the correct form for the use of ANSYS CFX-TurboGrid. The result of the re-construction of the blade is shown in Fig. 3.5.

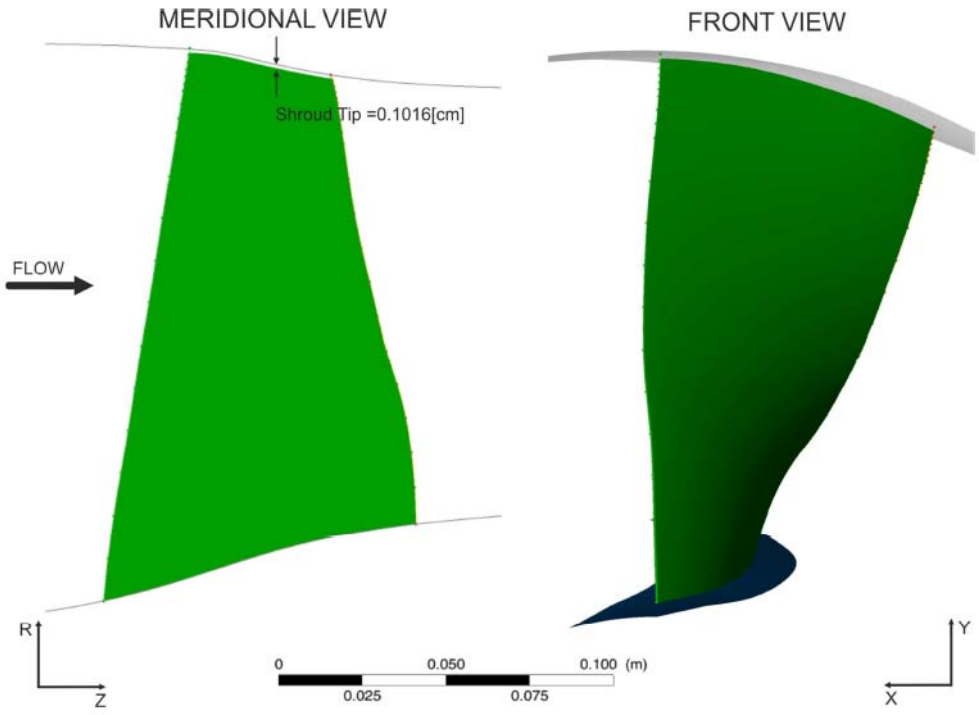

FIGURE 3.5: Meridional and front views of the blade in ANSYS® CFX-TurboGrid

3.2.1 Computational Grid Generation

The computational mesh grid has been created with ANSYS CFX-Turbogrid and the domain developed for this simulation is divided on three different parts as shown in Fig. 3.6:

- Inlet
- Outlet
- Passage

The section called Passage is the most critical because it contains the blades and the quality of the simulation depends strongly on the quality of the mesh. In fact the flow is remarkably complex and to respect the physics of the system the analysis must be very accurate.

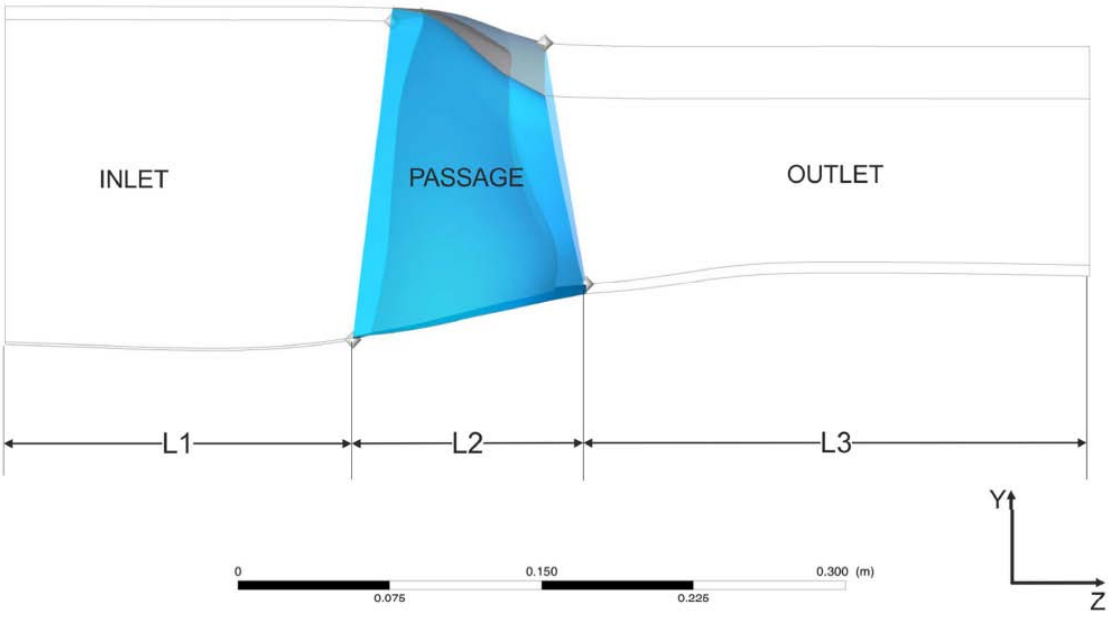

FIGURE 3.6: Inlet, passage and outlet configuration [12]

Once the geometry files have been loaded, with an accurate setting of the data relating to the generation of the mesh, the following figure is obtained as a result Fig. 3.7. To improve the quality of the system study, intermediate layers have been added in the simulation.

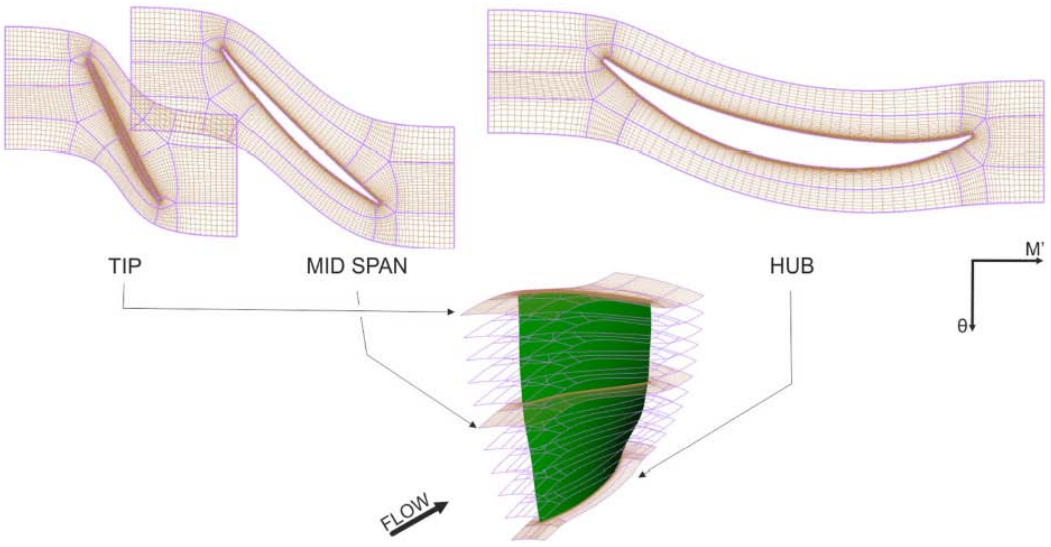

FIGURE 3.7: ANSYS® TurboGrid topology: layers of hub, midspan and tip section

In order to achieve a accurate mesh grid the number of elements is set at 2.38 million. Such a high number of nodes is necessary to obtain a correct study of the system in order to have an accurate description of the flow through the palar canal. The final mesh is shown in Fig. 3.8.

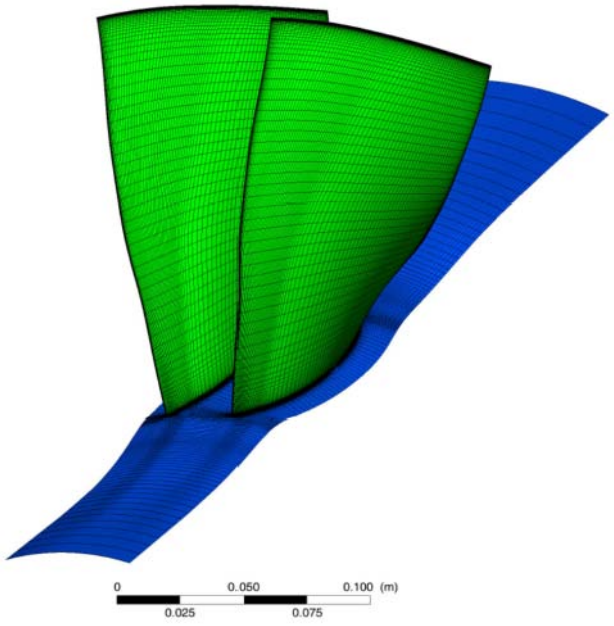

FIGURE 3.8: ANSYS® TurboGrid computational grid

3.2.2 Turbulence modeling

To study the turbulent flow of this analysis correctly, it is advisable to carefully choose the model to be used and near-wall approach to simulate the phenomenon as close to reality as possible. In CFD application the possible approaches during the calculation are three:

- DNS Direct Numerical Simulation
- LES Large Eddy Simulation
- RANS Reynolds Averaged Navier-Stokes Simulation

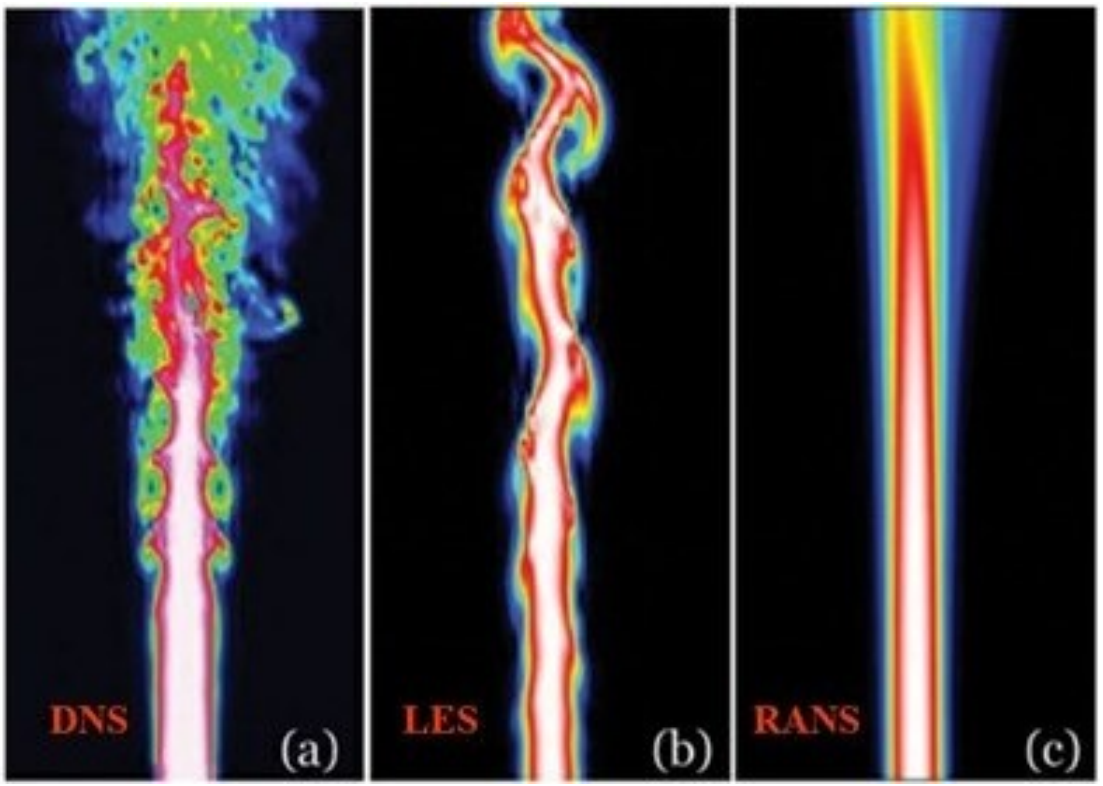

FIGURE 3.9: DNS, LES and RANS examples

It is not of interest for this work to study in detail the differences between the three applicable models, it can be said that the most accurate is the DNS, because it resolves the full N-S equations. But precisely for this reason its computational cost is prohibitive. LES model instead are less time-consuming compared to the DNS model, but this is still too much for most of the practical applications. Therefore, the turbulence model used is the RANS one because its cost of the simulation is

much lower than the others. Given the computational model taken into consideration, it is necessary to choose the turbulence model. For this work the SST $k-\omega$ model is used, due to its best accuracy in predicting the behaviour of the flow rather than any other RANS models.
As it is concerned the near-wall region there is two methodologies available:

- Wall Function, which saves computational costs using empirical equations. As stated in [25] this choice is suitable for problems where the attention is focused in the middle of the domain rather than in the boundary layer. In thi case the restriction on y^+ is not that strict
- Low-Reynolds-Number, where y^+ requirement are very tight ($y^+ \approx 1$). Therefore, a very fine mesh is needed near the wall bringing about a large number of nodes. This models perfectly suits for turbomachinery performance because the forces and heat transfer are well described.

3.2.3 CFX-Pre Set-up

CFX-Pre is an ANSYS's tool with which all the parameters of the simulation are set. In the next Table 3.2 all of the relevant parameters are reported.

In this analisys the convergence was critical throughout all the calculation, so to solve this problem a user function was implemented with the purpose of adapting the maximum timescale, which indeed is of utmost importance for calculation stability. At the beginning a value of 1e-7 [s] was set, then it was increased up to 1e-4 [s], for then return to lower values around 1e-5 [s] before calculation was stopped. The convergence was established when the RMS maximum residue were lower than 1e-5 and the variables of interest described in the next paragraph had an asymptotic behavior.

Table 3.2: Set-up of the parameters in CFX-Pre

	Ansys CFX Solver set-up	
Analysis Type	Steady State	
Domain	Domain Type	Fluid Domain
	Fluid and Particles Definition	Air Ideal Gas
	Reference Pressure	0 [atm]
	Domain Motion Option	Rotating
	Domain Motion Angular Velocity	-16043 [$revmin^{-}1$]
	Heat Transfer	Total Energy
	Turbulence Option	SST
	Wall Function	Automatic
	Wall Heat Transfer Model	High Speed
Boundary Condition	Hub	No Slip Wall Smooth Wall Adiabatic Rotating Frame
	Shroud	No Slip Wall C-R Wall Smooth Wall Adiabatic Rotating Frame
	Inlet	Subsonic Stat. Frame P_0 101325 [Pa] Normal to BC Stat. Frame T_0 288.2 [K] Frame Stationary
	Outlet	Subsonic MFR or Pressure Variable
Solver Control	Advection Scheme	High Resolution
	Turbulence Numerics	High Resolution
	No. Iteration	3500
	Timescale Control	Auto Timescale
	Convergence Criteria	MAX 1e-5

3.2.4 Calculation Of The Variables Of Interest

The rotor performances have been calculated in suitable reference positions. These positions were the same of those adopted in the NASA Report [11], for which experimental data are available derived from the measurements. Total pressure ratio and polytropic efficiency were evaluated taken into account quantities calculated with a mass-weighted average surface integral. In particular, the total pressure ratio was defines as:

$$\pi_c = \frac{p_2^0}{p_1^0} \tag{3.1}$$

where p_2^0 and p_1^0 are the total pressure in the stationary frame at the position 2 and 1, respectively, calculated with the aforementioned mass-weighted integral. On the other hand, the polytropic efficiency was defined as:

$$\eta_{pol} = (\frac{\gamma - 1}{\gamma})\frac{ln(\pi_c)}{ln(\frac{T_2^0}{T_1^0})} \tag{3.2}$$

in which T_2^0 and T_1^0 are the total temperatures in stationary frame at the position 2 and 1, respectively. The isentropic efficiency was defined as:

$$\eta_{iso} = \frac{\pi_c^{(\frac{\gamma-1}{\gamma})} - 1}{\frac{T_2^0}{T_1^0} - 1} \tag{3.3}$$

In addition to global variables, the performance distributed along the span is of utmost importance because through these it can give a understanding on which part of the blade affects in greater amount global performance.

3.3 Validation

This section deals with the validation of the model for further implementation. To obtain the validation of the analysis we need the error between the CFD and experimental data results to be as low as possible. In order to do that, many models have been developed with different mesh to understand if it is possible to achieve good results even with a coarser mesh. In fact, if this were possible, many calculation costs could be saved.

TABLE 3.3: Comparison of different type of mesh implemented [24]

	Number of Nodes	Computational Cost
Coarse $k-\epsilon$	700k nodes	1.5 hours
Coarse	800k nodes	2 hours
Fine	1.60 mln nodes	4 hours
Very Fine	2.38 mln nodes	6 hours

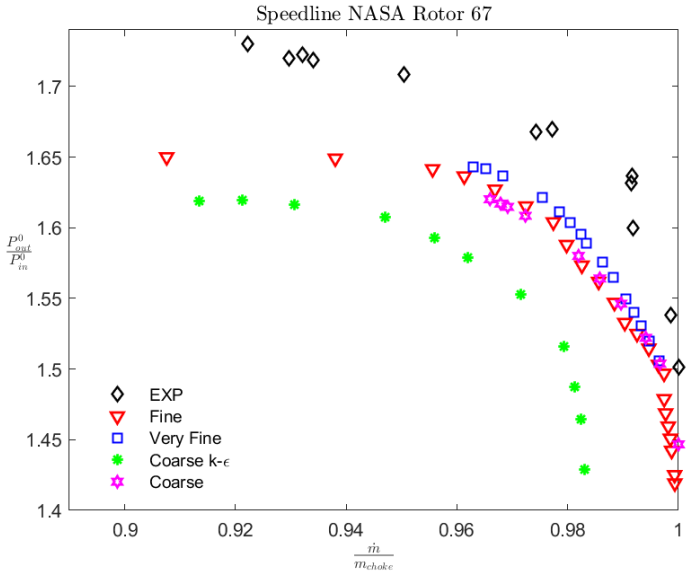

FIGURE 3.10: Speed line NASA Rotor 67 [24]

The Fig. 3.10 show the speed line of the NASA Rotor 67 with a rotational speed of 100%. This graph was obtained by [24] by varying the pressure at the outlet, starting from the choking condition and increasing the pressure untill the stall margin is reached. The pressure ratio is calculated respect to the mass flow rate $\frac{\dot{m}}{\dot{m}_{choke}}$. Analyzing the Fig. 3.10 the evolution of the experimental data is almost match for every mesh take into account but the error commited varies from mesh to mesh as it can see in Table 3.4. The very fine mesh, as expected, presents the closest values to the experimental ones even if the deviation is still evident.

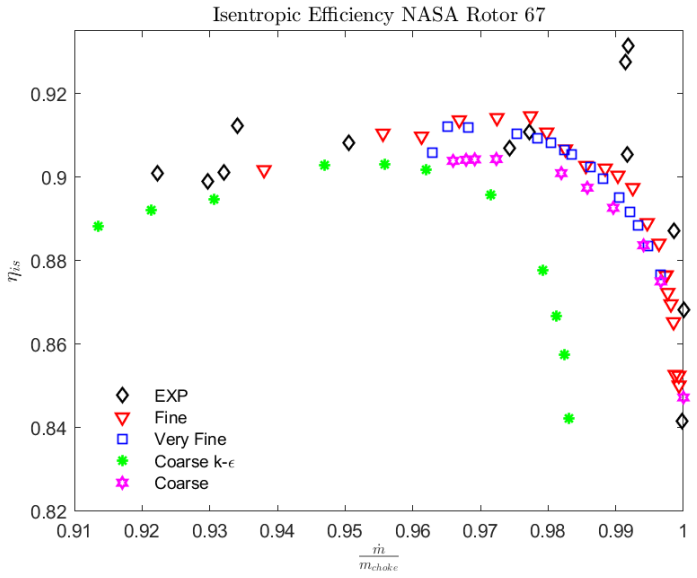

FIGURE 3.11: Isentropic efficiency NASA Rotor 67 [24]

TABLE 3.4: Comparison of different type of mesh implemented [24]

	Mass Flow Rate $[\frac{kg}{s}]$	Relative Error	PR	Relative Error
Design Point	33.25	-	1.64	-
Coarse $k-\epsilon$	33.4185	0.0051%	1.5829	0.024%
Coarse	33.2862	1.08e-3 %	1.6263	0.005 %
Fine	33.4047	0.0046 %	1.6372	0.0009 %
Very Fine	33.2350	4.03e-4%	1.6409	0.0002%

The Table 3.4 shows the relative error committed by during the simulation of the single palar channel. As you can see the coarse mesh correctly represents the phenomenon, and seen this fact it was used to analyze the compressor map as the cost on time is much less. In fact, the relative error is not that far from the one commited with the very fine mesh. Furthermore, with the analysis of the variation of the pressure and the relative Mach along the span of the balde its possible to see the behaviour of the shock wave. Below are the results obtained from the analysis with the very fine mesh. From Fig. 3.12(a) and Fig. 3.12(b) it is possible to see the variation of the relative Mach and the pressure along the blade span. From Fig. 3.13, instead, it is possible to see the position of the shock wave at different spans of the blade. Finally, from Fig. 3.14 it is possible to see the distribution of the relative Mach on the blade respectively at LE and TE.

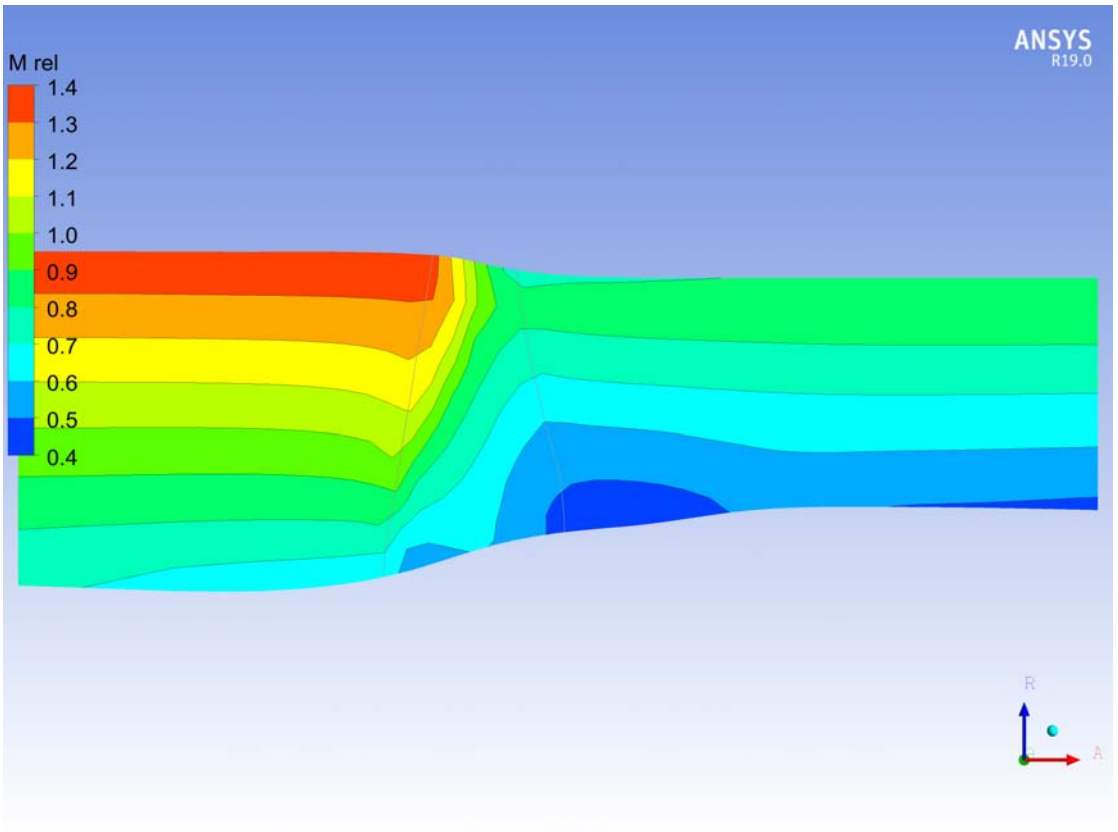

(a) Relative Mach

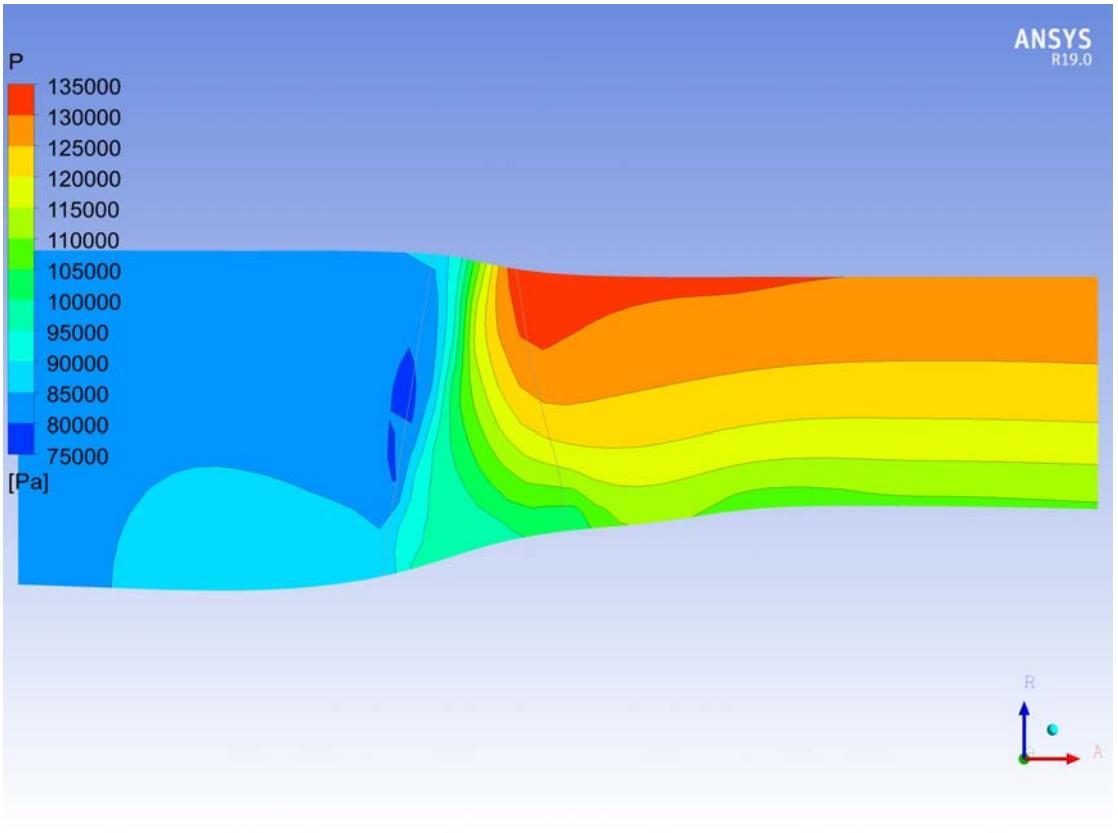

(b) Pressure

FIGURE 3.12: Pressure and Relative Mach Blade along the span

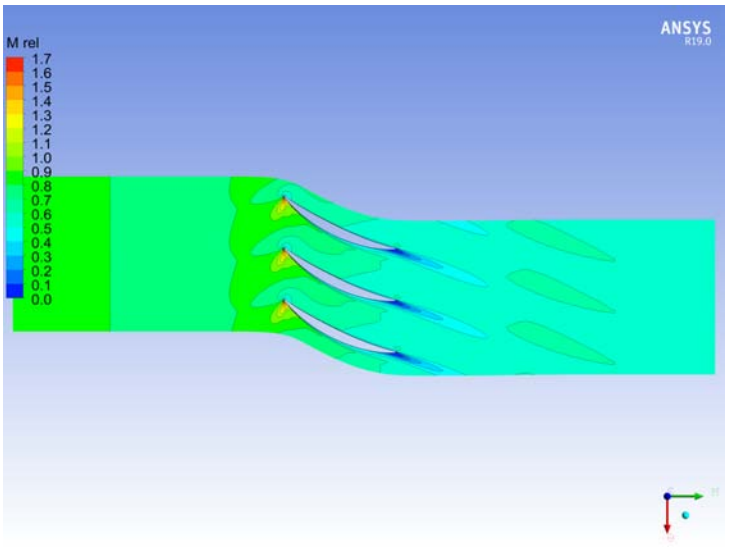

(a) Relative Mach at 20% span

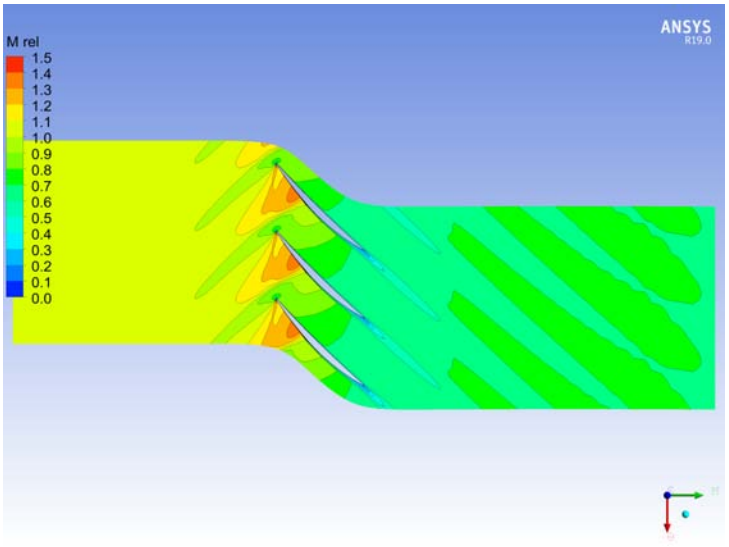

(b) Relative Mach at 50% span

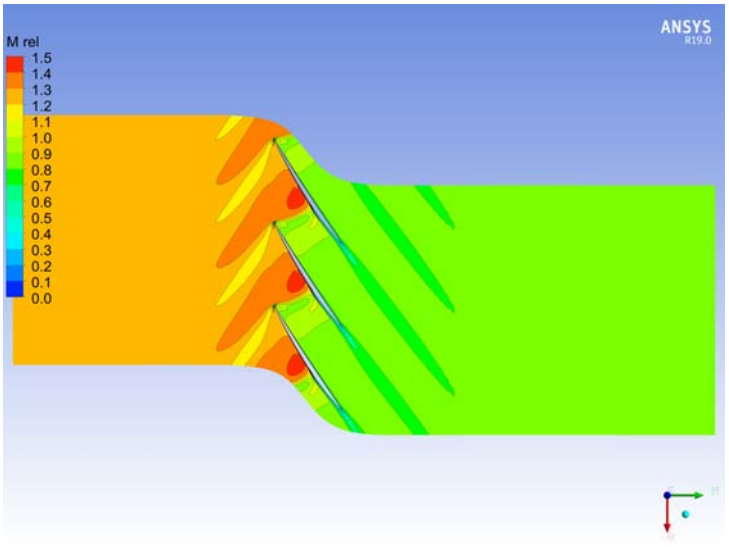

(c) Relative Mach at 80% span

FIGURE 3.13: Relative Mach at different span

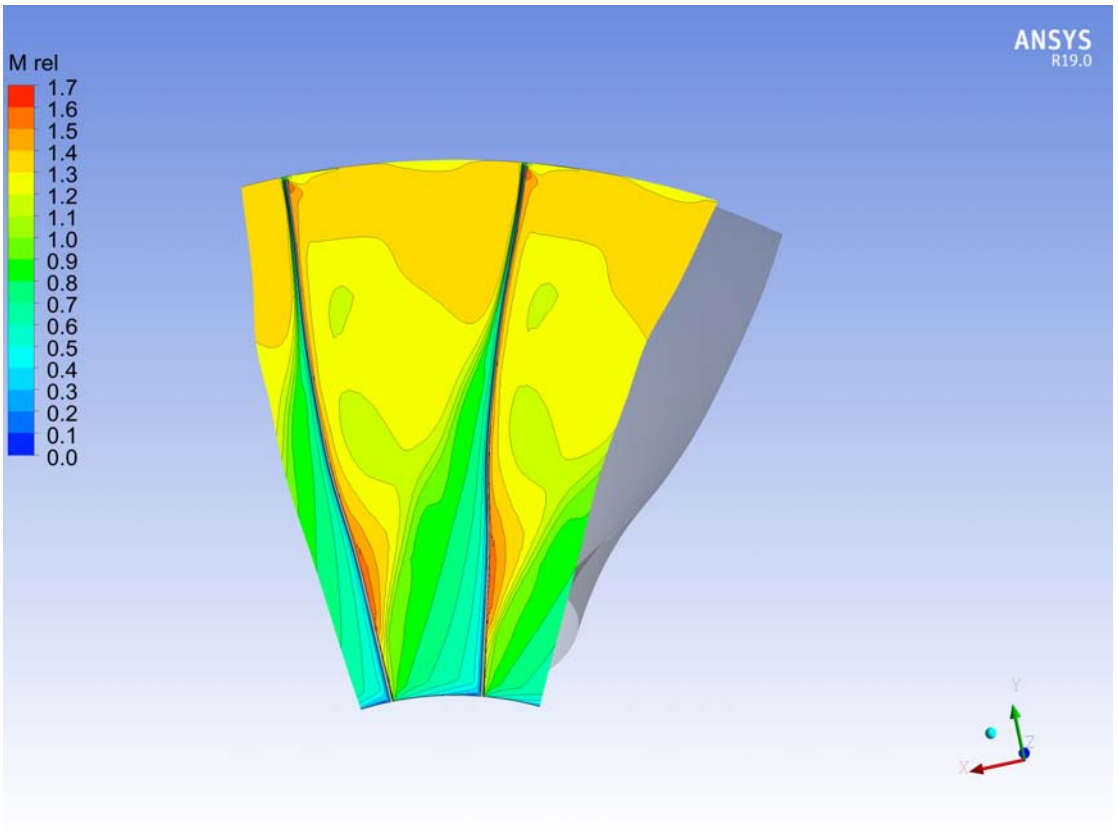

(a) Relative Mach at LE

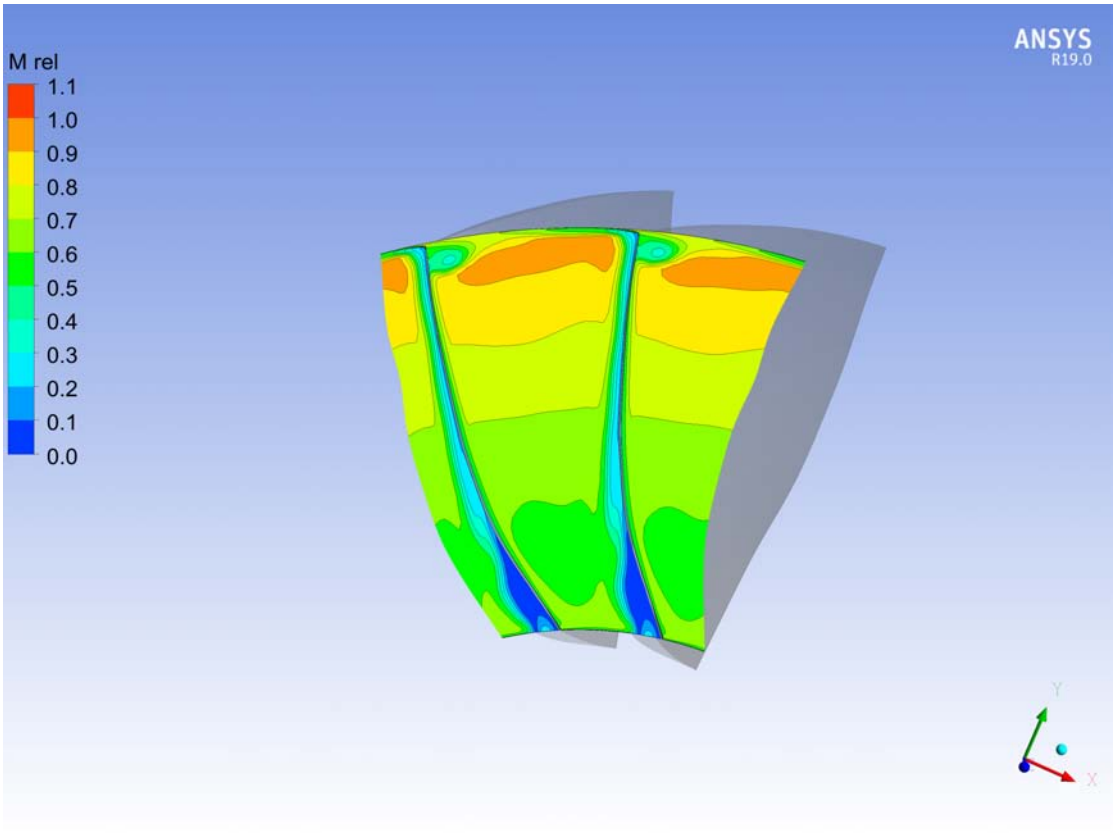

(b) Relative Mach at TE

FIGURE 3.14: Relative Mach distribution at LE and TE

For completeness, in the images below it is possible to see a comparison between the analysis carried out and the experimental data, and the operation of the compressor close to the choke and stall conditions. In the following figures the comparisons were made at 90% of the span.

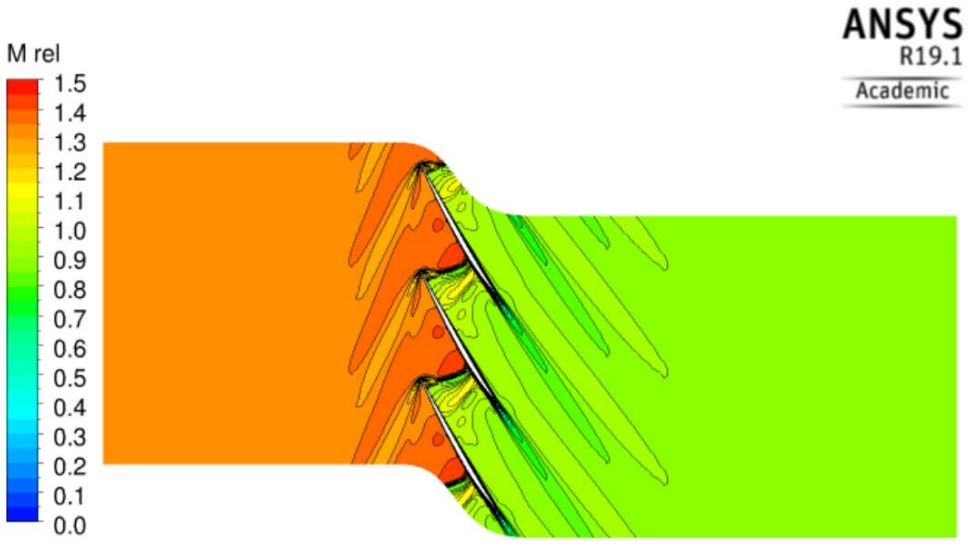

(a) Contour of M_{rel} at 90% near peak

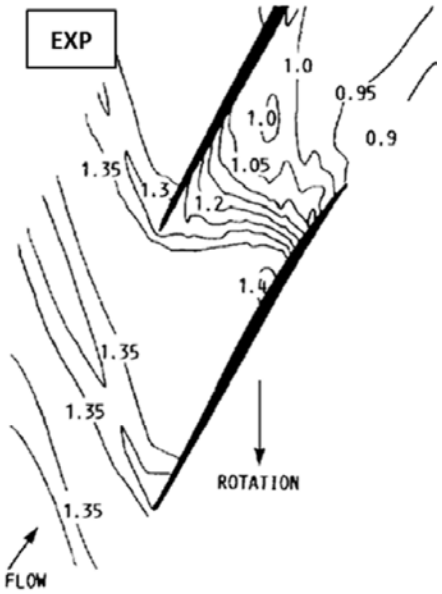

(b) Experimental blade to blade Contour of M_{rel} at 90% near peak

FIGURE 3.15: Comparison between contours of the relative Mach of experimental and CFD near peak conditions

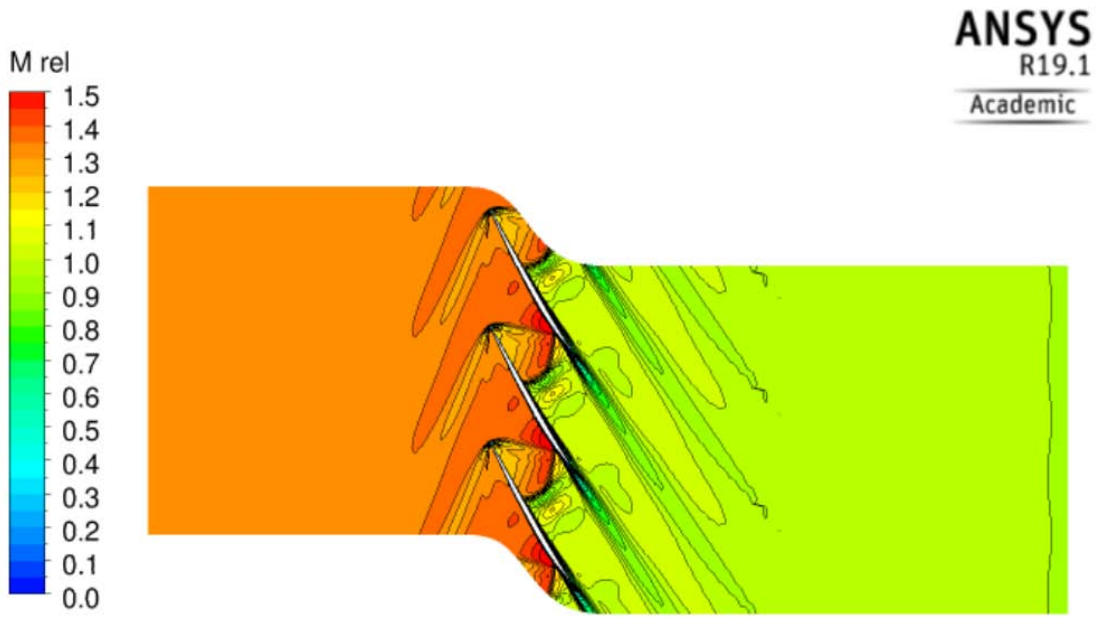

(a) Contours of relative Mach near choking conditions

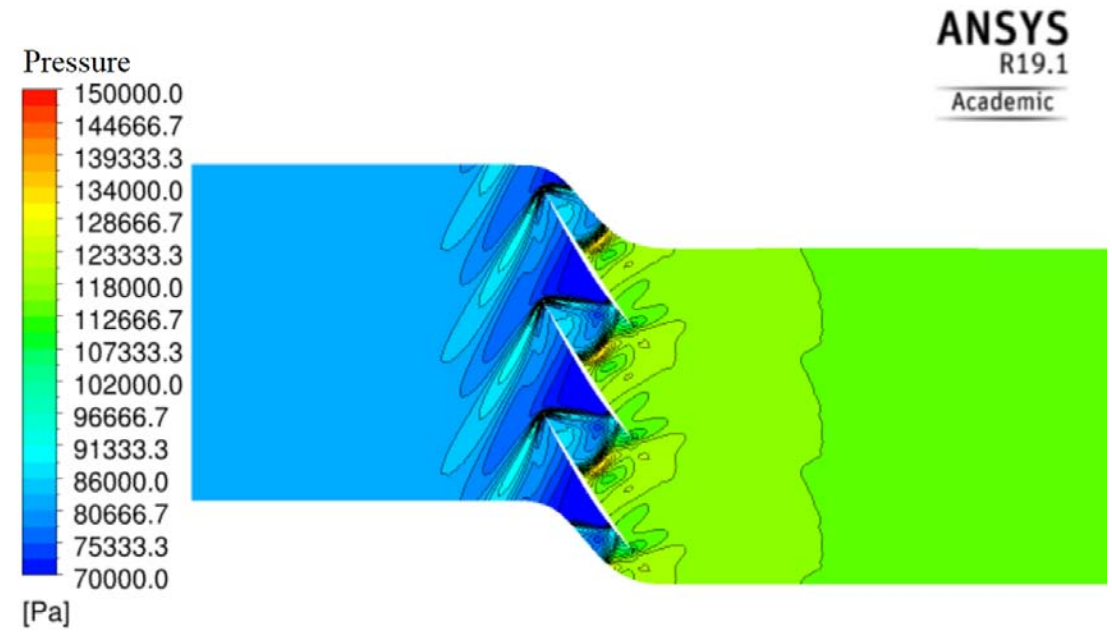

(b) Contours of Pressure near choking conditions

FIGURE 3.16: Contours of Pressure and relative Mach near choking conditions

3.3.1 Compressor Map

This section shows the calculation of the compressor map in order to get an idea of how the Rotor 67 works at different rotation speeds. This analysis was made in order to find the operating limits at the various speeds. To obtain this analysis Tridente [24] has chosen to use the model with the fine mesh because this has the advantage of obtaining good results with a fairly low computational cost. The time required is almost halved compared to the model with the very fine mesh (4 hours instead of 6). To draw all the lines on the map, the rotation speed is changed from 75% to 100% of the project rotation speed.

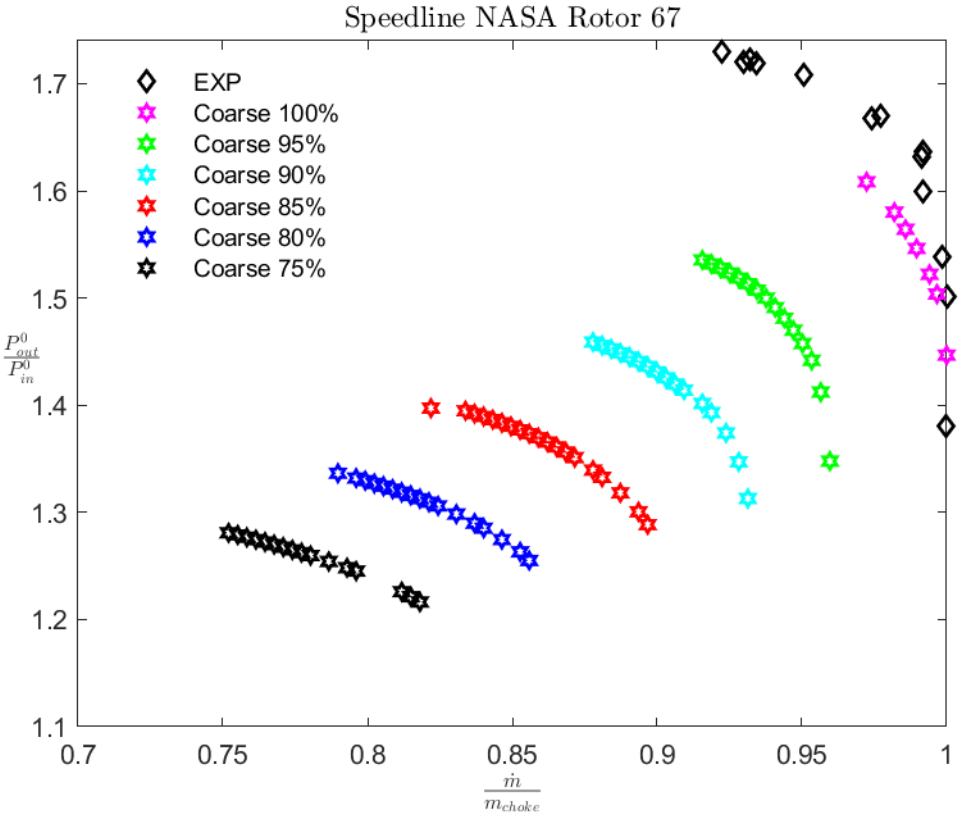

FIGURE 3.17: Compressor map NASA Rotor R67 [24]

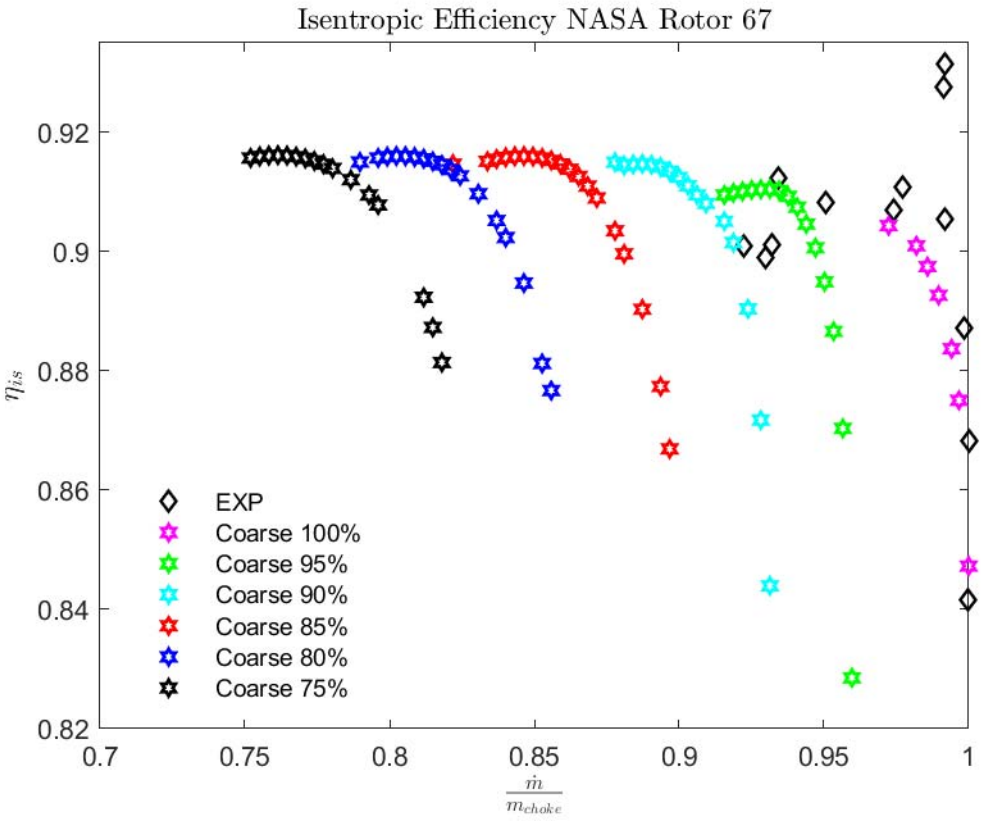

FIGURE 3.18: Isentropic efficiency NASA Rotor R67 [24]

Many results can be drawn from the results obtained by mapping the compressor. Firstly, even if it is not plotted, the stall margin is clear. Furthermore, the more the rotation speed increases, the further it move away from the vertical asymptote.

3.4 Full Annulus Analysis

The simulation of the entire Rotor 67, which means all the 22 blades, it is the first important step towards the study of the complete system which foresees the coupling of the transonic fan with the S-duct intake. In fact, it does not make sense to simulate the single channel downstream of the duct because the pressure profile is not uniform and, consequently, the rotor is influenced differently. One half of the rotor will in fact have the direction of the flow concordant with the direction of rotation, while the other half will have the direction of the flow contrary to the direction of rotation. This, as will be analyzed later, creates many problems during the optimization phase. A fundamental objective will be to understand the flow behavior and what it causes in terms of efficiency and overall performance

of the rotor operation. All these aspects will be discussed and analyzed in the following chapters. For the moment, the attention is focused on the analysis of the entire rotor and on the difference that could occur with the simulation of the single channel.

The two simulations as can be expected are very similar but there is a fundamental problem. The whole rotor is created by simply copying the single channel for the number of blades, however this procedure leaves an empty hole in the position of the rotation axis. This in the simple analysis of the rotor alone does not create problems as the flow inlet region is well defined, but creates significant problems when the system is coupled with the S-duct. In fact, an empty hole cannot be left in the center of the rotor because the program used for the simulation would close it with a vertical wall. This wall as can be expected makes no sense in the physics of the problem and creates significant problems with the flow.

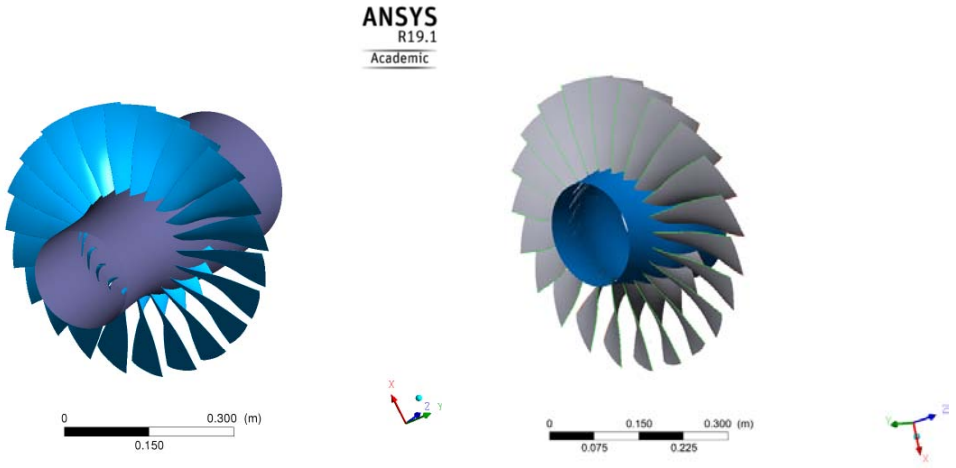

(a) Full annulus geometry of R67

(b) Full annulus geometry of R67 modified

FIGURE 3.19: Full annulus geometry before and after the change [24]

To pose a solution to this problem it was decided to implement an ogive upstream of the fan which has the duty to drive the air from the inlet towards the blades. This ogive was created by Tridente [24] and the attention in designing the ogive was not focused on its shape. In fact, the purpose was not to develop the nacelle to guarantee the highest efficiency possible but the aim was that the geometry gently drive the fluid without any detachment from the wall. In order to built this ogive, the geometry was drawn on SolidWorks and the mesh was made by using ANSYS workbench. But, before the finally coupling of ogive and fan the geometry of the latter has been modified to enable a perfect connection.

The Fig. 3.19(b) shows how the geometry was modified from the initial case of Fig. 3.19(a). This step was made with TurboGrid in which the region of inlet and outlet can be easily modified. As for the ogive, the geometrical dimension are known because they must match the fan's ones. The Fig. 3.20(a) and 3.20(b) show the geometrical shape of the ogive and its mesh.

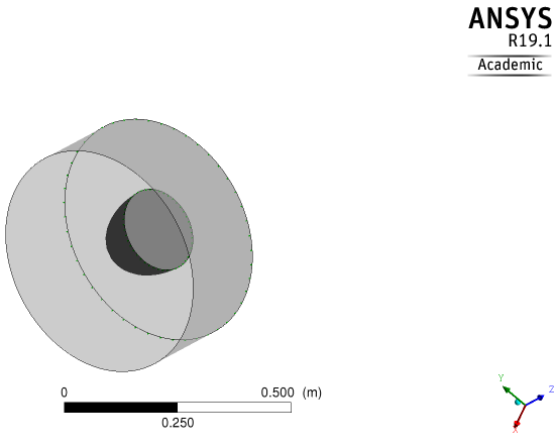

(a) Ogive upstream of the fan

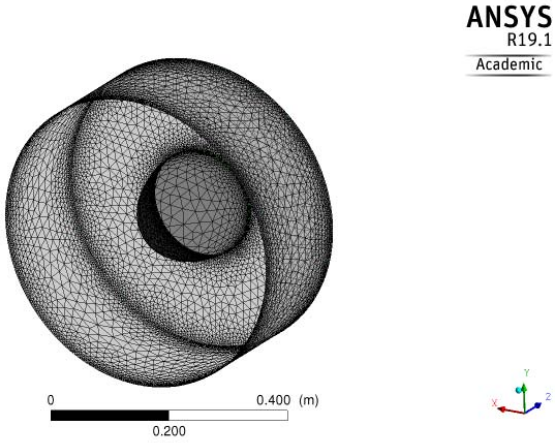

(b) Ogive's mesh

FIGURE 3.20: Full ogive geometry [24]

From the Fig. 3.21 it is possible to see how the two systems are paired together and which is the interface among them. There are three different domains in this system:

- Ogive
- Rotor 67
- Outlet

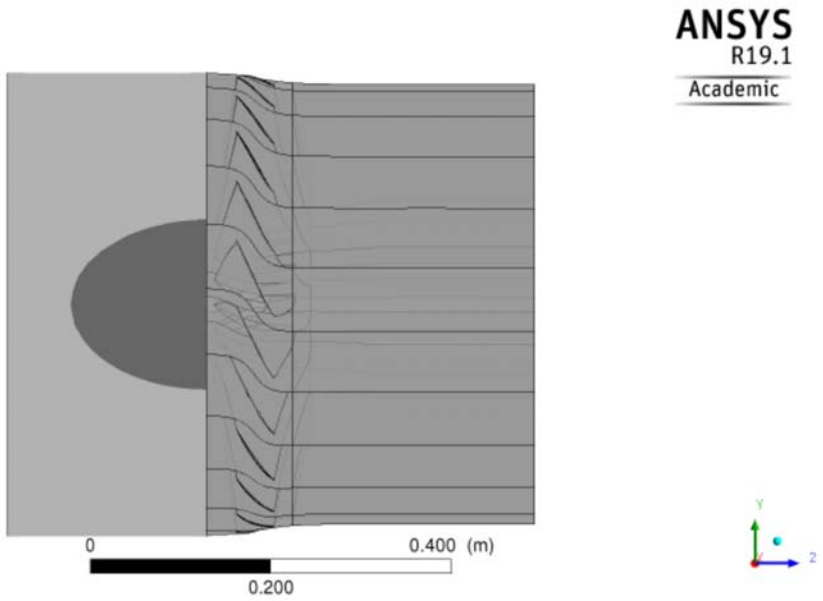

FIGURE 3.21: Entire component: ogive upstream plus the fan [24]

In the following table it is possible to see the differences between the single channel and the entire rotor

TABLE 3.5: Single channel and full annulus simulation features

Simulation	Mesh Model	No. of Nodes	CPU Cost	No. of Iterations
Single channel	Fine	1.6 mln	4 hours	3500
Full annulus	Coarse	35.2 mln	27 hours	1500

As for the analysis of the single channel, also with this simulation the compressor map was made. The aim was to highlight any differences. Furthermore, another goal of the simulation of the entire rotor was to validate its operation and then be able to couple it to the S-duct without problems. Fig. 3.22 shows the difference between the whole rotor and the single channel both at the operating speed of 95% and 100%. As you can see there are differences and the analysis of the whole rotor approximates reality better. This obviously, however, at the expense of the much higher computational cost. From the following tables it is possible to see out the main differences in accuracy between the models simulated.

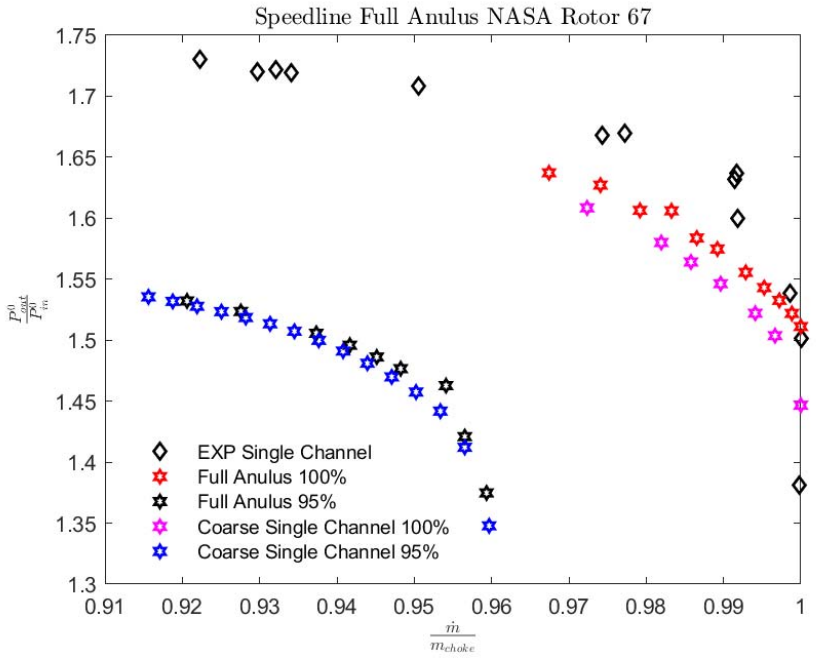

FIGURE 3.22: Comparison between single channel and full annulus simulations [24]

TABLE 3.6: Single channel and full annulus simulations near stall [24]

Simulation	$\dot{m}$ $[kg/s]$	$\Delta\dot{m}$	η_{is}	$\Delta\eta_{is}$
Single Channel Fine	33.2366	-	0.905865	-
Full Annulus	33.1807	+0.0559	0.906602	$-7.37e-4$

TABLE 3.7: Single channel and full annulus near peak [24]

Simulation	$\dot{m}$ $[kg/s]$	$\Delta\dot{m}$	η_{is}	$\Delta\eta_{is}$
Single Channel Fine	33.4226	-	0.911848	-
Full Annulus	33.4088	+0.0138	0.907245	$4.603e-3$

TABLE 3.8: Single channel and full annulus near choke [24]

Simulation	$\dot{m}$ $[kg/s]$	$\Delta\dot{m}$	η_{is}	$\Delta\eta_{is}$
Single Channel Fine	34.2867	-	0.888468	-
Full Annulus	34.2976	-0.0109	0.871416	+0.013264

All the previous tables show the differences between the entire rotor and the single channel subjected to different operating regimes. Since no analysis of the complete rotor has been found, the reference point is the experimental data obtained through the measurements. We can also take into account the results obtained by the single channel with the finest mesh. From Fig. 3.23, 3.24, 3.25 it is possible to observe how the pressure varies starting from the the stall, then near peak and finally to the choke condition.

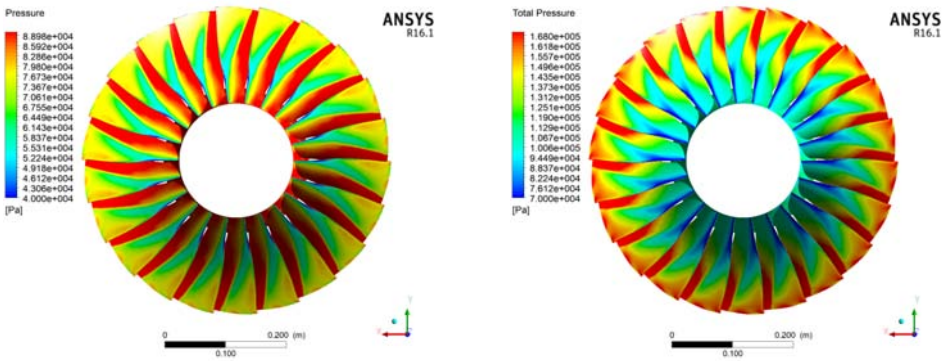

(a) Contours of static P for full annulus simulation

(b) Contours of P^0 for full annulus simulation

FIGURE 3.23: Near stall contours of static and total pressure for the full annulus simulation [24]

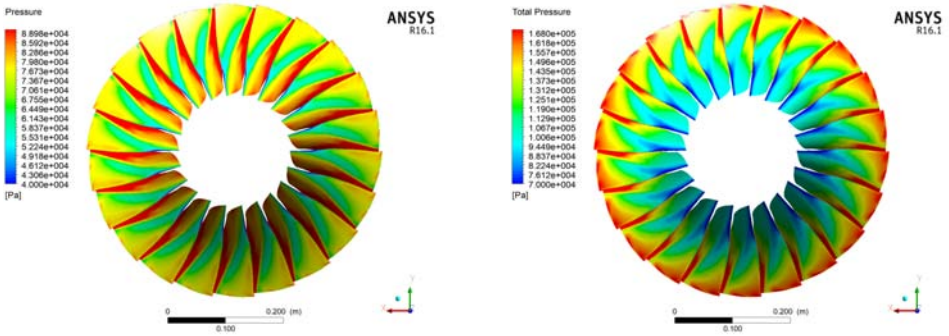

(a) Contours of static P for full annulus simulation

(b) Contours of P^0 for full annulus simulation

FIGURE 3.24: Near peak contours of static and total pressure for the full annulus simulation [24]

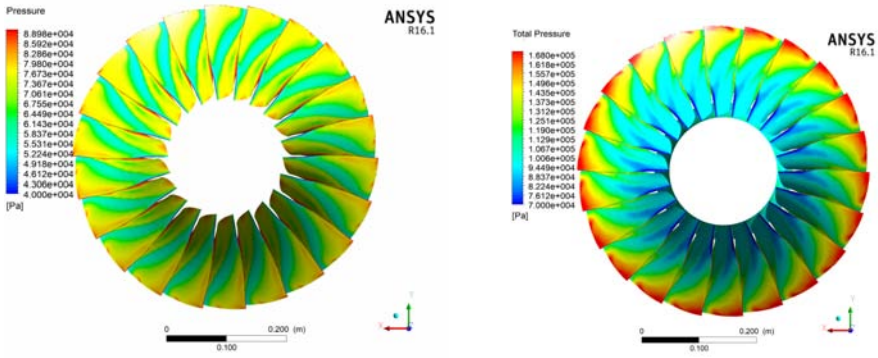

(a) Contours of static P for full annulus simulation

(b) Contours of P^0 for full annulus simulation

FIGURE 3.25: Near choke contours of static and total pressure for the full annulus simulation [24]

Chapter 4

S-duct and NASA Rotor 67 Baseline Interaction

In this chapter the work done by Tridente [24] is explained and reported. In fact, this work is the starting point of the work that I did during my period of study at the University of Cranfield. This chapter then explains how the simulation of the entire system is set up. The aim of Tridente's work was in fact to understand how the S-duct and the fan downstream of it can interact with each other. As can be seen later, the presence of the S-duct adversely affects the fan, creating a non-homogeneous flow which compromises the overall performance of the fan. The flow is said to be distorted by the intake duct and it is clear how a total pressure loss zone is created.
During his work Tridente performed three different simulations:

- entire system with S-duct baseline
- entire system with S-duct optimized (cp and DC_{60})
- entire system with S-duct optimized (cp and $swirl$)

The different S-ducts used by Tridente in the various analyzes have been optimized in accordance with Dal Magro [13] starting from the baseline geometry adapted by Dal Magro to the dimensions of the fan.

4.1 Inlet Distortion

In this section the flow distortion caused by the S-duct is under analysis. In fact, the aim is to understand how these losses could affect the overall fan performance. In the near future systems comprising intake ducts will be increasingly taken into consideration for the next generation of BLI [26] aircraft. In fact, positioning the engine inside the aircraft will provide significant advantages and therefore the use of S-duct will be necessary. As far as flow distortions are concerned, therefore, there are three main entrance distortions:

- velocity inlet distortion related with the swirl
- total pressure distortion due to the losses of friction on the wall
- total temperature distortion

These three different types of ailments involve three different effects on the fan. As for the first distortion, the swirl distortion is due to the non-axiality of the velocity. The speed at the entrance has, in fact, an angle in front of the blade. As it is concerned with both the total pressure and temperature distortion, they are considered to be radially or circumferentially distributed at the inlet of the fan.
As said in [27] the condition in which the flow is considered clean at the inlet is the one of most convenience for the design of the fan. But the reality of the facts proves that the rotor barely faces this situation, and the flow and its properties are never considered uniform. The inlet, in fact, is always experiencing disturbed condition due to multiple causes. This disturbed condition affects the performance in terms of pressure ratio, isentropic and polytropic efficiency. A. Naseri, M. Boroomand, and S. Sammak in [27] analyzed that "Inlet distortion patterns redistribute flow parameters over the compressor blades which could in turn alter the stability condition of the compressor and trigger rotating stall or surge". Considering all these aspects is of considerable difficulty and therefore many studies have been made with particular attention especially to the pressure and distortion of the swirl. So many of these studies, including [27] and [28] come to the conclusion that the swirl entails different consequences to the performance of the rotor:

- co-rotating flow helps to improve the stability of the compressor
- counter-rotating flow brings about a decline in the stability

Furthermore, both [28] and [27] have shown how the swirl and the total pressure distortion coexist at the same time, even if they are usually treated not at the same time. In the work done by Tridente [24] both of them are concurrently considered in order to represent as faithfull as possible the phenomenon.

4.1.1 Baseline Review

For the starting geometry of the S-duct, as mentioned above, it was decided to use the basic geometry of Delot [29]. The problem, however, is that the form developed by Delot was not created for practical use, but is only a tool to analyze how CFD codes can describe the phenomenon studied by Wellborn [30]. Trident [24], therefore, in agreement with Dal Magro [13] have decided to adapt the initial geometry to the size of the fan, in order to assemble the two systems together. The next step they had to overcome was to find the initial condition at the inlet of the S-duct in order to guarantee fan operation. In fact, for its simulations, Delot used 88744 $[Pa]$ as the input condition for the S-duct, but this condition is not compatible with the operating requirements of the rotor. This problem was overcome by Dal Magro [13] through a parametric study of the inlet total pressure so that the inlet total pressure to the fan was 101325 $[Pa]$. The choice of having this total pressure at the inlet of the rotor was dictated by the fact that, with this input, it is possible to compare the results of the fan performance with all the analyzes carried out previously. The parametric study was performed by varying the total inlet pressure so as to obtain a weighted average total pressure in the area at the suction outlet as close as possible to the desired one. To do this, the static rotor outlet pressure is provided by the analysis of the entire rotor. The total inlet pressure obtained from the study carried out, which satisfies the required requirement, was 106390 $[Pa]$. By means of this pressure, a total pressure is obtained as input for the rotor of 101341.08 $[Pa]$ which is very close to the desired one.

The Fig. 4.1 shows the results of the analysis conducted on the adapted basic geometry. These results are very similar to those obtained with Delot's original geometry. Although the behavior is almost identical, however, the pressure recovery factor is very different for the two geometries. This factor, cp, is a parameter with which the losses in total pressure are estimated and is expressed by

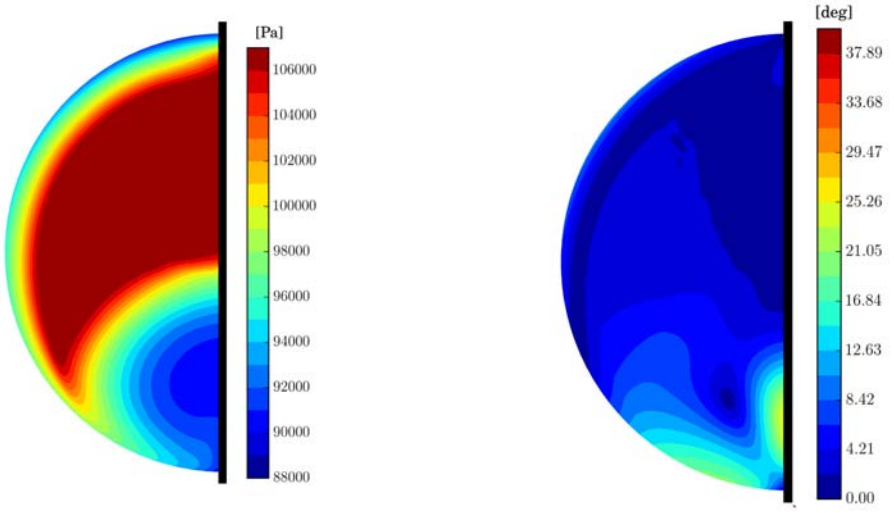

(a) *cp* (b) Swirl

FIGURE 4.1: *cp* and *swirl* representation of scaled basiline geometry

the following equation:

$$cp = 1 - \frac{P^0_{out}}{P^0_{in}} \tag{4.1}$$

In the previous expression P^0_{out} is the total pressure at the outlet interface and P^0_{in} is the total pressure at the inlet of the duct.

From the Table 4.1 it is possible to see the main differences between the two simulation. As demonstrated by Tridente and Dal Magro, in fact, even if the geometry is the same, the dimension are not, and the swirl angle and pressure recovery are highly different. This phenomenon can be explained since the boundary condition has drastically changed.

TABLE 4.1: Delot and adapted baseline comparison

Individual	*cp*	$\alpha[deg]$
Delot Baseline	0.0310	3.3978
Adapted Baseline	0.048042	4.73329

The Fig. 4.2 shows the cutting section of the S-duct through which you can see the trend and evolution of the flow along the entire length of the S-duct itself. As for the Fig. 4.2(a) the trend of the P^0 along the duct is in accordance the one of the Fig. 4.1(a) in the other symmetry plane. As for the Fig. 4.2(b) the velocity shows an interesting trend. There is, indeed, a bubble near the curvature of the duct in which the Mach number increases and approaches the sonic condition.

After the curvature, the velocity decreases and it is possible to see the growth of the boundary layer. It is possible also to see that the velocity in blu is negative, which underline the recirculation of the flow in that region.

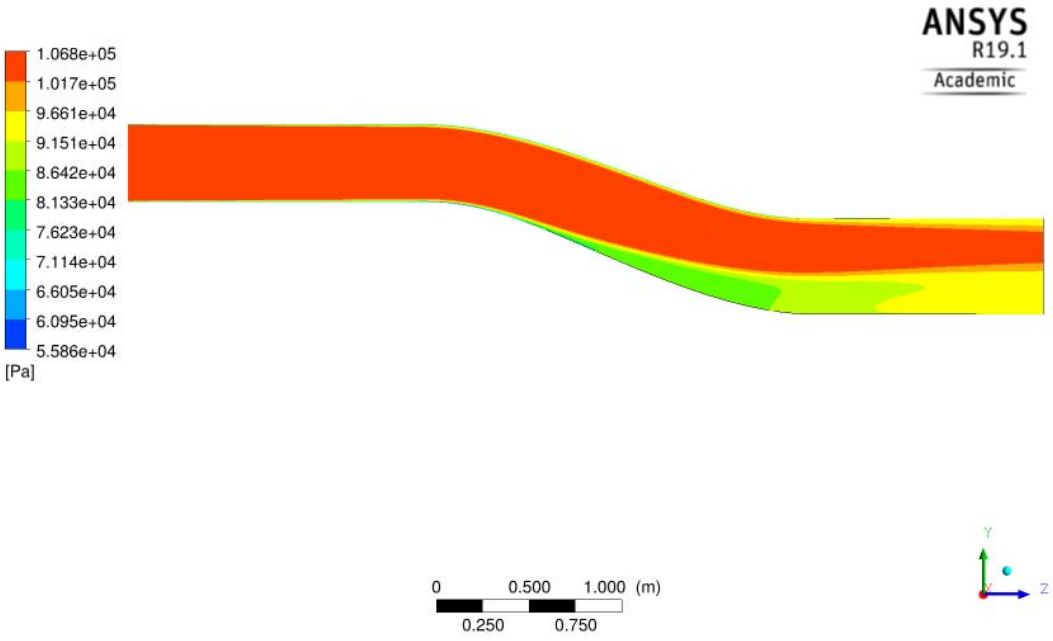

(a) Total pressure

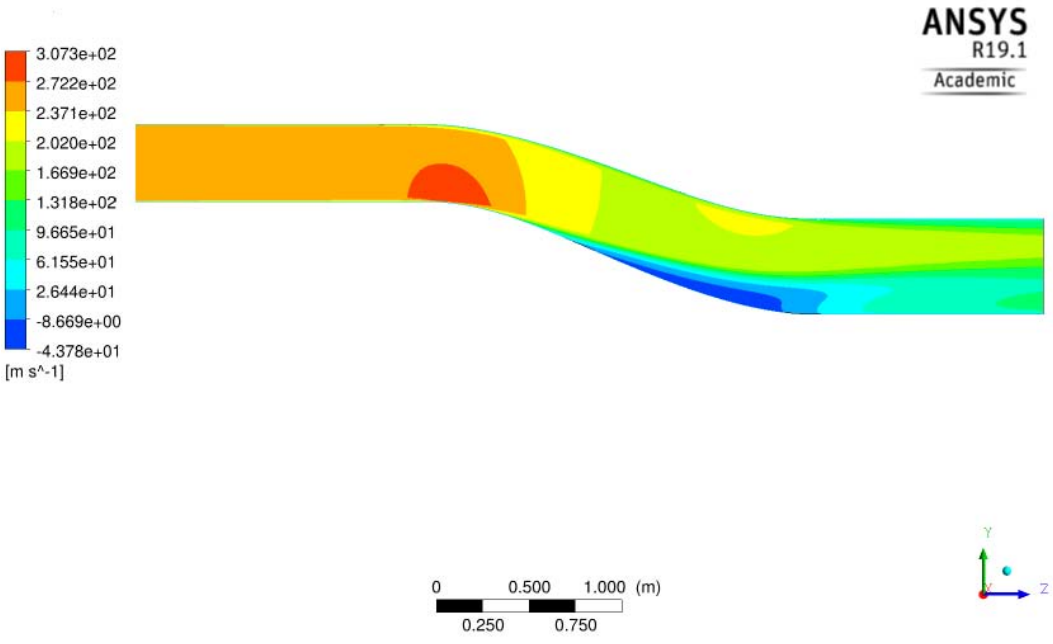

(b) Z-velocity

FIGURE 4.2: Total pressure and z-velocity on the symmetry plane representation of the adapted baseline

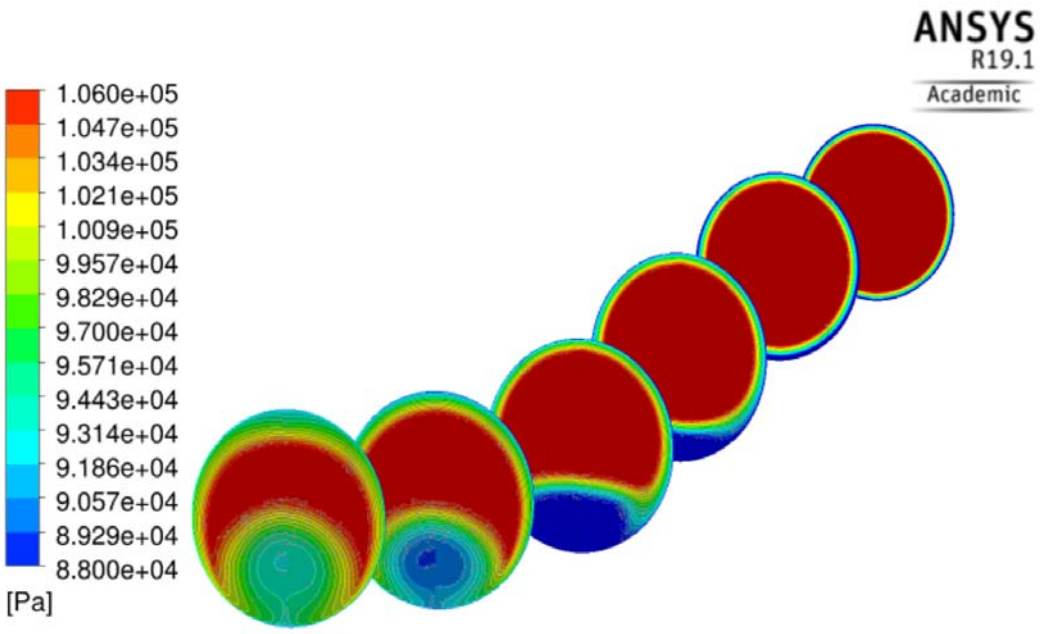

FIGURE 4.3: Isometric view of total pressure in different plane

The Fig. 4.3 shows 6 sections of the S-duct, from inlet to outlet, and how the distribution of the total pressure varies along the duct. From a uniform condition at the inlet, in which the contour is all red with a tiny blue circle, which highlights the friction losses at the wall, it passes to a outlet condition in which the profile is highly distorted. The plane of symmetry at the outlet is divided into two different region, the first one is ruled by an high pressure (red) and the second one is the light green region in which the pressure suffered a considerable drop. This non-equilibrium of the total pressure distribution is the cause of the non-axiality of the velocity, but, despite this, the average total pressure at the interface between the S-duct and the fan is that required for the correct operating condition.

4.2 Entire System

This section describes the analysis of the entire system and the parameters used for it by Tridente [24]. The entire simulationis was carried out on CFX, by exploiting the Delta cluster of Cranfield University. In this case, the simulation was carried out by using multiple nodes in parallel. This is due to the high computational cost, that the simulation required.

Indeed, the parameters of the simulation are:

- No. of Nodes 23e+6
- No. of Domains 4
- No. of Iteration 1500
- No. of CPU 64 cores
- No. of RAM 512 GB
- Computational cost 17 hrs

Due to the high computational cost and the high time required, it was decided by Tridente to analyze the system only at one speed line. So he didn't do the entire compressor map. The speed line that is taken into account is the 95% of the rotational speed. The domain of the system is split into four different body and each of these has been connected with an interface in CFX. Fig. 4.4 shows the entire system and all the four domains are visible. The four domains are in order: S-duct, ogive, fan, outflow. The analysis of the S-duct in [13] are done on half of the geometry in order to save time. In the case in question, instead, it is impossible because the fan is affected differently by the two halves of the S-duct. Therefore, the S-duct geometry has been revolved to complete the entire duct for the simulation.

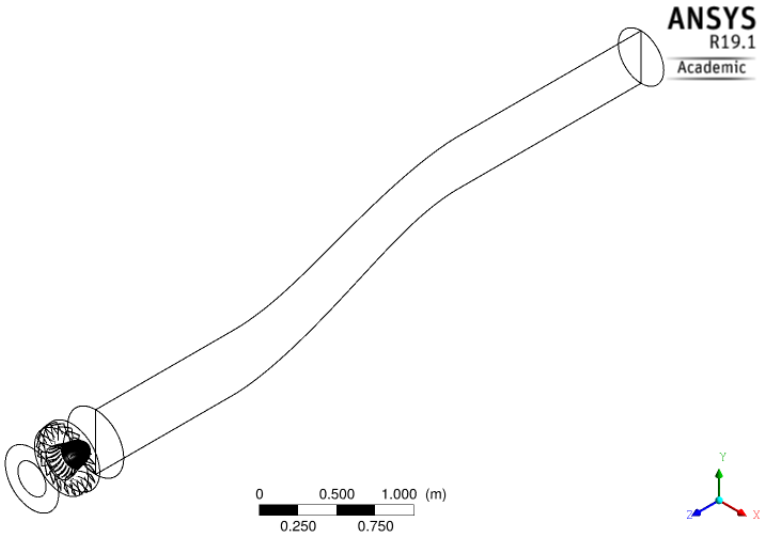

FIGURE 4.4: View of the entire system

4.3 Optimization with DC_{60} and cp

In this section the results of the optimization of the S-duct carried out in [13] are reported. The results obtained by Tridente [24] are also reported, in which it is possible to see the effect of S-duct optimization on the fan. To improve the flow out of the duct and therefore reduce the total pressure losses and decrease the level of distortion at the interface of the two components a multiobjective optimization is set up with the model MOTS (Multi Objective Tabu Search). The targets to be minimized, therefore, are the pressure recovery (cp) and the DC_{60}. The first parameter is linked with the reduction of the distortion of the total pressure, while the DC_{60} is related to the non axiality of the flow.

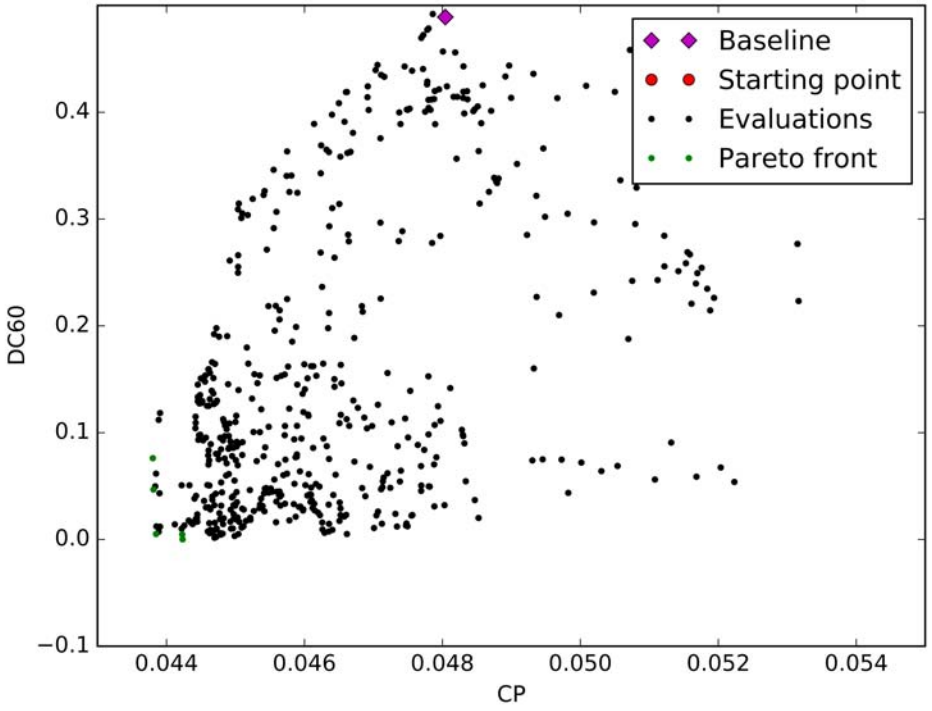

FIGURE 4.5: Pareto Front with DC_{60} and cp as objective function [13]

The Fig. 4.5 shows the Pareto Front obtained by Dal Magro [13] of the optimization carried out and it is possible to see how both of the two objective functions are decreased. To study the effects of these two optimized parameters on the fan, three different simulations were carried out by Tridente. One with the best cp, one with the best $DC60$ and one with the trade off geometry between the two parameters. The simulations were carried out only for the condition of maximum

efficiency and not for the entire rotor speed line due to the high calculation time required.

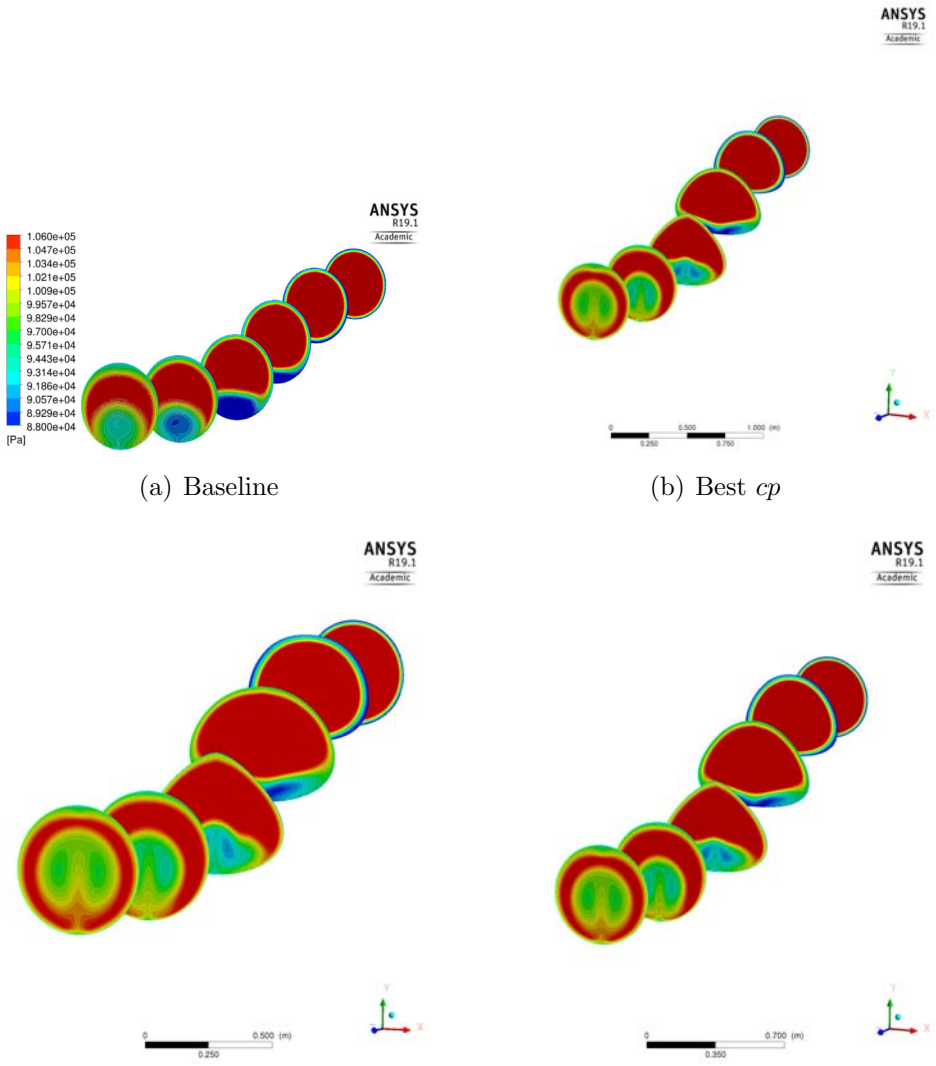

(a) Baseline (b) Best *cp*

(c) Best DC_{60} (d) Trade-off

FIGURE 4.6: Comparison between baseline geometry and optimized geometries

The Fig. 4.6 shows the variation of the geometry of the duct according to the parameter to be minimized chosen. As it is possible to see there is a big difference in the geometries. The shape is not drastically changed on the plane $y - z$, but this happened in the $x - y$ plane. In fact, the central cross section, the one that is most modified by the optimization, is no more circular, but it changes into different shapes (either elliptical or almost triangular). The outlet total pressure distribution, which is of our greatest interest, is slighly different from the baseline one. There is a higher pressure is positioned at the outer part of the section, and there is a central core with a slightly lower pressure. This is good because in the

whole circumference the pressure variation is very low. In fact, as it is possible to see, the outflow is much more symmetrical than before. This is to the advantage of the fan.

Table 4.2 reports the results for the geometries considered in terms of *cp* and DC_{60}. As it is possible to seen from the results reported, the variation of the parameters occurred with considerable effectiveness.

TABLE 4.2: Optimization with DC_{60} and *cp*

Individual	*cp*	DC_{60}
Baseline	0.04804	0.48912
Best *cp*	0.04380	0.07611
Best DC_{60}	0.04423	0.00167
Trade-off	0.04384	0.00507

Table 4.3 reports the comparison of the performance of the fan between the baseline and the optimized geometries. From the analysis of the results is possible to see that, in all of the three optimized geometries, the polytropic efficiency is improved, which means less losses. However, the π_c slightly decreases compared to the baseline geometry. This optimization process shows that the less is the *cp*, the higher is the η_{pol} increases.

TABLE 4.3: Performance of the optimized geometries

Individual	π_c	Rel. Error	η_{pol}	$\Delta\eta_{pol}$
Baseline	1.50000	-	0.885606	-
Best *cp*	1.49336	4.40e-3 %	0.890612	+5.00e-3
Best DC_{60}	1.49573	2.85e-3 %	0.890460	+4.85e-3
Trade-off	1.49327	4.48e-3 %	0.890584	+4.90e-3

The Fig. 4.7 shows in more detail the differences at the outflow between the basic geometry and the optimized geometries with the best *cp* and with the best *DC*60.

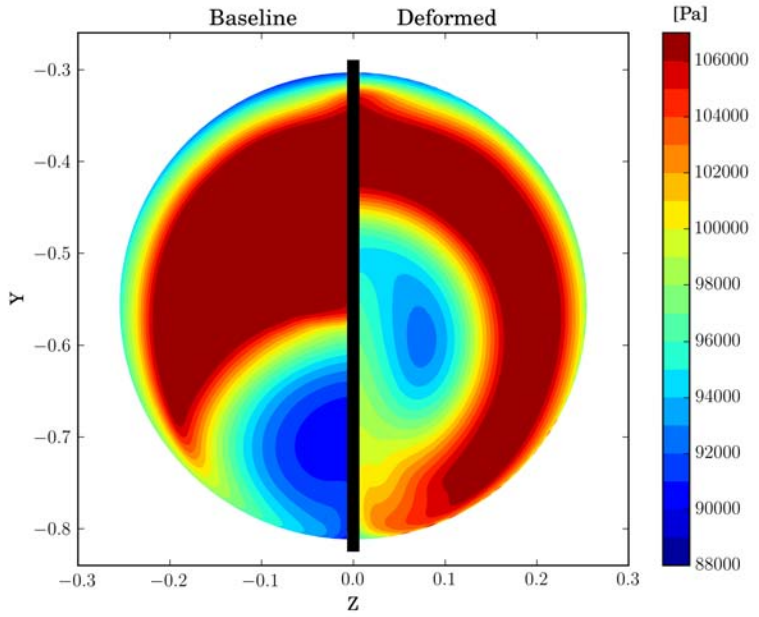

(a) Baseline and best *cp*

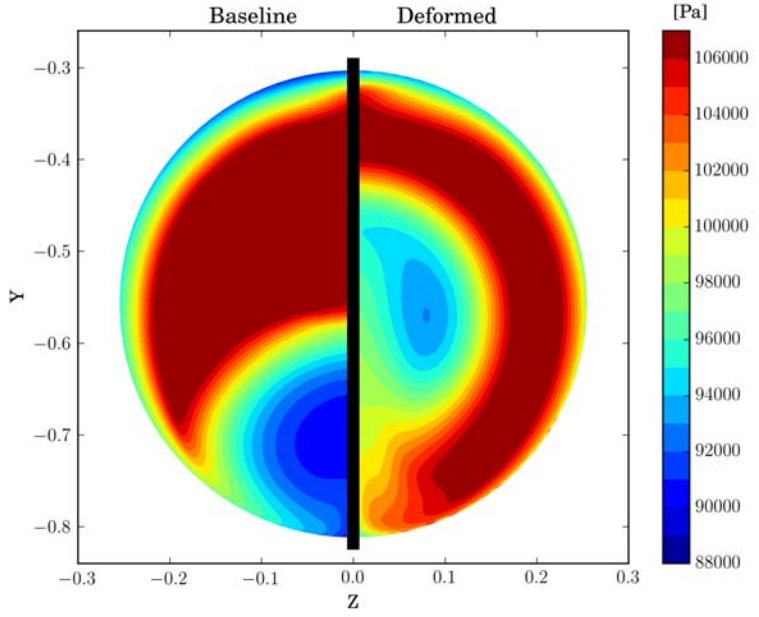

(b) Baseline and best DC_{60}

FIGURE 4.7: Baseline geometry and optimized geometries with best *cp* or *DC*60 [13]

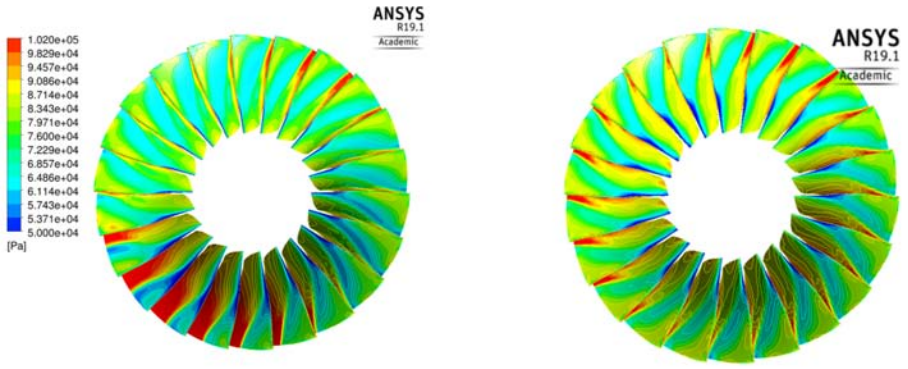

(a) Baseline (left) and best DC_{60} (right)

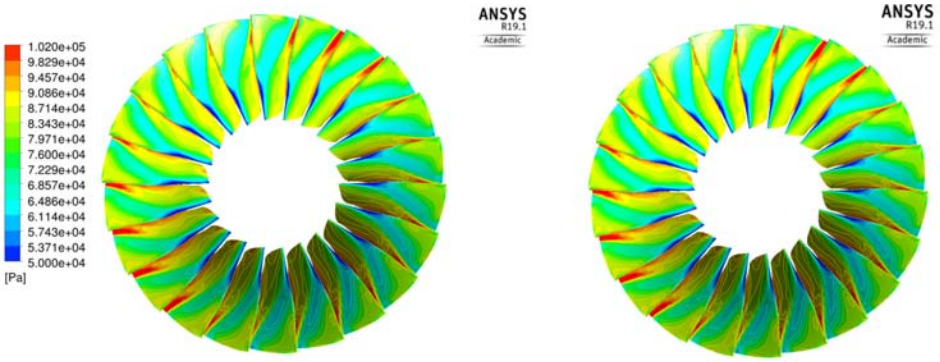

(b) Best *cp* (left) and trade-off (right)

FIGURE 4.8: Baseline and optimized geometries static pressure comparison

Analyzing the Fig. 4.8, which shows the results found by Tridente [24], it is possible to see how optimization process has decreased the distortion of the static pressure.The most interesting thing is that the red region in the lower left, which can be seen from the baseline geometry, has been greatly reduced. The distribution of the pressure is still distorted, but the level of distortion is utterly lowered. This fact leads to a marked improvement in the operation of the fan, in fact, as stated before, in all of the optimized geometries the η_{pol} is increased.

4.4 Optimization with *Swirl* and *cp*

This section reports the results of the second optimization carried out by Dal Magro [13]. Compared to the optimization discussed above, this has a different objective function, in fact the parameter α is analyzed, also called swirl angle. This angle is related with the non-axiality of the flow, that is, this is the angle at which the speed is distorted. Through the ducts obtained from this different optimization, Tridente [24] analyzed the fan performance. The results he obtained will be discussed later.

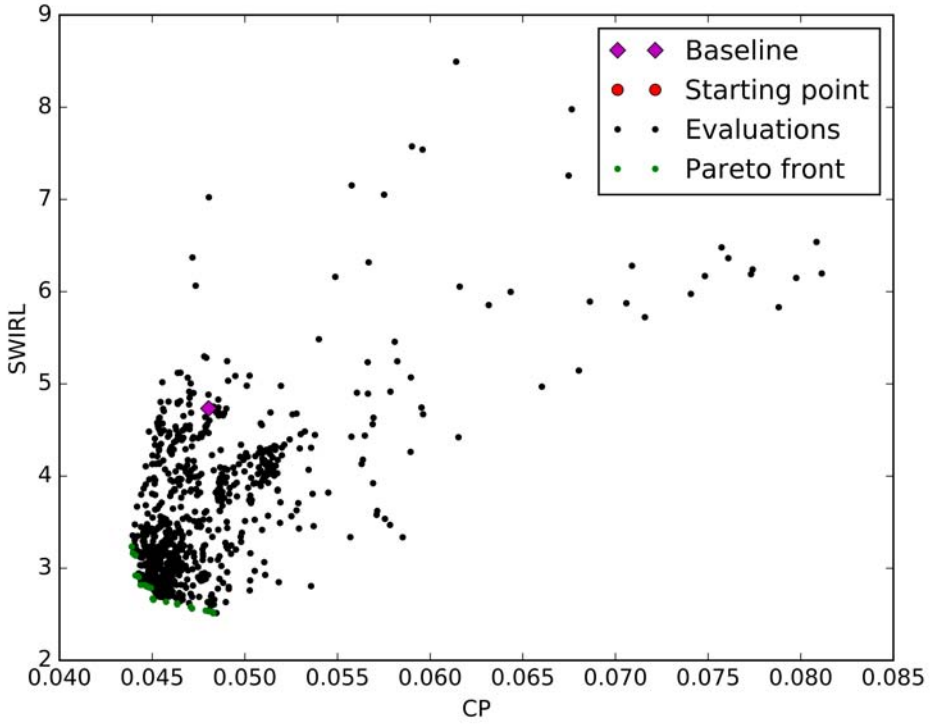

FIGURE 4.9: Pareto Front with α and *cp* as objective function [13]

In the Fig. 4.9 is possible to see the Pareto Front of the optimization obtained by Dal Magro for new objective functions. In this analysis more results were obtained but the improvement of the parameters is less evident than in the previous analysis. In fact, the swirl angle improvement is lower than the $DC60$ improvement. As for the pressure recovery factor, the optimized geometries present similar values with respect of the previous ones. For the comparison with the baseline geometry, was chosen by Dal Magro to simulate four different geometries. The results then obtained were compared with each other. To do this, either the best *cp* and α have

been selected and the two trade-off geometries. The results of these geometries are visible in the Fig. 4.10.

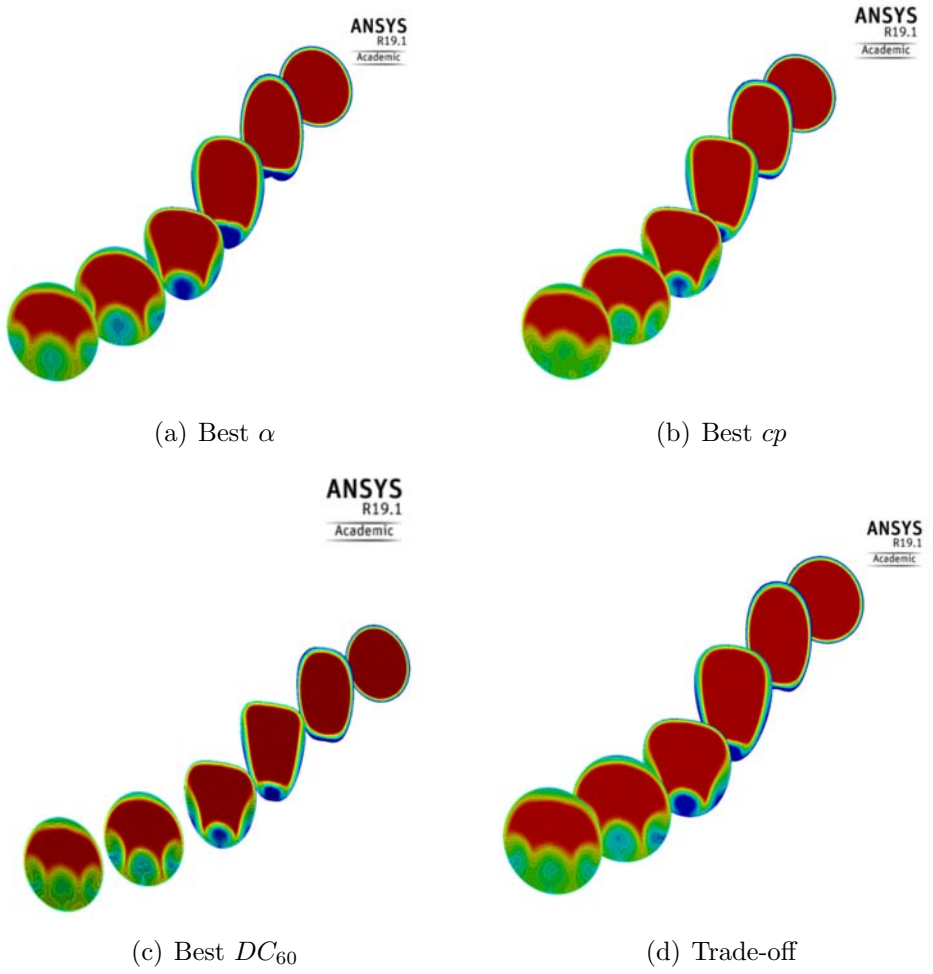

(a) Best α

(b) Best cp

(c) Best DC_{60}

(d) Trade-off

FIGURE 4.10: Comparison between baseline geometry and optimized geometries

As it is possible to see from the comparison between the optimized geometries and the basic geometry shown in Fig. 4.6(a), the central cross section is no longer circular, but varies along the curvature to minimize the two objective functions analyzed.

TABLE 4.4: Optimization with α and cp

Individual	cp	α
Baseline	0.04804	4.73329
Best cp	0.04389	3.23356
Best α	0.04829	2.51120
Trade-off (α)	0.04707	2.58174
Trade-off (cp)	0.04422	2.91428

The Table 4.4 shows the results obtained by Dal Magro [13] and it is clear how the results have improved, in comparison with the baseline geometry, allowing the fan to work in the best possible conditions.

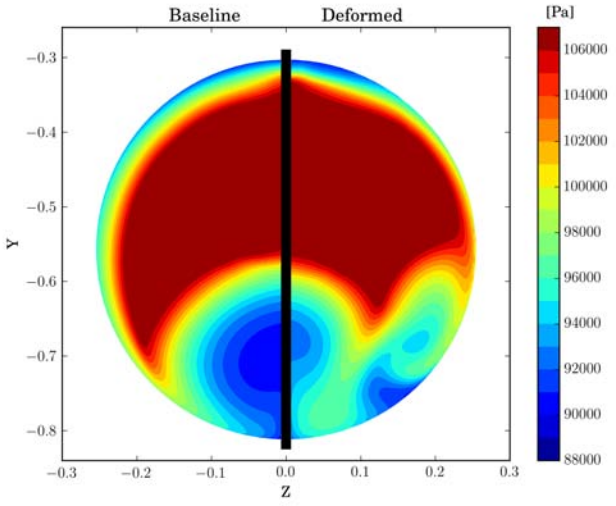

(a) Baseline and Best *cp*

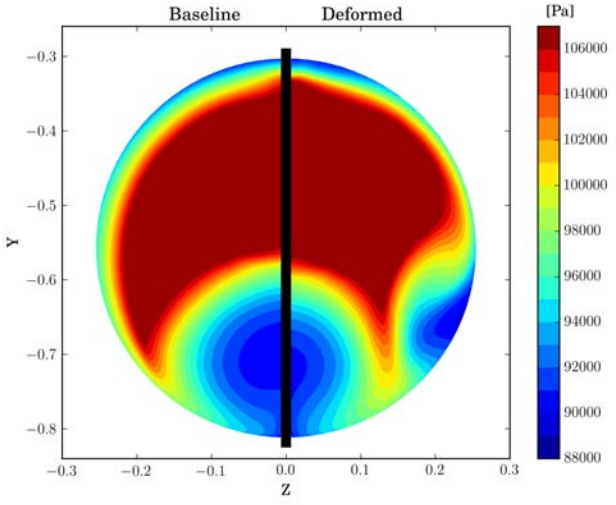

(b) Baseline and Best α

FIGURE 4.11: Baseline and optimized geometries with best α or *cp* [13]

Fig. 4.11 shows the comparison of the pressure distribution between the baseline geometry and the optimized geometries. From this comparison it can be seen that the pressure distribution is more similar to the baseline distribution than the distribution obtained from the previous optimization. This result does not benefit the operation of the fan, in fact this pressure distribution involves a different load for the blades. Some of these work under underloaded conditions.

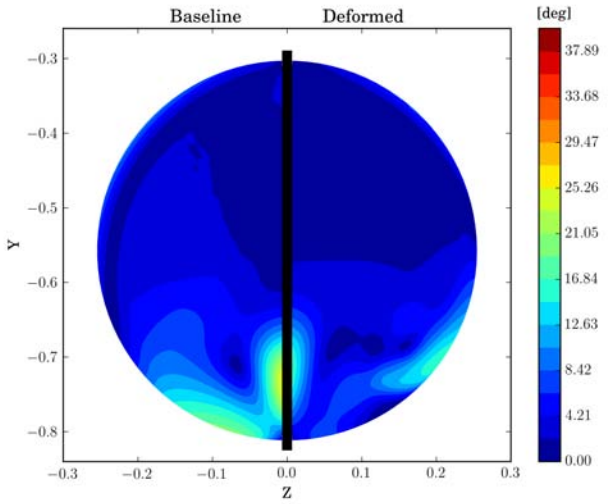

(a) Baseline and Best *cp*

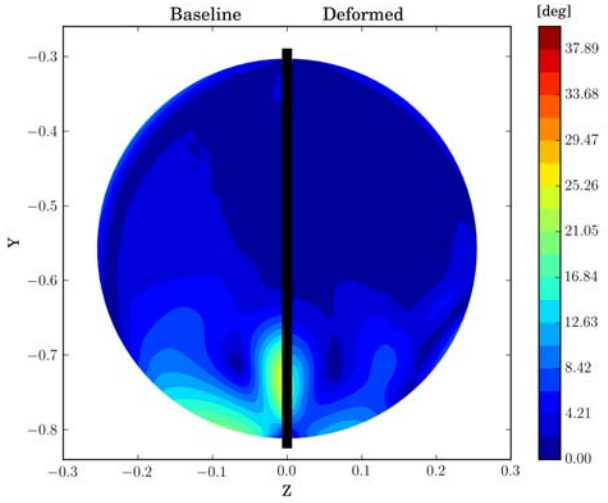

(b) Baseline and Best α

FIGURE 4.12: Swirl angle comparison between basic geometry and optimized geometries [13]

Fig. 4.12 shows that the swirl angle in the optimized geometries has lowered, therefore the flow is more axial and uniform than before.

TABLE 4.5: Performance of the optimized geometries

Individual	π_c	Rel. Error	η_{pol}	$\Delta\eta_{pol}$
Baseline	1.50000	-	0.885606	-
Best *cp*	1.49721	1.86e-3 %	0.888358	+2.75e-3
Best α	1.50323	2.15e-3 %	0.887988	+2.40e-3
Trade-off (*cp*)	1.50006	4.00e-5 %	0.889976	+4.37e-3
Trade-off (α)	1.50393	2.62e-3 %	0.888312	+2.76e-3

Table 4.5, obtained by Tridente with his work, reports the comparison of the performance between baseline geometry and optimized geometries. In all four analyzes there were improvements with respect to the basic geometry which led to an increase in polytropic efficiency. This increase means that there are fewer losses in the rotor.

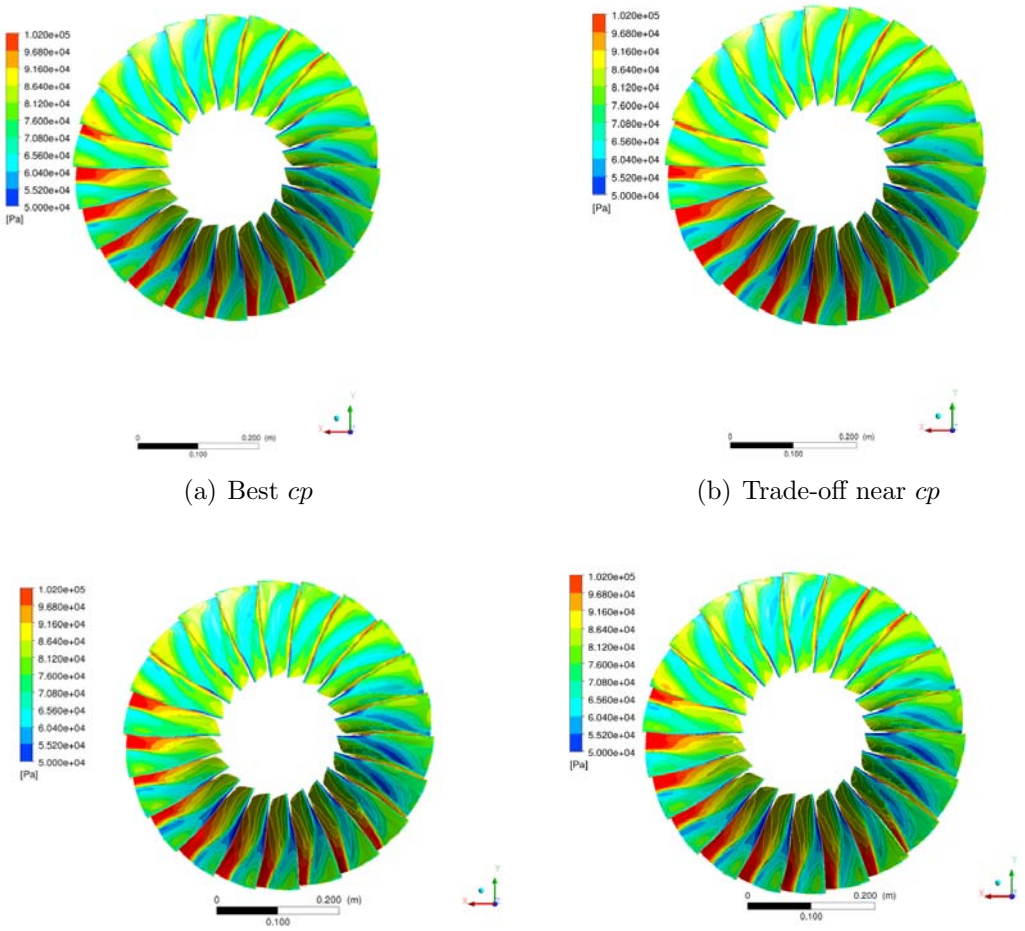

(a) Best *cp*

(b) Trade-off near *cp*

(c) Best α

(d) Trade-off near α

FIGURE 4.13: Baseline and optimized geometries static pressure comparison

As it is possible to see in Fig. 4.13 from the comparison of these four geometries, that it was obtained from the second optimization, with the basic geometry it is clear how the distortion is still present in the blades, even if it is less evident than the baseline S-duct. This aspect, as already mentioned, compromises the performance of the fan.

From the work done by Tridente [24] many conclusions have been drawn:

- both optimizations on the S-duct carried out by Dal Magro and therefore the new geometries obtained produce better results than the basic geometry
- the first optimization taken into consideration generates results in which the distortion is lower on the fan blades and this improves the overall performance of the rotor
- the parameter that showed the greatest improvement and that improved the performance of the rotor is the *cp*, because it increase the polytropic efficiency with respect of the baseline
- the objective function that returned the best results is the DC_{60} rather than the α, because it is able to reduce more the losses and the distortion of the total pressure

Chapter 5

Multi Objective Optimisation

In this chapter the aim is to give a general knowledge of optimization problems. These processes can be found in many fields of study, from engineering to economics to even agriculture. An optimization problem is solved through the use of repetitive calculation cycles (loops). These cycles are automated and continue until the set goals are reached. Optimization cycles are usually composed of three main processes: design analysis, results evaluation and new design creation. The design analysis process consists in analyzing the response of a given system when it is subjected to certain input parameters. The results evaluation process, on the other hand, is used to check if the results are optimal at the end of the process. Finally, the new design creation process aims to create a new design for subsequent iteration. To perform these last two steps, the optimization cycle needs efficient algorithms in order to reduce the computational cost. In addition to this, many constraints must be taken into account in an optimization process. For example, as in the case carried out in this thesis, the rotor blade, if very thin, offers good performance but if it is reduced beyond a certain thickness, the blade will break. Speaking now in mathematical terms, an optimization process can be described as follows: let's consider an independent variable $x \in \mathbb{R}$ called design variable, and consider an objective function $f(x)$, the aim of a optimisation process is to automatically modify the design variable in order to find a certain x^* such that $f(x^*)$ is a global minimum or maximum of the system based on the problem that is being analyzed. In a general case, x is built to be a design vector of design variables $\mathbf{x} = (x_1, \ldots, x_n) \in \mathbb{R}^n$. The optimization, according to the form it takes, is called single objective (SOO) if only one objective function is the objective to be

optimized, or is called multi-objective optimization (MOO) if there are multiple objectives.

5.1 Formulation of the Optimization Problem

At the beginning of an optimization process the most complicated part is the selection of design variables, objective functions, constraints, models and uncertainties.

- **Design variables**: the design variables are called in this way because they are parameters that have the task of modifying the shape or properties of the model taken into consideration. However, these variables usually have to respect a specified range. This interval is defined during a sensitivity or optimization design study. This limit is imposed to prevent the shape from being changed in unwanted ways or from not respecting the constraints of the process. In the case of studies of this thesis the control points of the parametrized blade can be considered as design variables.
- **Constraints**: a restriction or a limit that must be satisfied that is imposed by the designer is called a constraint. There can be many types of constraints, some can be rigid or that cannot be overcome, others can be soft or rather that have a range of variation. For example, the constraints in the design of a blade can be related to the production itself or to the characteristics necessary for the blade to withstand the operational load to which it is subjected during its operation.
- **Objective functions**: a mathematical equation that describes the final aim of the optimization process is called objective function. This objective generally corresponds to the maximization or minimization of a parameter which can correspond, for example, to the maximization of certain performances or to the minimization of losses. Many optimization processes have only one single objective function, but usually the optimization processes are multi-objective, in this case the well-known Pareto Front is obtained.
- **Models**: optimization models can be classified by differentiating them according to the types of constraints and the types of objective functions. There are four main types of optimization problems: unconstrained, linear, quadratic, nonlinear. These models differ in that they can be empirical or

theoretical models. The type of model chosen by the designer determines both the accuracy of the solution and the computational cost. A very accurate model consequently entails a high computational cost.

- **Uncertainties**: the uncertainties are deficiencies that can occur in an phase or activity of the modelling process. These deficiencies are usually due to lack of knowledge. To get a good explanation of the uncertainties, it is advisable to view the work done by Scaramuzzi [31].

5.2 Multi-objectives Problems

Once all the design variables, constraints, objectives and models have been set, the optimization process is defined and it is possible to proceed with the realization phase of the automatic calculation loop.

An objective function is described as $f(\mathbf{x})$, where $\mathbf{x} \in \mathbb{X}$ represents vector of design variables. A multi-objective optimization problem want to minimise or maximise a set of objective functions $[f_1(\mathbf{x}); f_2(\mathbf{x}); \dots f_m(\mathbf{x})]$ where $\mathbf{x} \in \mathbb{X}$ represents a vector of design variables. As it is possible to see below a deterministic multi-objective minimisation problem is formulated as:

$$\begin{cases} \min\limits_{\mathbf{x}} [f_1(\mathbf{x}); f_2(\mathbf{x}); \dots f_m(\mathbf{x})] & \forall\, \mathbf{x} \in \mathbb{X} \\ s.to & g(\mathbf{x}) \leq 0,\ h(\mathbf{x}) = 0 \end{cases} \tag{5.1}$$

where $g(\mathbf{x})$ and $h(\mathbf{x})$ are constraints vectors and $\mathbb{X}$ is the design space.

5.3 Classification of Optimization Algorithms

In an optimization process, the choice of the algorithm plays a fundamental role. In fact, the purpose of the algorithm is to decide how to modify the design parameters. There are different typologies of algorithms:

- Exact algorithms: these algorithms solve the optimization problem with the aim of finding the exact mathematical solution. Finding the exact mathematical solution, however, is not always possible and is a time-consuming process.

- Heuristic algorithm: heuristic means solving the optimization process by trial and error. These algorithms are designed to solve the problem by sacrificing accuracy, precision and completeness to get the solution in the shortest possible time. These are generally used when solutions with a certain degree of approximation are sufficient and when the exact solutions are computationally too expensive.

- Metaheuristic algorithms: metaheuristics is an evolution of the previous algorithm and performs better. A definition of metaheuristic algorithms is given by Glover [32] who considers them as a "main strategy that guides and modifies other heuristics to produce solutions in addition to those normally generated in the search for local optimality".

5.3.1 Metaheuristic Algorithms

In the work done by the author it was decided to use the metaheuristic algorithms. This choice was dictated by the fact that the problem is very complex and these algorithms guarantee correct solutions with a much shorter calculation time than the other algorithms. In these algorithms there are two major components: intensification and diversification, or also called exploitation and exploration. Diversification has the task of creating different solutions with the aim of extending the research space, while intensification has the task of focusing the research locally [33]. A good compromise between intensification and diversification is necessary to improve the rate of algorithm convergence. To obtain an intensification and differentiate the design space the algorithm makes a decision based on:

- Non-preference methods: the new design is randomly selected without the use of a specific strategy

- Priori method: the designs are choose before getting the results of the simulations.

- Posteriori method: the new design is selected after each iteration by analyzing the results obtained.
- Interactive methods: these methods have the advantage of allowing the user to interact with the simulation while it is in progress, so as to be able to guide the solution towards the desired result.

There are many types of metaheuristic algorithms that allow you to create an optimization process. Some of these are:Simulated Annealing, Genetic Algorithms, Differential Evolution etc.... To carry out the optimization process required in this thesis, it was decided by the author to use the GA genetic algorithm.

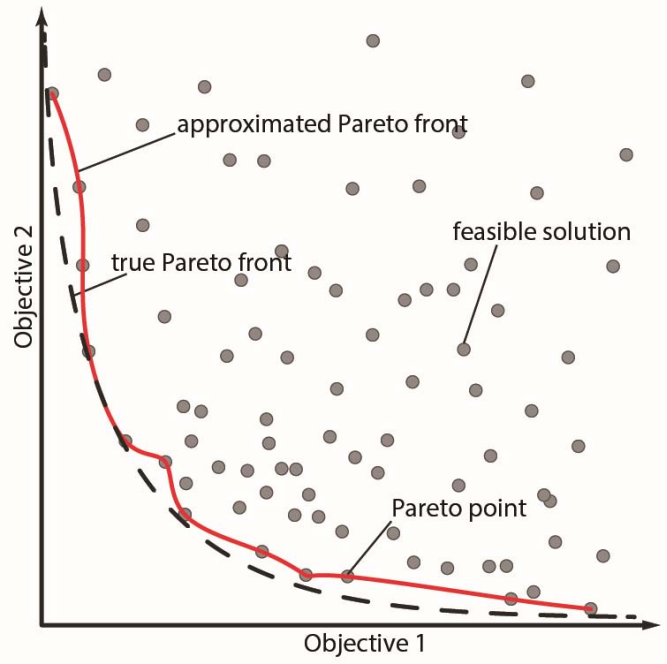

FIGURE 5.1: Pareto Front

5.4 Genetic Algorithm

The Genetic Algorithm (GA) is the most common and most used evolutionary algorithm in aerodynamic optimization problems because:

- "do not require the computation of gradient and can tolerate even more approximate or noisy design objective evaluation" [34];

- "can be efficiently parallelized and can take full advantage of the massively parallel computer architecture" [34];
- "can directly approach to a multi-objective optimization problems" [34].

Genetic Algorithms are created following the example of the mechanisms of natural selection. In fact, they use the survival of the fittest to finally obtain the optimal individual. A population consists of a fixed number of individuals, and each one is represented by a binary string, containing all values of parameters. In Fig. 5.2 is possible to see the reproduction mechanism used by GA. About its operation, a starting population is created and its genetic material is manipulated and modified by a reproduction mechanism Fig. 5.2. The result of reproduction is new individuals and this individuals compose the new generation. These individuals are in competition, and who adapt better to the environment, in other words, they have more chance to survive and to hand down their gene pool. The population evolves from generation to generation, increasing the average fitness of the individuals. At the end of the process the resulting population is the most suitable and responds best to the required characteristics.

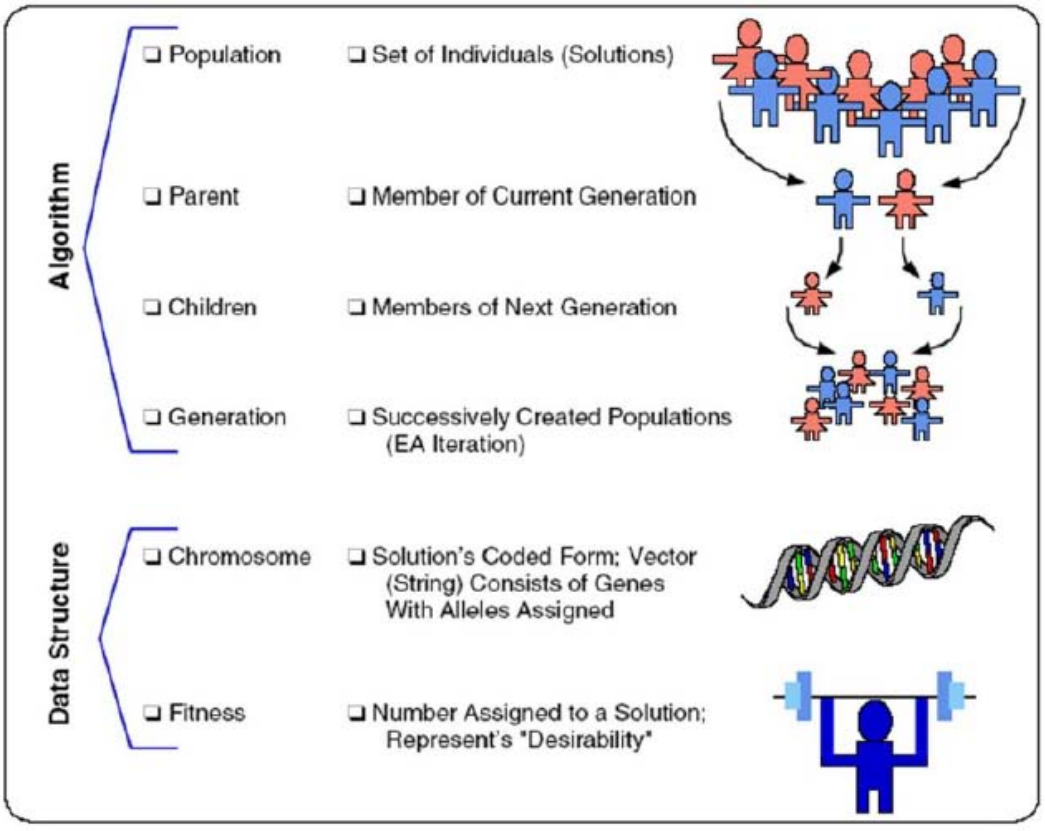

FIGURE 5.2: GA reproduction mechanism

5.4.1 Binary String

As said before in a genetic algorithm, each individual is represented by a binary string. It is possible to define a number of bits per parameter based on the precision and accuracy required to define the parameter. Hence, a value x ($x_l < x < x_u$) can be rounded by a binary string $\mathbf{S} = (b_q, b_{q-1}, \ldots, b_1, b_0)$ defined as:

$$x = x^l + \frac{x^u - x^l}{2^q - 1} \sum_{k=0}^{q} 2^k b_k \tag{5.2}$$

5.4.2 GA Operators

In the process of reproduction, genetic algorithms use three different operators:

- Selection
- Reproduction
- Genetic Mutation

5.4.2.1 Selection

The selection operator makes a choice of individuals based on the strength of their fitness value. There are two main methods for choosing individuals and these are: tournament selection and roulette wheel selection. For the first method, tournament selection, s individuals are chosen randomly in the initial population, and the best among them is selected as the first parent. The second parent is selected in the same method. The parameters s is called tournament size. Very high values of the s parameter mean a more elitist selection, while a low values allow less fit parents to be selected and this result in a more diverse population. The s choice, therefore, influences the exploration and the performance of the algorithm. In [35] is proposed to use $s = 2$. As an alternative to this method, a roulette wheel selection can be used. Fig. 5.3 show this method, it is possible to see that the number of parts of the circle represents the number of individuals, and the size of each part symbolizes the fitness of each individual.Therefore, the probability to choose one individual is directly proportional to his fitness value.

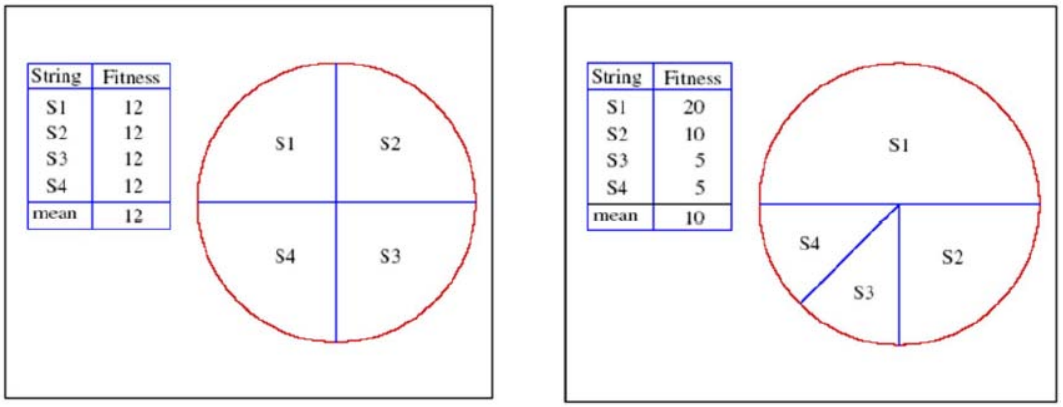

(a) Equal fitness (b) Unequal fitness

FIGURE 5.3: Roulette method of selection

5.4.2.2 Reproduction

The reproduction operator has the aim of mixes the parent genes. A necessary and indispensable function for the proper functioning of the algorithm is the crossover. It consists of a random counter that chooses a random point in the binary string. In this point, the two strings of the two individuals are broken and exchanged, as shown in Fig. 5.4.

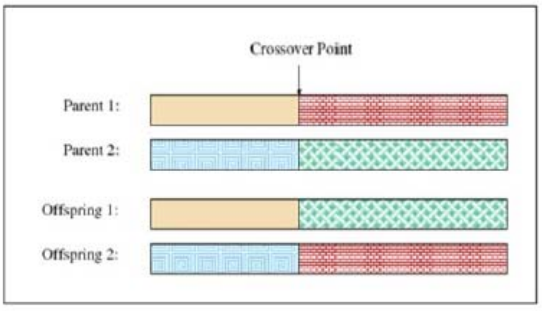

(Parent 1) $X_1 = \{0\ 1\ 0 \mid 1\ 0\ 1\ 1\ 0\ 1\ 1\}$

(Parent 2) $X_2 = \{1\ 0\ 0 \mid 0\ 1\ 1\ 1\ 1\ 0\ 0\}$

(Offspring 1) $X_3 = \{0\ 1\ 0 \mid 0\ 1\ 1\ 1\ 1\ 0\ 0\}$

(Offspring 2) $X_4 = \{1\ 0\ 0 \mid 1\ 0\ 1\ 1\ 0\ 1\ 1\}$

FIGURE 5.4: Crossover

5.4.2.3 Genetic Mutation

The genetic mutation has the task of changes an element of the chromosome (0 becomes 1 and vice versa) at a random position Fig. 5.5. The mutation is essential function for the exploration of the research space. Due to the mutation or the crossover process, however, during the evolutionary process, it is possible that the best individual is lost. So to prevent this loss of valuable information, most genetic algorithms use the strategy of elitism. It is possible that the best individual of the new generation is worse than that of the previous generation, in this case, the latter one will replace a randomly selected individual of the new generation. Through this process there is security that the best individual prevails or can be replaced by a better one.

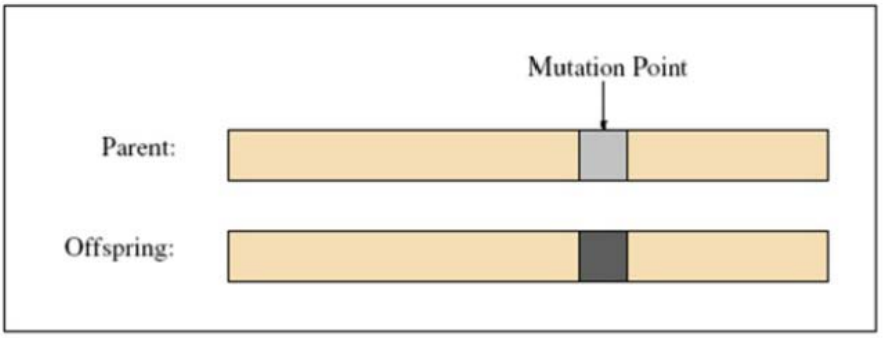

FIGURE 5.5: Genetic mutation

5.4.3 Distributed GA

Over the years, several methods have been studied to accelerate genetic algorithms and the Distributed Evolutionary Algorithm is one of them. In this method the population is divided into islands which evolve in isolation, and the most promising individuals are exchanged between islands. Therefore, "distributes GAs outperform conventional GAs in term of total number of evaluations" [36] [37]. This method is a optimal solution for parallel computing because each island is computed by a single processor or a single solver node. "The main idea is the use of small size of interconnected sub-populations instead of a single large population; these subpopulations evolve independently on each node for a time or period called an epoch. After each epoch a period of migration and information is exchanged between nodes and successive new periods of isolation occur" [38].

5.4.4 Hierarchical GA

The hierarchical genetic algorithm is another method that has the ability to accelerate the GA. A low-fidelity model is used in this method. In fact, the objective function is evaluated by using less accurate tools. This tools can be obtained by reducing the number of grid points or by reducing the complexity of the analysis. These models have the advantage of being computationally less expensive but in contrast they have a lower efficiency. Because of this lower efficiency, each promising individual needs to be reevaluated with a high fidelity model.
Usually the distributed GA is used with the hierarchical GA. In this way in fact the evolution takes place on isolated islands and some of them use the low-fidelity model while others use the high-fidelity model. The individuals that are exchanged and pass from low fidelity islands to high fidelity islands must be reevaluated with the high fidelity model. An example of hierarchical genetic algorithm is shown in Fig. 5.6.

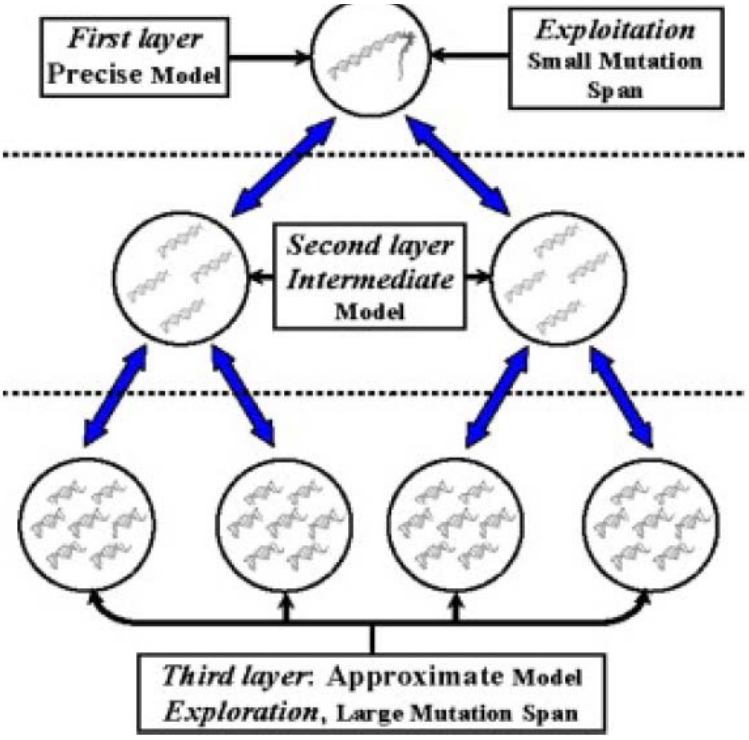

FIGURE 5.6: Hierarchical GA topology.

Chapter 6

Blade Optimisation

6.1 Literature Review

Since the construction, measurements and studies carried out on the NASA Rotor 67 over the years, various works have focused on optimizing the shape of the fan. These jobs had the objective of optimizing performance by changing the geometry of the blade. The following revision in this section aims to highlight which part of the blade has been parameterized and how the various optimization strategies have influenced the results of the optimization process. The main works on the parameterization of the blades with their respective optimization strategies are shown in the Table 6.1 and in the Table 6.2.

First, let's start with direct optimization methods. Among these it is possible to mention the work done by Oyama et al. [39] that has minimized the loss of fan flow through the generation of entropy with a genetic adaptive range algorithm. According to the knowledge of the authors, maximization of isentropic efficiency would be more to the advantage of maximizing the total pressure ratio rather than minimizing flow loss. The total pressure ratio and mass flow were limited, in fact their variation compared to the basic design of respectively 0.5% and 1%, respectively. In their work they analyzed 200 generations with 64 individuals for population, so in total they carried out 12800 CFD analyzes. As a result they got an increase of isentropic efficiency by 1.78% at design point. To achieve this improvement the entropy production was reduced in regions between hub and mid-span, and near tip. The first effect was due to a diminishing of incidence angle, while the second was determined by the maximum camber position that moves

TABLE 6.1: Previous studies on NASA Rotor 67: parameterization

Authors	**Parameterization**	
	Type	Design variables
Oyama *et al.*	Airfoils shape: 4 spanwise sections; camber line + thickness distribution	53
Pierret	Airfoils shape: 4 spanwise sections	35
Lian and Liou	Airfoils shape: 4 spanwise sections (perturbation approach)	32
Lian and Kim	Airfoils shape: 4 spanwise sections (perturbation approach)	32
Okui *et al.*	Airfoils shape: 5 spanwise sect.; camber + spanwise chord distribution Sweep	14
Luo *et al.*	Airfoils shape: 32 Hicks-Henne shape functions (perturbation approach)	238
Hu *et al.*	Blade loading (inverse design strategy) Only airfoil shape can change	-

toward aft. As a consequence of this they have obtained a weaker and shifted aft shock on the blade suction side. Despite the optimization was performed at design point, which could create problems in off-project operation, the optimized geometry still maintained higher isentropic efficiency over the range of operating conditions and the stall margin remained unchanged.

An optimization process that only aims at improving aerodynamics can lead to excellent results as regards performance, but it is very easy to obtain unfavorable structural shapes of the blade. Indeed, small thicknesses in the leading edge region decrease the shock losses, and therefore the overall efficiency is improved. The problem is that these blades are unable to meet mechanical constraints. An optimization process was developed by Pierret [40] in which the aim was the structural aspect of the blade, so as to prove his theory. For the formulation of this optimization, aerostructural objectives and constraints were defined at three operating points: near-stall, near-peak efficiency and near-choking. The optimization also involved a genetic algorithm assisted by RBF interpolation technique. As expected, aerodynamic optimization returned higher values of isentropic efficiency compared to aerostructural efficiency, for the entire speed line.

A different parameterization approach was adopted by Lian and Liou [41] in which

TABLE 6.2: Previous studies on NASA Rotor 67: optimization strategies

	Authors	Optimization Strategy		
		Method	Objectives	CFD runs
No Surrogates	Oyama *et al.*	GA+CFD	-Min. Entropy generation @peak efficiency -Constr.: mass flow + total pressure ratio	12800
Off-line	Lian and Liou	RSM+CFD offline	-Min. Entropy generation + Max. total pressure ratio @peak eff. - Constr.: mass flow	1023
In-line	Lian and Kim	RSM+CFD inline	- Max. total pressure ratio + Min. Blade Weight @peak eff. - Constr.: mass flow + probability of failure	1678
	Okui *et al.*	DE+ANN +CFD	-Max. Isentropic eff.+ throttle margin @peak eff. -Const. mass flow @choke + mass flow @stall	-
	Pierret	RBF+GA+CFD	-Max. Isentropic Eff.+Structural obj @Multipoint (near-stall, near-peak efficiency and choke) →Weights to perform single obj.	-
	Luo *et al.*	Adjoint method	-Min. Entropy generation @ Multipoint (near-stall, near-peak efficiency and choke) -Constr.: mass flow + total pressure ratio	-
	Hu *et al.*	Inverse method	-Max. Isentropic Eff. @Design point - Constr.: mass flow @Choke	-

the optimized rotor blades were obtained by superimposing perturbations on the original geometry. One of the advantages of using this different approach is that baseline geometry is included in the analysis space. In fact, to obtain the original geometry it was sufficient to set the design variables to zero perturbation. The multi-objective optimization was carried out to obtain maximum efficiency, the total pressure ratio was maximized and finally the entropy generation was minimized. As for the mass flow, it was limited within a maximum variation of 0.5%. As a result of this optimization the total pressure ratio increased as much as 1.8% and the entropy production decreased by 6.2%. This has led to an improvement in the isentropic efficiency of 0.7%.

The previously mentioned works take into consideration only the aerodynamic aspects and for this reason the work done by Lian and Kim [42]. In fact, in their optimization process, the structural and aerodynamic performance of the Rotor 67 has been studied. Total pressure ratio and rotor mass were taken as objective functions to optimize, while mass flow rate and probability of failure have been taken as constraints. From this analysis it was discovered that most optimal designs broke the security constraint.

Okui et al. [43] used a 3D parameterization tool of the blade which was more flexible than the previous ones. The parameterization of the blade therefore allowed three main geometric deformations: sweep, variation of the mean camber line and the spanwise distribution of chord. As regards the thickness distribution, it was maintained the same as the original to avoid mechanical issues. To build the optimization process was used a multi-objective evolutionary algorithm with the support of neural networks. Okui has chosen isentropic efficiency and accelerator margin as objective functions to be maximized. The optimization process obtained was then accelerated, respecting the original mass flow, imposing two constraints on the choked and stall mass flow. For these parameters, the off-project performance curve was required and was evaluated by CFD. The whole optimization process was divided into two different optimizations. As a first optimization, only sweep and chord variation were activated. Then a new optimized rotor was obtained with the introduction of the camber design variables. As a second optimization, on the other hand, an optimization of the entire stage was performed keeping the stator fixed and increasing the degrees of freedom of the parameterization of the camber line. As a result of this process it has been seen that as the deformations of the chords and sweeps proceeded, the optimal blade

obtained a forward sweep shape. This form resulted in a 0.3% gain in isentropic efficiency. This obtained form which affected the region of the external span divided the shock wave into a very weak shock on the suction side and a weaker passing shock than before. When, however, the deformation of the camber line was added, it was found that the optimal blade had a form of backward sweeping and this led to an increase in isentropic efficiency of 0.6%. The reason for this better result is to be attributed precisely to the S-shaped camber line. This modification was, in fact, able to compensate for the negative effects of the backward sweep on stability and efficiency.

As for the direct approach optimization method, the last work to mention is that of Luo et al. [44]. A different method from the previous ones was used for this optimization process. The main advantage obtained is that the computational cost has been made independent of the number of design variables. In this case, in fact, the rotor has been described with 288 variables. Two different optimizations were carried out, the first with single-point and the second with multi-point with the aim of minimizing entropy production. As a constraint, the variation of the mass flow rate and the total pressure ratio with respect to the baseline have been kept to a minimum. As for the multipoint optimization took into account three operating conditions: near choke, near peak efficiency and near stall. Looking at the results, in the single-point optimization the isentropic efficiency has increased by 1.10%, but this at the expense of a significant reduction in total pressure ratio for all the operating conditions between stall and peak efficiency. In the multipoint optimization, instead, the isentropic efficiency has increased in all three operating conditions, with increments of about 1.24% near choke, 0.84 near peak efficiency, 0.54% near stall. The difference from the first optimization is that the total pressure ratio is almost unchanged compared to the baseline all over the range.

Talking now about the reverse optimization method, it is possible to list three different jobs related to NASA Rotor 67. The first two, i.e., the one of Watanabe and Zangeneh (2003) [45] and Tiow and Zangeneh (2002) [46], are based on the study of the inverse method itself and its ability to reconstruct the geometry given a target loading. For these jobs two different pressure loading distributions, derived from the original loading distribution of Rotor 67, were tested in order to analyze the variation of the isentropic efficiency. As a result of the studies carried out it was seen that the second distribution performed better with an improvement of about 0.6%. Furthermore, the stall margin was increased by 3%.

In the third work, Hu et al. [47] optimized the blade loading pressure distribution.

To do this optimization, the loading pressure has been parameterized for various span sections through the use of B-spline control points. Only the deformation of the 2D blade geometry was studied, therefore only the shape of the section changed while the changes in inclination and sweep were not taken into account. It was also chosen to perform the optimization only in a specific operating point. The main problem that was encountered was to control the air flow rate in order to keep its value as close as possible to the baseline. Two methods have been proposed in Hu's studies. As a first observation, it has been noted that the modification of the operating point, keeping the pressure load constant, could lead to a variation of the characteristic curve. This variation, in fact, could modify the air flow. Second, it was noted that the choked air flow was influenced by the peak position of the pressure load. As a result of this study the isentropic efficiency of NASA Rotor 67 was increased by 1.26% at design point, while the choke flow rate was reduced by 0.8%. It has been seen that most of the improvement comes from 25% to 100% of span.

6.2 Lean And Sweep Deformations

The shock wave that occurs in the palar canal of a transonic rotor is responsible for the losses related with both the shock itself and for the shock-boundary layer interaction. It is also responsible for the stability of the compressor in terms of stall margin. To counteract these losses, a modification of the stacking line could positively influence the shape of the shock wave, improving the performance of the compressor. The studies and simulations conducted so far have shown that there are three main changes that can be made: blade airfoils deformation as it is possible to see in [48] and [39], sweep and lean.
As for the sweep and lean, these involve 3D deformations of the stacking line of the blade. In other words, these variations are defined as profile translation, projected on the compliant plane, along the direction of the rotation axis (sweep) or tangential direction (lean) as it is possible to see from the Fig. 6.2. Both sweep and lean changes can be specified with adjectives forward and backward. With reference to lean, forward or backward refer to concordance or discordance to the displacement of the stacking line with the direction of rotation of the rotor. As for the forward or backward sweep, this depends on the direction of the displacement, which could point in the downstream (backward sweep) or upstream (forward sweep) direction.

Focusing now on the backward sweep, this was first studied by Hah and Wennerstrom [49]. They have shown a significant improvement in peak efficiency but this at the expense of a reduction in the stall margin. This penalty was caused, as reported by Wadia et al. [50], from the local increase in load in the tip section. This effect provoked a strong bow shock, as well as a more intense migration of fluid particles on the boundary layer of the suction side. Hah et al. [51] has instead demonstrated the advantages of a forward oriented rotor. In fact, a greater margin stall and higher peak efficiency are obtained with respect to the original unswept rotor. Denton and Xu subsequently confirmed by obtaining similar results with their CFD [52] analyzes.

It is now known that the blade sweep is an effective technique for distributing the radial load [53], but, in addition to this effect, the sweep affects the position of the shock, which tends to take the shape of the sweep. In addition to this the so-called endwall effect has been observed, this is the shock approaching at right angles as demonstrated by Hah et al. [51]. Therefore, due to the overlap of the sweep and the "endwall effect", the position of the shock is shifted downstream in the case of the forward sweep while upstream in the backward sweep, as shown in Fig. 6.1. As has been observed, usually, a more backward position of the shock translates into better stability. This is the justification for the improvement in the stall margin observed with the rotors oriented forward.

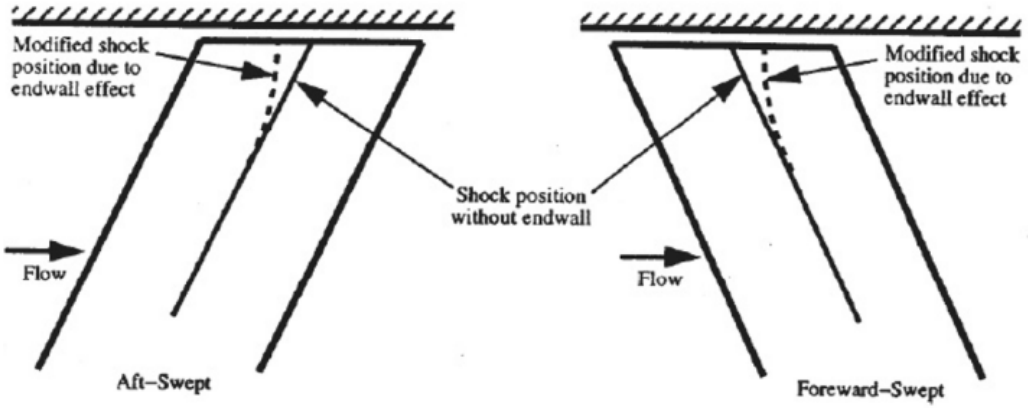

FIGURE 6.1: "Enwall effect" on shock structure near casing [14]

Many studies carried out on lean have revealed that its use can produce favorable effects due to the change in the structure of 3D shocks as can be seen in the work of Bergner et al. [54]. In fact, forward lean, i.e. towards the direction of rotation, has shown a positive influence on the overall efficiency of the rotor as can be seen

in the works of Ahn and Kim [55] and Benini [56]. Finally, an important study with excellent results on the aerodynamics of swept and leaned transonic rotors was developed by Biollo and Benini [57].

6.3 Parameterization

The change in the shape of the NASA Rotor 67 blade was achieved by superimposing a displacement field on the points of the baseline geometry. This strategy made it possible to start the optimization process from the original blade geometry. In order not to go into lengthy mathematical explanations, the displacement field is described by a B-spline surface which returns the displacements in the three directions, i.e. dx, dy, dz, for each point of the baseline geometry. In this way it was possible to obtain an entire optimization of the blade geometry.

6.3.1 B-Spline Surfaces

A B-spline surface is definied as the extension of the B-spline concept to 3D space. To better understand the concept of B-spline surface, the reader can refer the work of Mortenson [58]. In this work, in fact, it is possible to see a detailed explanation of B-spline surfaces and their numeric implementation. The B-spline surface equation is defined as the tensor product:

$$p(u,w) = \sum_{i=0}^{m} \sum_{j=0}^{n} P_{i,j} B_{i,K}(u) N_{j,L}(w) \tag{6.1}$$

in which the curve $p(u,w)$ is defined by the polyhedron control points $P_{i,j}$ and the basis functions polynomials $B_{i,K}(u)$ and $N_{j,L}(w)$. These depends on the specific i-th or j-th control point, but their degrees K and L are independent on the number of control points and this is very important because the number of control points can be very high.

6.3.2 Parameterization Framework

In the work done in this thesis, the parameterization of the blade was obtained by superimposing two main deformations: the deformation of the 3D stacking line and the deformation of the 2D profile. Each of these deformations has been treated independently with B-spline curves so as not to have interactions between the changes. Subsequently these two different deformations are joined together so as to form the final displacement field of the surface of the B-spline. To do this parameterization, six equally spaced sections of the blade have been selected as control sections. Each of these sections has been derived by intersecting the baseline blade with the streamline surface.

6.3.3 Sweep And Lean Deformations

By means of a flat, 2D translation of the control sections, a complete modification of the entire 3D shape of the stacking line is obtained, as can be seen in Fig. 6.2. Modifying only the sweep would only obtain a variation of the geometry on the southern plane, while modifying only the lean would modify the stacking line only on the tangential plane. Generally, therefore, to obtain a complete modification of the blades, these two modifications are combined. In fact, this procedure has been adopted in this work. The parameterization used is the same used and validated by Venturelli [12] in his PhD. In fact, a more detailed explanation can be read in its elaborate. The parameterization created is therefore based on two B-spline curves which were obtained by interpolating the displacement values in the six control sections. These two curves are sufficient to describe the displacement field along the span of the blade. The defined displacement field involves 12 control points, 6 for the lean and 6 for the sweep. Another type of parameterization had been studied by the author but due to the limited time available, the model already validated was chosen, although potentially less accurate. Therefore in the model used, in order to obtain an effective deformation of the stacking line, it was decided to use the control points to define the shapes. In this way, each of the forms imposes relationships between control points so that they are no longer independent of each other. As shown in Fig. 6.3, the sweep and lean shapes remain independent and can influence the blade in two different ways: they act locally near the tip and globally in the rest of the blade. Overall, 9 shapes have been defined and adopted as design variables in the optimization process used.

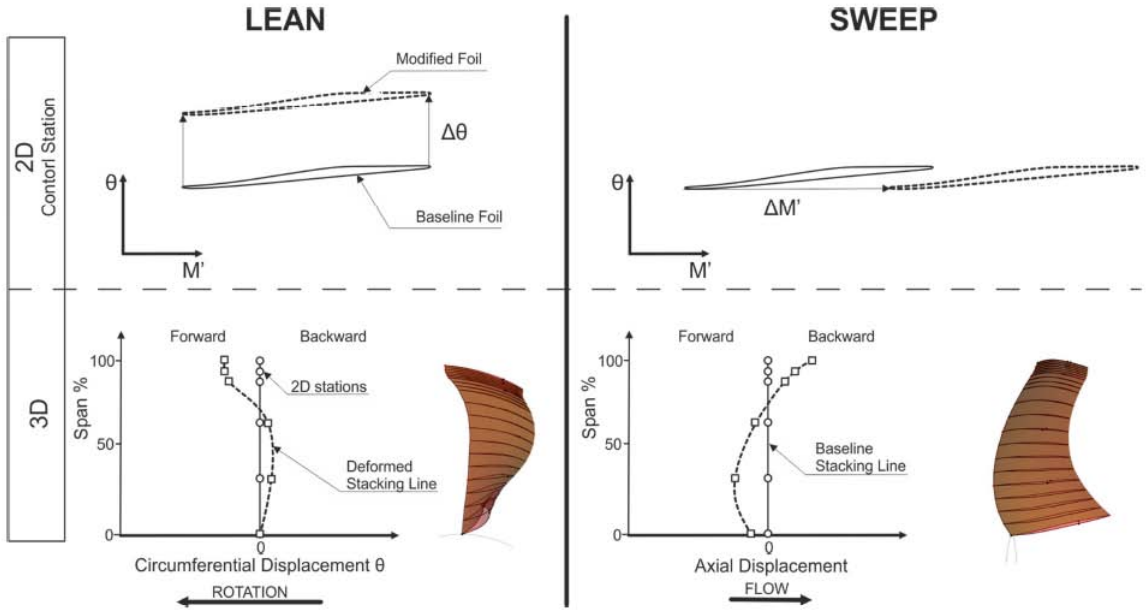

FIGURE 6.2: Lean and sweep definition

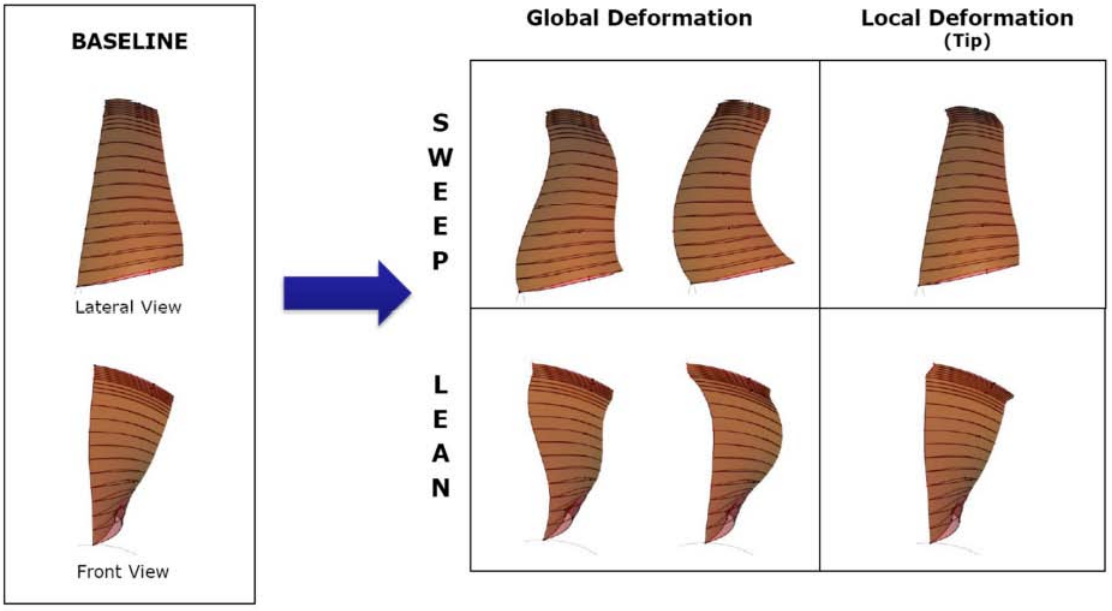

FIGURE 6.3: Blade parameterization: global and local deformations of sweep and lean

6.3.4 Foil Deformations

The profile of each of the control sections was parameterized through the use of different control points. Also in this case therefore a displacement field was created and the 2D foils were deformed using the shape approach. In fact, this approach,

as explained before, allows to reduce the number of design variables while guaranteeing promising deformations within the research space. This choice was made because a compromise was sought between computational resources and the width of the research space. In fact, the more variables are taken into consideration, the more the field of research expands but on the other hand the computational cost becomes impossible to sustain. Fig. 6.4 shows how the hub section can be changed. It is possible to see that by applying high or low values of its two control points of the shape the degree of modification totally changes. Such high displacements are only to highlight the ability of the parameterization approach used and are not representative of the deformations adopted in the optimization process. In fact, changing the shape of the blade too much leads to too high a time and calculation power. Overall, therefore, 2 shapes x 6 control sections return 12 design variables, these added to 9 of the stacking line parameterization bring the total to 21 design variables. This number of variables is an excellent compromise between the degree of deformation and the computational cost of the optimization process.

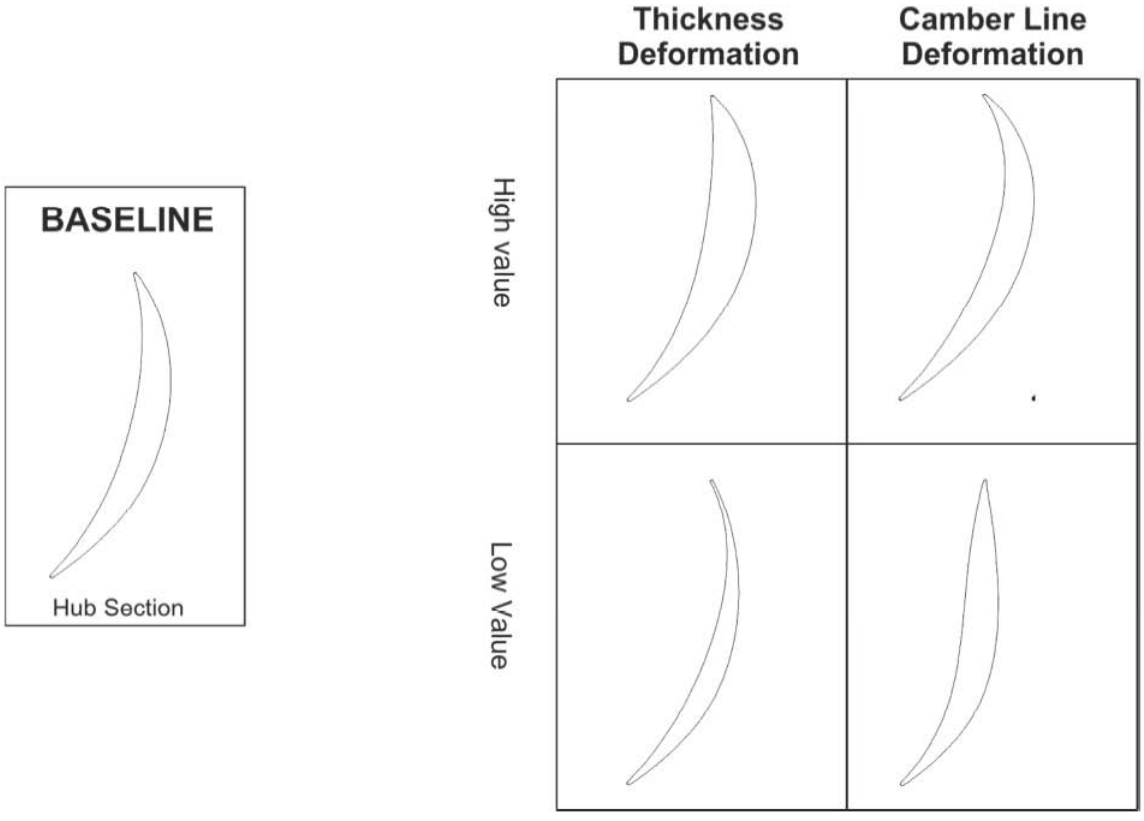

FIGURE 6.4: 2D foils deformations

6.3.5 Spline Model Of The Entire Blade

The following is a brief mathematical description of how the surface of the B-spline is presented. It is possible to see how the two deformation categories are taken into consideration, namely the staking line and the 2D foil. The modified geometry, therefore, is the result of the baseline geometry disturbed by the displacement field created:

$$p_{mod}(u, w) = p_{base}(u, w) + p_{displ}(u, w) \tag{6.2}$$

where the u and w are the parameters of the B-spline surface. The first parameter is defined around the foil, in fact it takes the value 0 on the trailing edge, 0.5 on the leading edge and finally 1 when it returns on the trailing edge. The second parameter is instead defined along the span of the blade, in fact it extends from the hub to the shroud. It takes the value of 0 for the hub and 1 for the shroud. As regards $p_{base}(u, w)$, it represents the high fidelity approximation of the baseline blade, which is defined by 21 spanwise sections. In fact, the number of control points are of the same order of magnitude of the points.
While $p_{displ}(u, w)$ is defined as:

$$p_{displ}(u, w) = p_{lean}(w) + p_{sweep}(w) + p_{foil}(u, w) \tag{6.3}$$

in which both the sweep and lean displacement fields are function of the only spanwise location. The foil displacement, instead, depends on the foil taken into consideration.

6.4 Formulation Of The Optimization Problem

The aim of the multi-objective optimization problem developed in this thesis is to maximize the two-objective function keeping constant a specific design mass flow rate:

$$F(P) = (f_1, f_2) = (-\eta_{pol}, -\pi_c) \tag{6.4}$$

where P is the vector of the optimization parameters or decision variables of the design (i.e., the control parameter of shapes describing the displacement field), η_{pol} is the polytropic efficiency and π_c is the compression ratio of the rotor. As it is possible to see from the formula, a minus sign has been placed in front of the objective functions to be maximized. This was done in such a way as to obtain a correct Pareto Front. The constraints complete the problem formulation. A penalty function has also been included to manage any violations of the restrictions by the chocking mass flow, for which a variation of 0.5% with respect to the baseline was acceptable. The term Q, in fact, depends linearly on the level of violation of the constraints:

$$Q = (Q_1, Q_2) = (r_1, r_2) \cdot G \tag{6.5}$$

$$G = max\{\frac{\mid \dot{m}_{choke-bl} - \dot{m}_{choke-new} \mid}{\dot{m}_{choke-bl}} - 0.005, 0\} \tag{6.6}$$

For this optimization process no geometric constraints were imposed. The range of the decision variables, in fact, was set in such a way that unfeasible geometries were avoided. It should be noted that the range was deliberately set very wide with the aim at reaching the most disparate configurations. For a broader description, the reader is brought back to read the paper by Giovanni Venurelli [12]

Chapter 7

S-duct and NASA Rotor 67 Optimized Results

This chapter are reported the results of the whole work done by the author during his stay at the University of Cranfield. The built-in optimization process, despite the many problems encountered along the way, gave good results. Unfortunately, due to the complexity of the work and the optimization, it was not possible to obtain a large number of results. In fact, since the system being analysed is very complex, this entailed a high computational cost and therefore a high expenditure of time. However, the results obtained are encouraging and demonstrate the correctness of the analysis carried out and the decisions taken. It was decided to report all the results obtained through the use of a graph showing the Pareto Front. Subsequently, the most relevant results of the entire optimization process were analysed individually in detail. The cases studied are the following:

- entire system with Rotor 67 optimized (best η_{pol})
- entire system with Rotor 67 optimized (best π_c)
- entire system with Rotor 67 optimized (trade-off)

7.1 Entire System

This section describes the entire system built and the parameters used for it. The entire simulation was carried out on Ansys CFX, by exploiting the Delta cluster of Cranfield University. In this case, the simulation was carried out by using multiple nodes in parallel. This is due to the high computational cost, that the simulation required. Indeed, the parameters of the simulation are:

- No. of Nodes 38e+6
- No. of Domains 4
- no. of Iteration 1500
- No. of CPU 128 cores
- No. of RAM 1024 Gb
- Computational cost 33 hrs

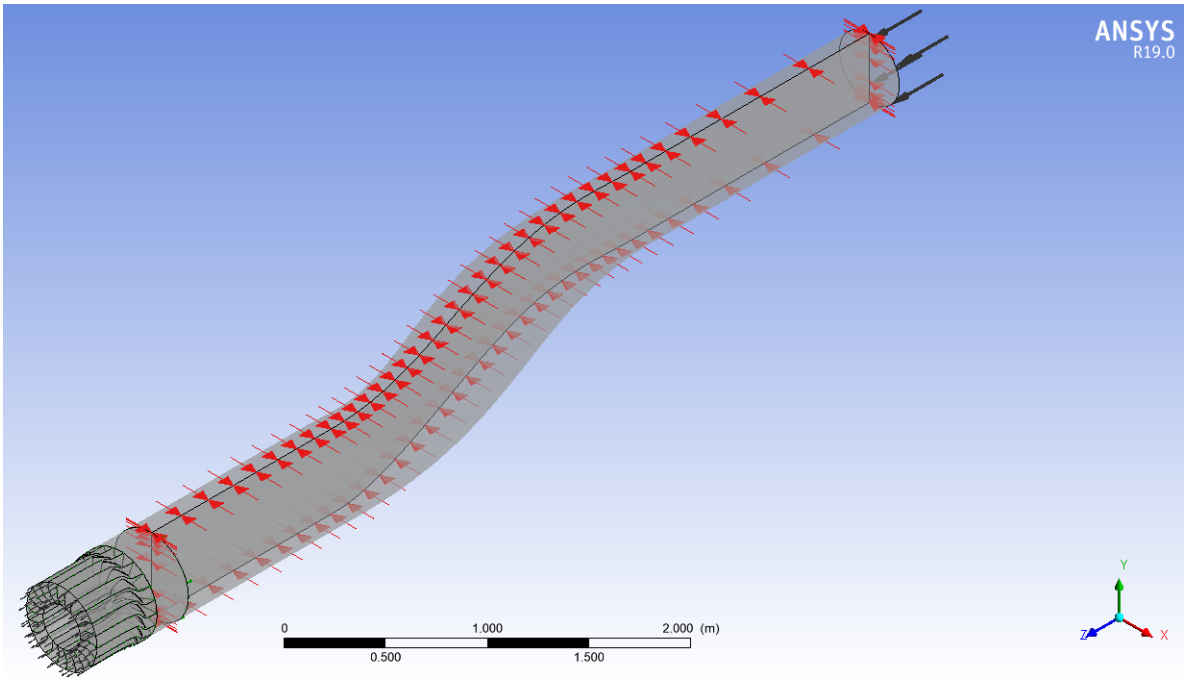

FIGURE 7.1: View of the entire system

As it is possible to see in Fig. 7.1 and Fig. 7.2, the system domain is divided into three different bodies: each of these has been connected via an interface in CFX. The three domains are in order: S-duct, ogive, fan.

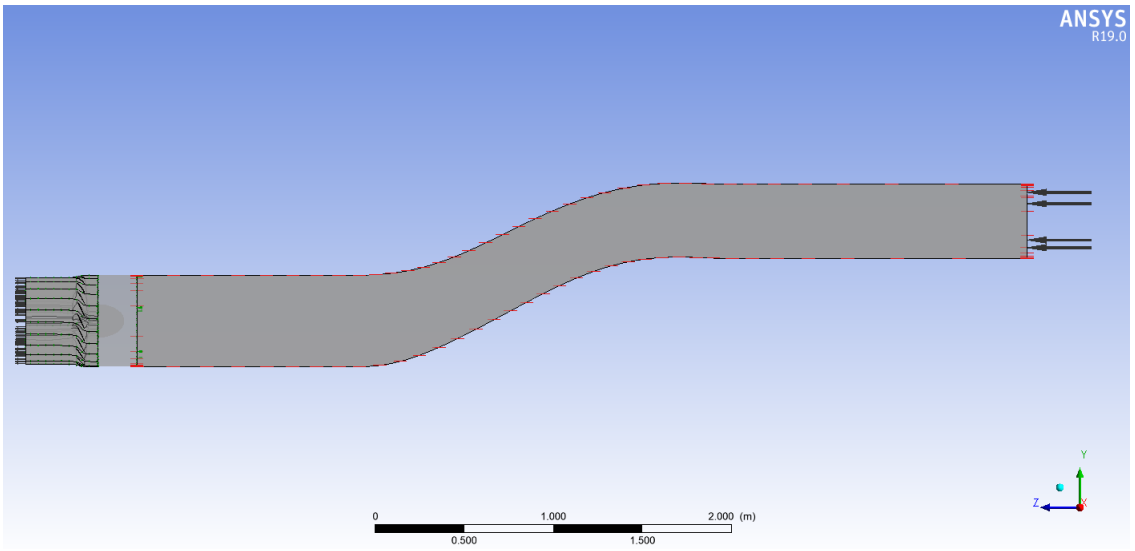

FIGURE 7.2: View of the entire system

7.1.1 CFX-Pre Set-up

In the next Table 7.1 all of the relevant parameters are reported. As conditions surrounding the entire system, the previous conditions used for all the other analyses carried out have been adopted in order to have a direct comparison with the results. The only difference from the work done by Tridente [24] is that the fan rotation speed has been set at 100%. The of the author decided to compare the performance of the optimized rotor with the performance derived from the analyses carried out by the authors mentioned above. Among these, in fact, the work done by Venturelli [12] in which the parameterization of the blade is the same is of particular attention.

In this analysis the convergence was critical throughout all the calculation. To solve this problem a user function was implemented with the purpose of adapting the maximum timescale, which indeed is of utmost importance for calculation stability. At the beginning a value of 1e-7 [s] was set, then it was increased up to 1e-4 [s], for then return to lower values around 1e-5 [s] before calculation was stopped. The convergence was established when the RMS maximum residue were lower than 1e-5 and the variables of interest described in the next paragraph had an asymptotic behaviour.

Table 7.1: Set-up of the parameters in CFX-Pre

	Ansys CFX Solver set-up	
Analysis Type	Steady State	
Domain	Domain Type	Fluid Domain
	Fluid and Particles Definition	Air Ideal Gas
	Reference Pressure	0 [atm]
	Domain Motion Option	Rotating
	Domain Motion Angular Velocity	-16043 [$revmin^{-}1$]
	Heat Transfer	Total Energy
	Turbulence Option	SST
	Wall Function	Automatic
	Wall Heat Transfer Model	High Speed
Boundary Condition	Hub	No Slip Wall Smooth Wall Adiabatic Rotating Frame
	Shroud	No Slip Wall C-R Wall Smooth Wall Adiabatic Rotating Frame
	Inlet	Subsonic Stat. Frame P_0 106390 [Pa] Normal to BC Stat. Frame T_0 288.2 [K] Frame Stationary
	Outlet	Subsonic MFR or Pressure Variable
Solver Control	Advection Scheme	High Resolution
	Turbulence Numerics	High Resolution
	No. Iteration	1500
	Timescale Control	Timestep Function
	Convergence Criteria	MAX 1e-5

7.1.2 S-duct Optimized

The S-duct, chosen to carry out the optimization, was obtained from the analyses carried out by Dal Magro in his course of studies. For a more accurate description we can refer to his work [13]. The decision to use this S-duct was made by the author as it was the one that gave the best results in the analysis of the complete system carried out by Tridente [24]. Unfortunately, it was not possible to use the ducts studied by Meneghin [15] as it had not yet reached an acceptable solution, when the optimization process was started. In fact, the time required for optimization is very long, so it was not possible to wait for the completion of Meneghin's work. The most important difference between the ducts under study and the duct considered for this optimization is that the latter is longer. In fact, it has a longer section after the S-curve which in the ducts studied by Meneghin has been removed. The reason for the removal of the final section of the duct is due to the fact that it was too long and was therefore unusable on a practical level in a real case. In addition to this fact, most of the duct taken into consideration entails a worsening of the outlet flow since the turbulence has time to develop thus creating many more leaks. In any case, the study carried out in this thesis is focused on optimizing the performance of NASA Rotor 67 therefore the analysis with the best duct obtained by Dal Magro has been accepted. In Fig. 7.3 it is possible to see the s-duct taken into consideration.

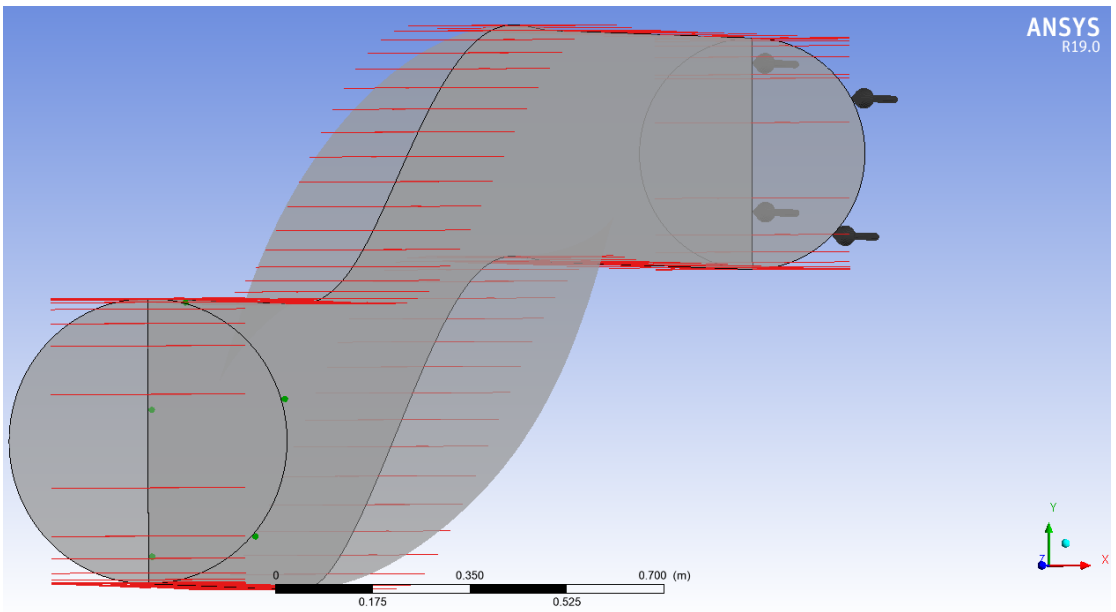

FIGURE 7.3: View of the S-duct

The Fig. 7.4, instead, shows the mesh developed for this s-duct. For a correct description of the phenomena occurring inside the duct and to obtain the most detailed output flow possible, it was decided to use a very fine mesh of 3320000 elements.

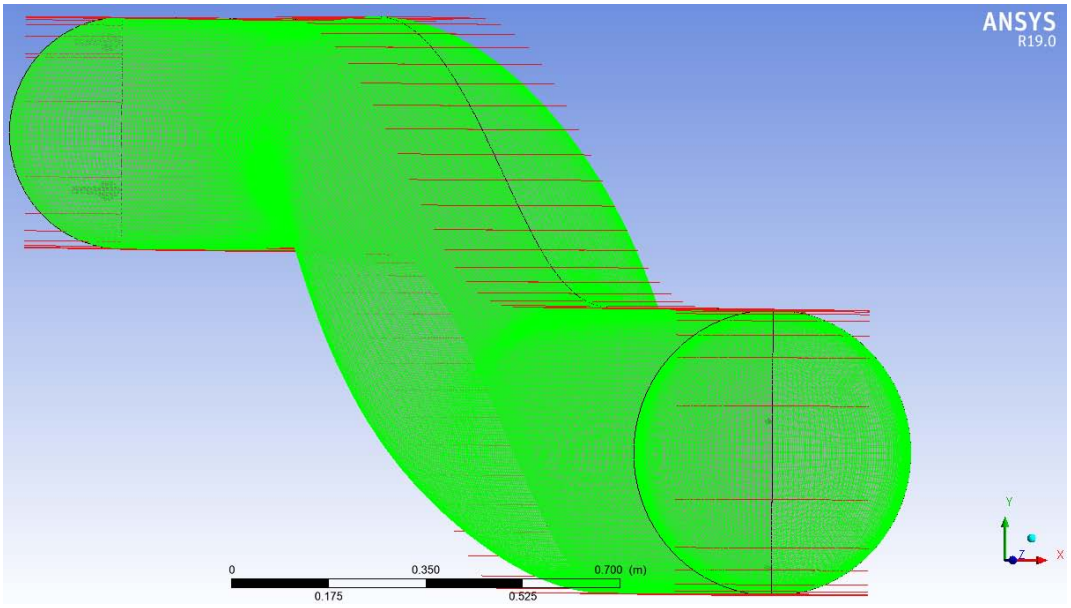

FIGURE 7.4: View of the S-duct mesh

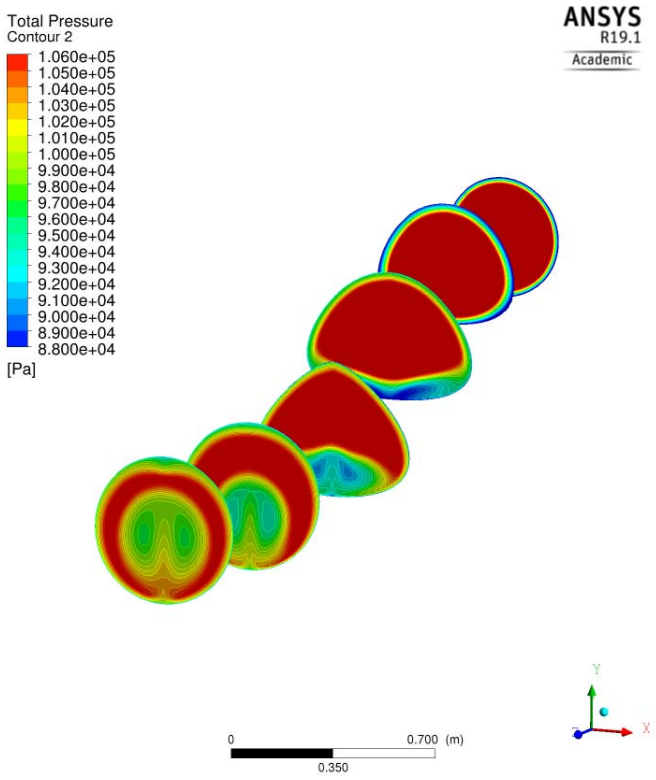

FIGURE 7.5: Contour of the S-duct

Fig. 7.5 shows the trend of total pressure along the duct. The last section shown in the figure corresponds to AIP. Fig. 7.6, on the other hand, shows the S-duct studied by Meneghin in order to see the difference compared to the conduit taken into consideration for the analysis carried out.

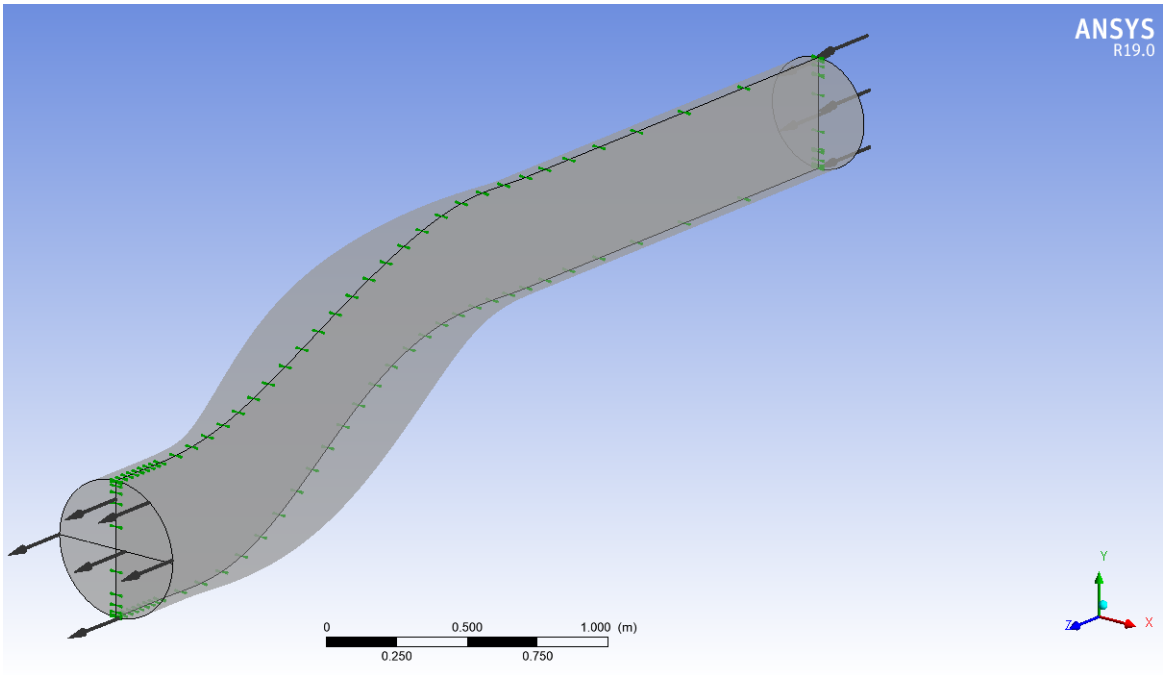

FIGURE 7.6: View of the S-duct studied by Meneghin [15]

7.1.3 NASA Rotor 67 Optimized

This section shows the entire NASA Rotor 67 used for this optimization. During the calculation process the geometry of the blades changed from time to time, while the rest remained unchanged. Even the mesh remained the same number of elements in order to have the same degree of precision. Then at each calculation cycle the geometry of the blade was modified and then the entire rotor was rebuilt and the mesh was rebuilt again. In the Fig. 7.7 it is possible to see the rotor used for the analysis. The inlet was kept short so as not to develop turbulence in the flow and so that the ogive was placed near the blades as it happens in reality. On the other hand, the outlet, was kept long so as to see the behaviour of the outgoing flow without it being directly disturbed by the blades.

The Fig. 7.86 shows the mesh used for the rotor. As for the size of the latter, it was very difficult to find a solution. Initially the single palar canal previously optimized by Venturelli [12] was studied with a very fine mesh. This decision

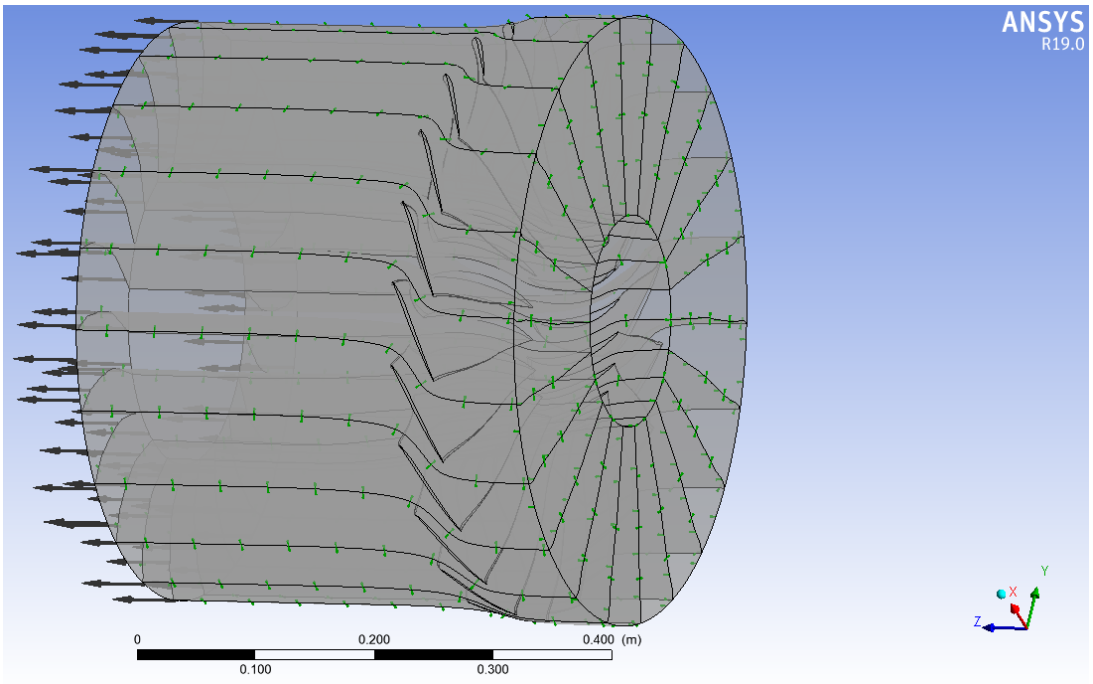

FIGURE 7.7: View of the entire Rotor 67

was made because it was necessary, for the correctness of the optimization, that the flow within the channel was described in the best possible way taking into account also the computational cost. In fact, a too fine mesh entails an excellent description of the flow but, on the other hand, returns too high a computational cost. A too coarse mesh instead guarantees a very low computational cost but at the expense of the accuracy in the description of the flow. The main problem is that the rotor is transonic and therefore a perfect description of the shock waves is necessary for the optimization process. In fact, an inaccurate analysis compromises the entire optimization. Venturelli has found a compromise solution by using a single-passage mesh of 2.3 mln elements. However, this mesh is too heavy if used for the entire rotor as the number of elements must be multiplied by the number of palar channels which are 22. There is a mesh of 50.6 mln elements of the rotor only which is unsustainable for the calculation resources available. Because of this fact it was decided by the author to lower the size of the mesh being aware that the description of the shock waves is affected. To find the right compromise, several tests were carried out in order to understand which solution was the best. Initially the baseline geometry of the rotor was analysed with a very coarse mesh. The result of this analysis confirmed what supposed. The main performance parameters of the rotor were described with a small difference compared

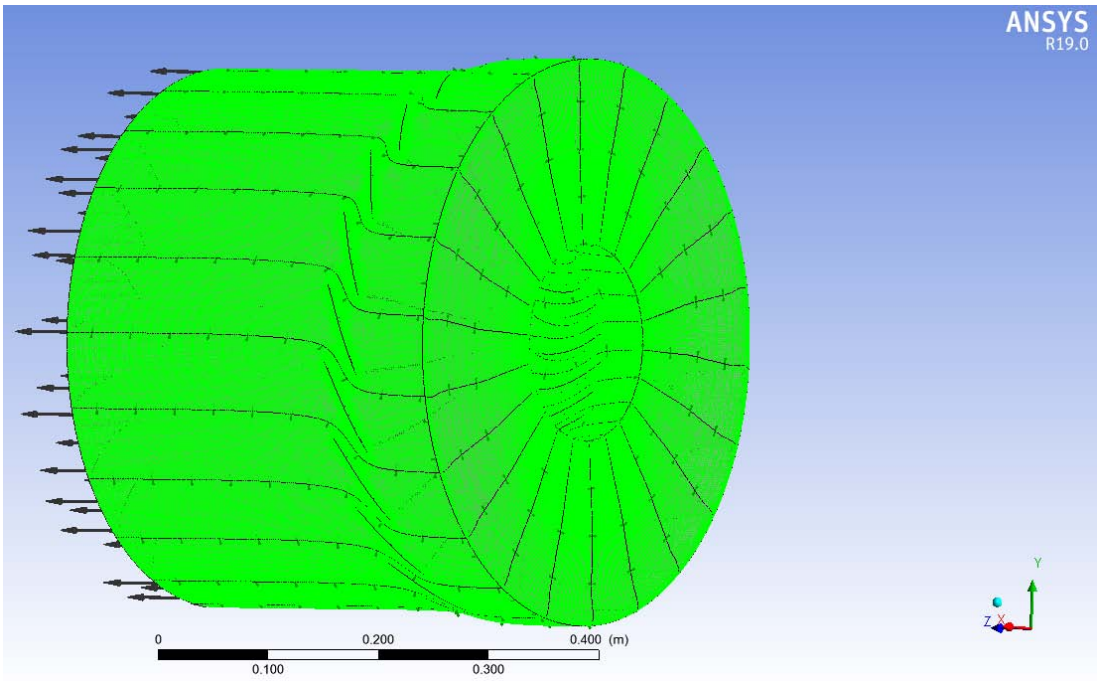

FIGURE 7.8: View of the entire Rotor 67 mesh

to the correct parameters. While the rest of the parameters, including the description of the shock waves, had huge errors. However, since the compression ratio and the polytropic efficiency are of interest, and since these two values differed slightly from the real ones, an optimization process has been tried with the use of a very coarse mesh. The aim was to maximize the two goal functions with a limited computation time required. Once the optimized geometry was obtained, then will be studied through a very fine mesh in order to validate the results and the process. This did not happen because, although the parameters were optimized with the use of the coarse mesh, once the geometry with the very fine mesh was studied, this returned the real performance which was significantly worse than the baseline performance. In conclusion, a coarse mesh takes the blade optimization process out of the way because the shock waves and therefore the losses connected to them are not accurately described.

Given this result, it was decided to use the finest mesh possible based on the maximum calculation performance available. The number of elements of the mesh used for the optimization process is therefore 1.6 mln for each palmar canal. Consequently, the mesh size of the entire rotor is 35.2 mln elements. A mesh of so many elements, considering also the addition of the elements of the s-duct and the ogive, entailed a very high computational cost. In fact, a single calculation loop took 33 hours. This high calculation time is the reason for the few results obtained.

7.2 Results of the Optimization Process

The developed optimization process was cycled in the time available. At the end of the calculation cycles, all the results obtained were collected and the graph shown in the Fig. 7.9 was created. From this graph it is possible to see the Pareto Front. Unfortunately, due to the limited time available, the amount of results is limited, but it is sufficient to have an idea of the optimization process. In addition to the insufficient time, the real bottleneck of this work is the complexity of the system taken into consideration and the need for a very accurate analysis without which the results that would be obtained would be distorted. As you can see from the graph, the two objective functions have been optimized in an excellent way. It is interesting to note how they are decoupled so in an attempt to improve only one of the two functions the other, most of the time, gets worse. In order to obtain an excellent final result, the trade-off solution between the two functions was taken into consideration. In addition to this, the solutions with maximum value of the respective objective functions were specifically analysed.

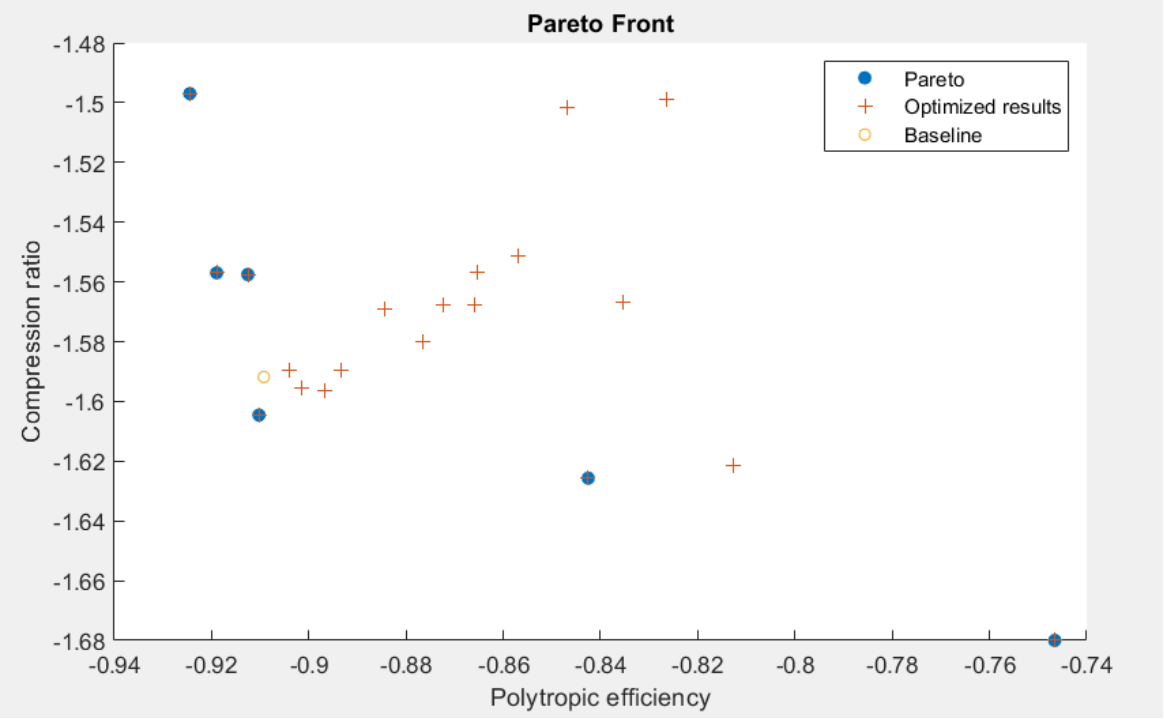

FIGURE 7.9: Pareto Front

The Table 7.2 details the solutions analyzed with the respective values of the target functions.

TABLE 7.2: Performance of the optimized geometries

Individual	π_c	$\Delta\pi_c$	η_{pol}	$\Delta\eta_{pol}$
Baseline	1.591817	-	0.909263	-
Best η_{pol}	1.496984	-0.094833	0.924487	+0.015224
Best π_c	1.679987	+0.08817	0.746584	-0.162679
Trade-off	1.604587	+0.01277	0.910254	+0.000991

From the values shown, it is possible to notice how the fan performance has deteriorated compared to the baseline. This deterioration is due to the flow out of the s-duct which leads to leaks and malfunctions in the fan. In particular, since there is no uniformity in the flow at the fan inlet, this has different behaviours based on the region in which you are located. This change in flow conditions causes non-ideal operation and therefore a drop in performance. Despite the general decrease in performance, it is of interest to note the maxima of the two respective objective functions. As for the compression ratio, it is possible to see a significant increase compared to the baseline, in fact, it increased by 0.08817. On the other hand, however, the blade that returned this result shows a considerable collapse of the polytropic efficiency which decreased by -0.162679. As for the polytropic efficiency, it is possible to see an increase of $+0.015224$ with, however, a respective decrease in the compression ratio of -0.094833.

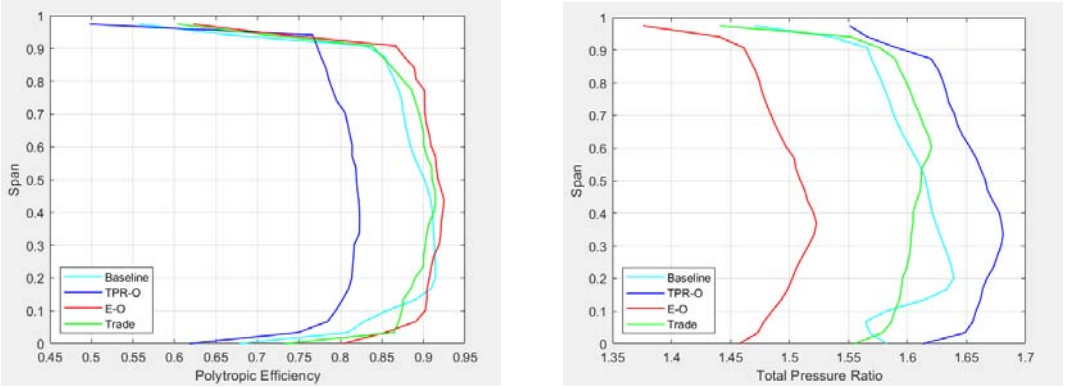

(a) (b)

FIGURE 7.10: Spanwise distribution of polytropic efficiency and total pressure ratio of the baseline and optimized configurations

In the Fig. 7.11(a) it is possible to see the comparison of the three different optimized blades. The blue blade is the one that corresponds to the best compression ratio obtained, the red blade corresponds to the best polytropic efficiency and finally the green blade is the one that presents a compromise between the two parameters. In the Fig. 7.11, on the other hand, it is possible to see in detail the

variation in shape of the profiles with different spans. A detailed description of the operation of the three blades will be given below.

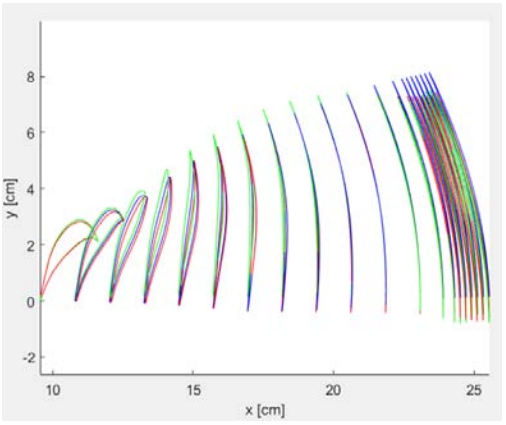

(a) Blades

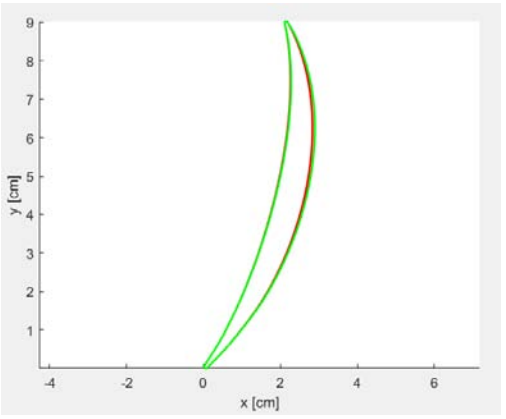

(b) Hub

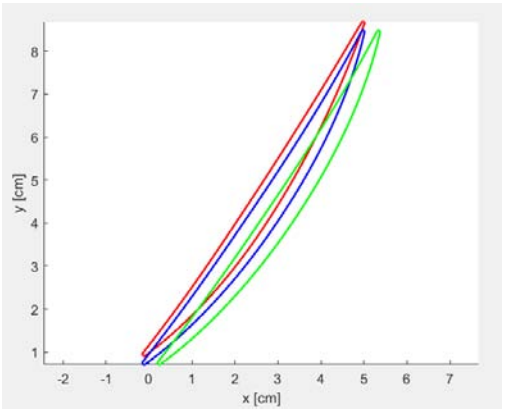

(c) 25% span

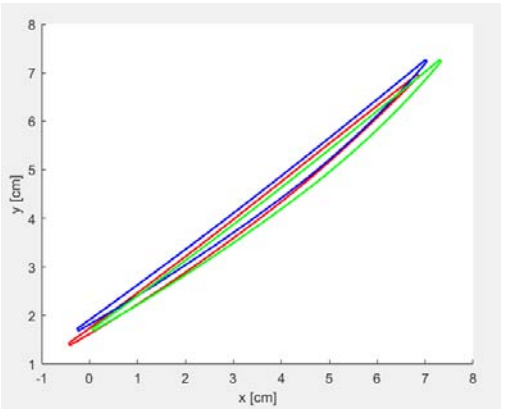

(d) 50% span

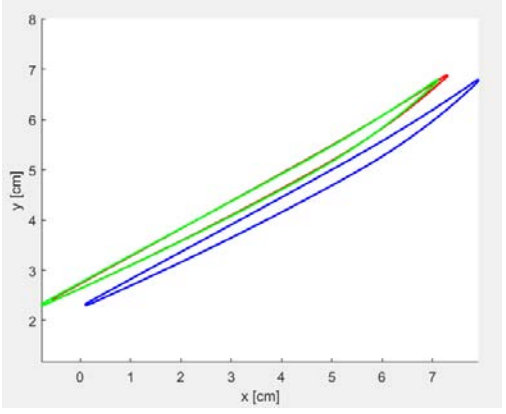

(e) 75% span

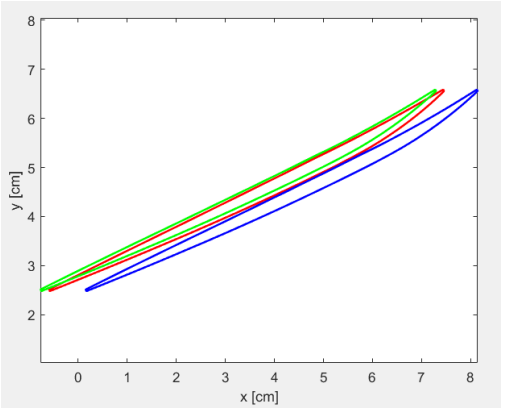

(f) Tip

FIGURE 7.11: Comparison of the three optimized profiles: blue (best π_c), red (best η_{pol}), green (Trade-off)

7.3 Best η_{pol}

Analysing in detail the blade that returns a higher value of polytropic efficiency we can see substantial differences compared to the baseline. The change in geometry mainly affected the stacking line while it only slightly changed the shape of the profiles. As you can see the lean gave an S-shaped profile to the leading edge of the blade. Starting from the hub, in fact, the inclination is first forward up to half the span and then backwards. Furthermore, near the tip it is possible to see a strong inclination in the direction of rotation. As for the sweep, the blade has a forward sweep from the half-span hub and then, instead, has a backward sweep to the tip. Finally, a higher camber and a slightly lower thickness compared to the original design was observed in the hub section. All these deformations have decreased the flow losses and have reduced the intensity of the shock waves, which is why polytropic efficiency has increased at the expense of the compression ratio. In fact, this blade is less loaded than the base line therefore a lower compression ratio is obtained.

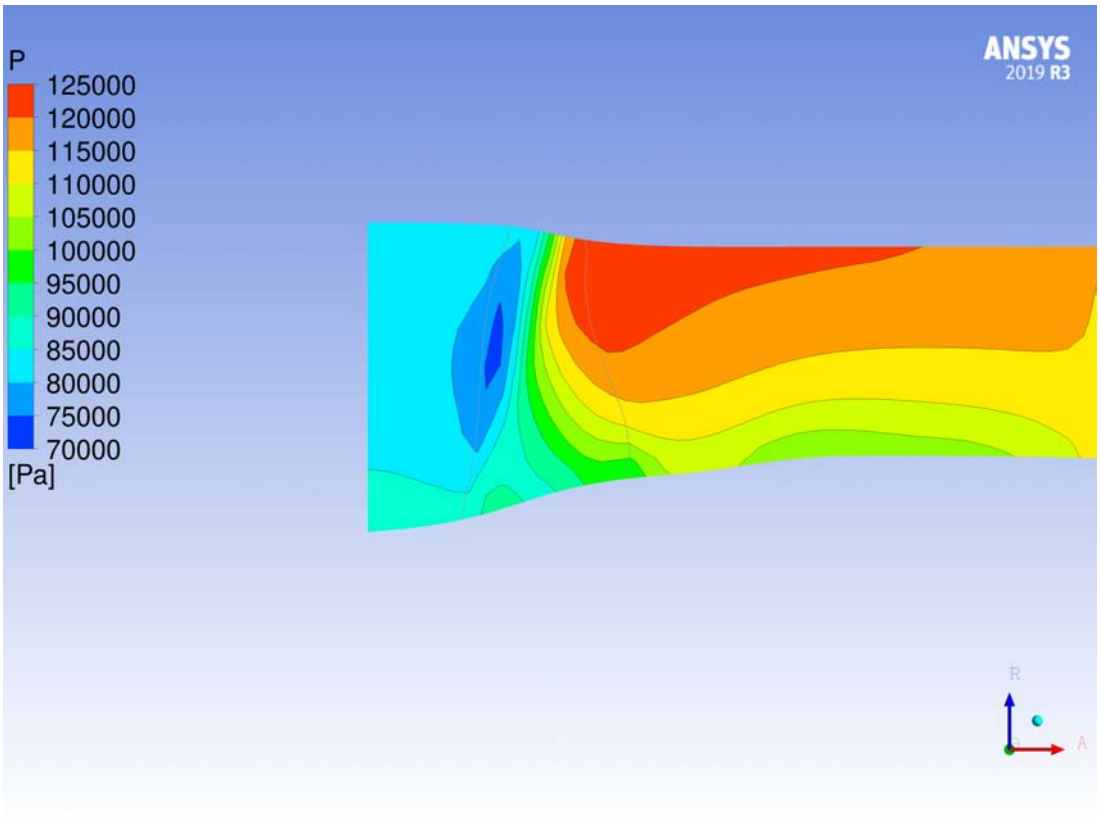

FIGURE 7.12: Static Pressure along the span

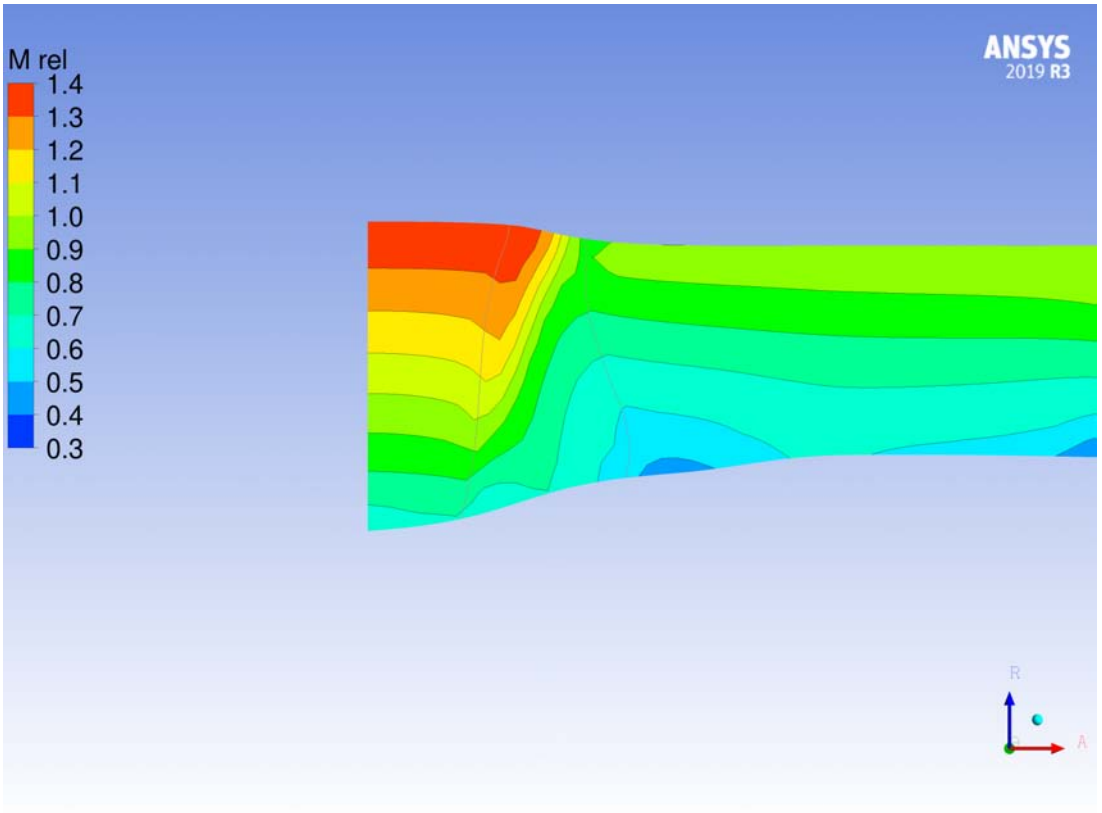

FIGURE 7.13: Relative Mach along the span

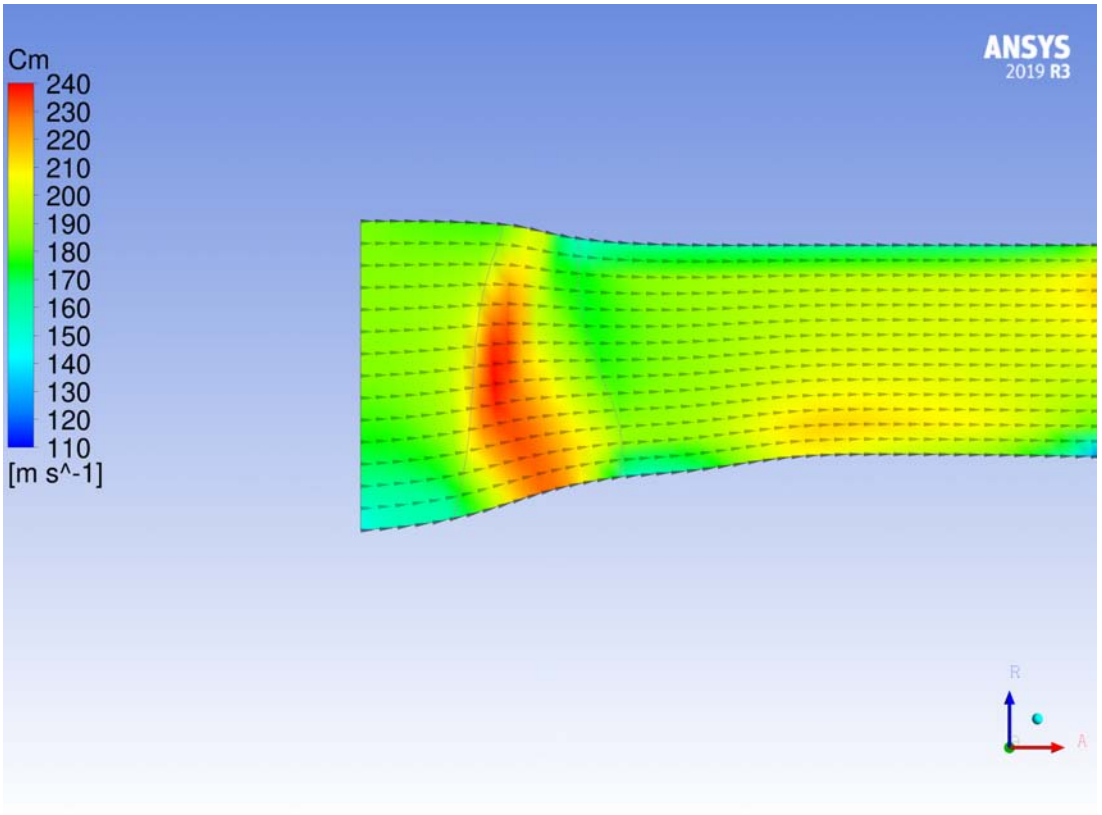

FIGURE 7.14: Cm along the span

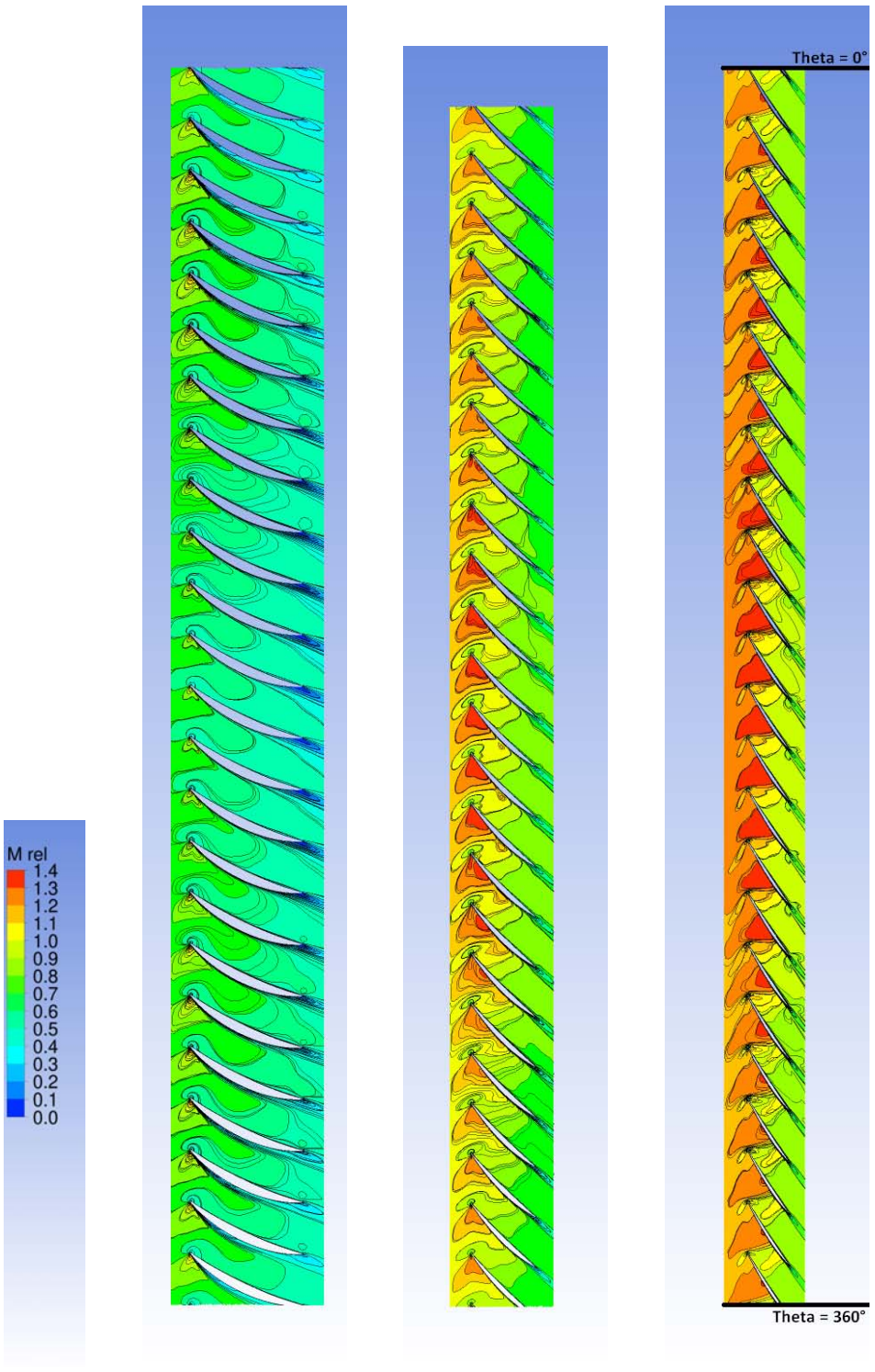

(a) (b) 20% span (c) 50% span (d) 80% span

FIGURE 7.15: Contour of M_{rel} at different span

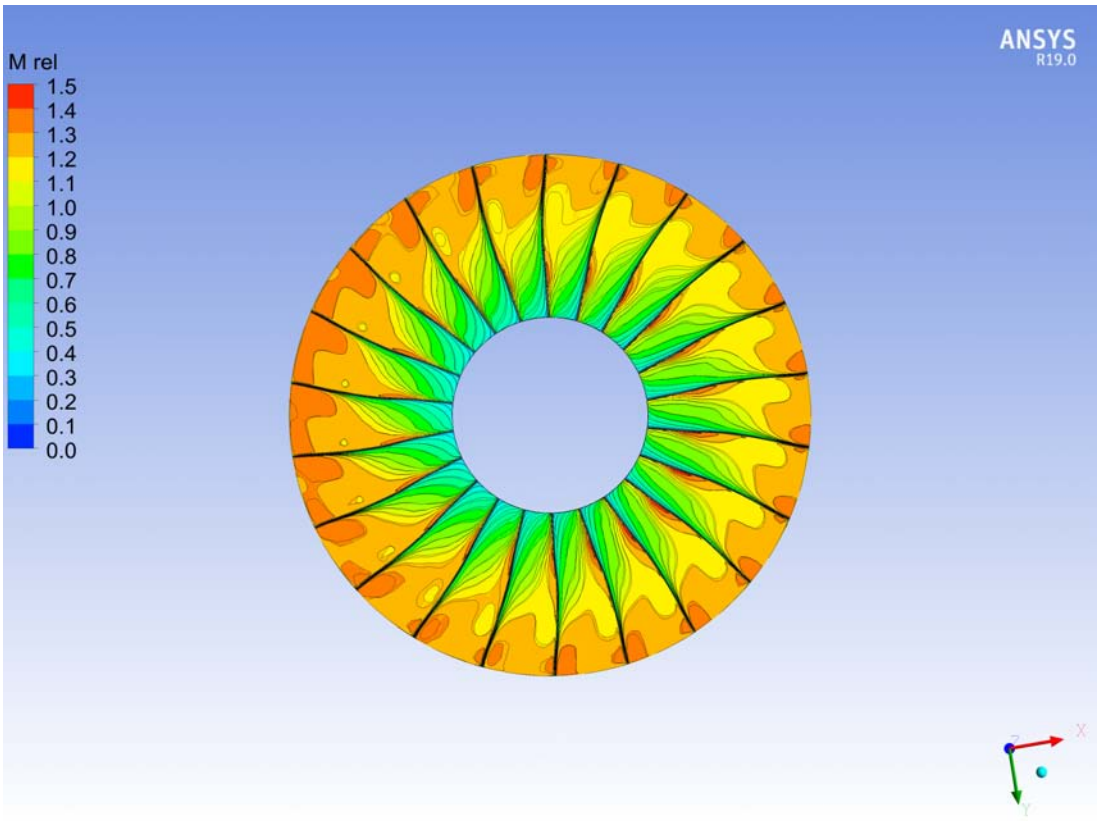

FIGURE 7.16: Relative Mach at blade LE

In the pictures above it is possible to see in detail the operation of the blade. Fig. 7.15 and Fig. 7.16 are of particular interest from which it is possible to see the position of the shock wave and the progress of the relative match along the span of the blade. The oblique shock wave near the tip is similar to the baseline, except for the slightly greater obliquity, which induces less shock losses. Despite this, a weaker second-pass shock on the pressure side, as can be seen in Fig. 7.15, reduced the effect of the first shock causing the efficiency to be higher than the basis. In this case, the interaction between the boundary layer and the shock wave is not as serious as that which will be seen in the following case and is similar to that of the baseline. The sweep introduced influenced the position of the first shock wave, which consequently increased its obliquity with respect to the incoming flow, thus reducing the shock losses. Finally, in the internal area near the hub, also the remodelling of the aerodynamic profile, through a softer rear camber, has contributed to reducing the losses in the flow, guaranteeing higher efficiency.

7.4 Best π_c

Analysing in detail the blade that returned the highest compression ratio as a result, we can see that this is much more loaded than the other two, which is why this high increase occurred. The blade has a modification of both the camber and the maximum thickness along the entire span. The stacking line also has substantial differences from the baseline. This remodelling was responsible for the increase in load. On the other hand, there have been many flow losses that have compromised polytropic efficiency. These high losses result mainly from the position of the shock wave.

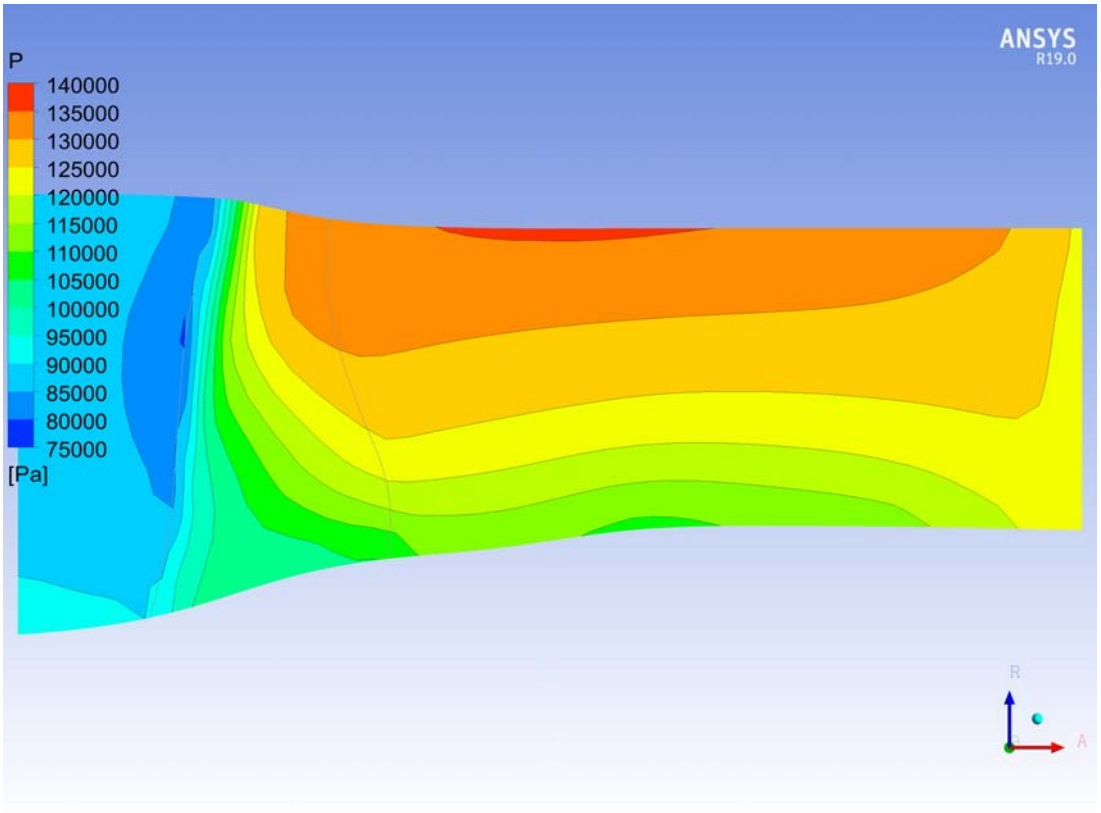

FIGURE 7.17: Static Pressure along the span

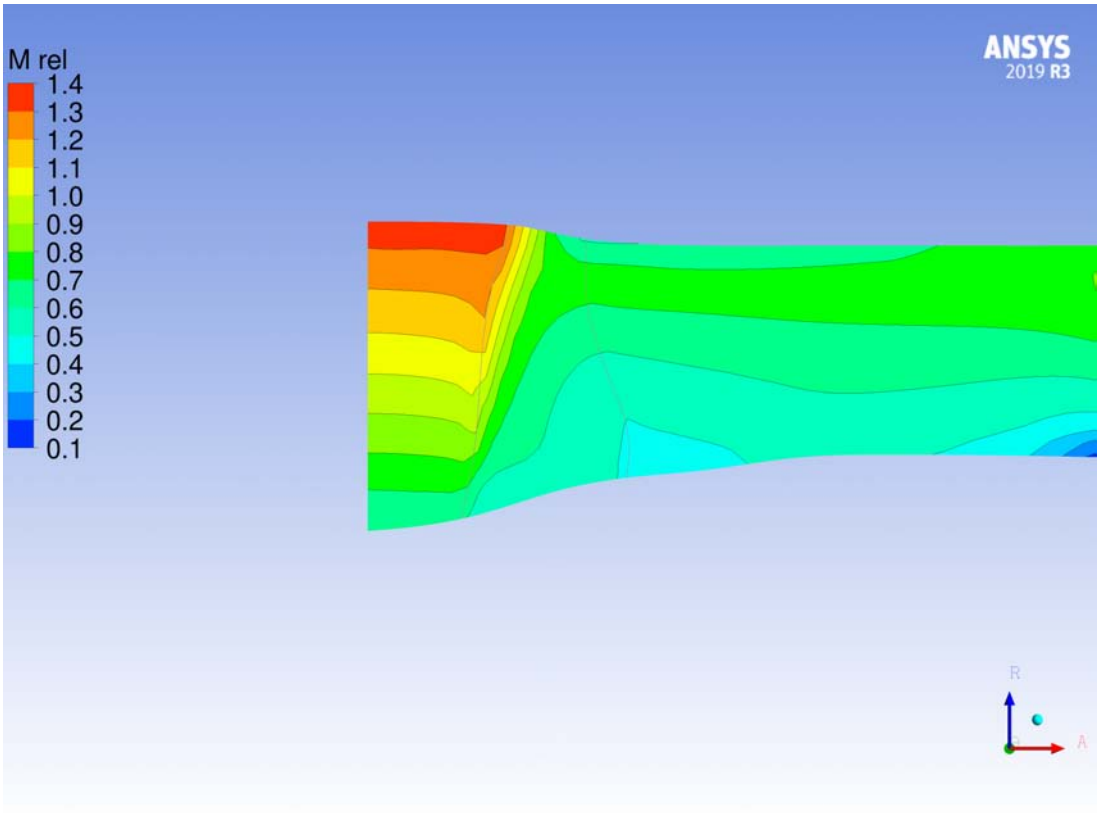

FIGURE 7.18: Relative Mach along the span

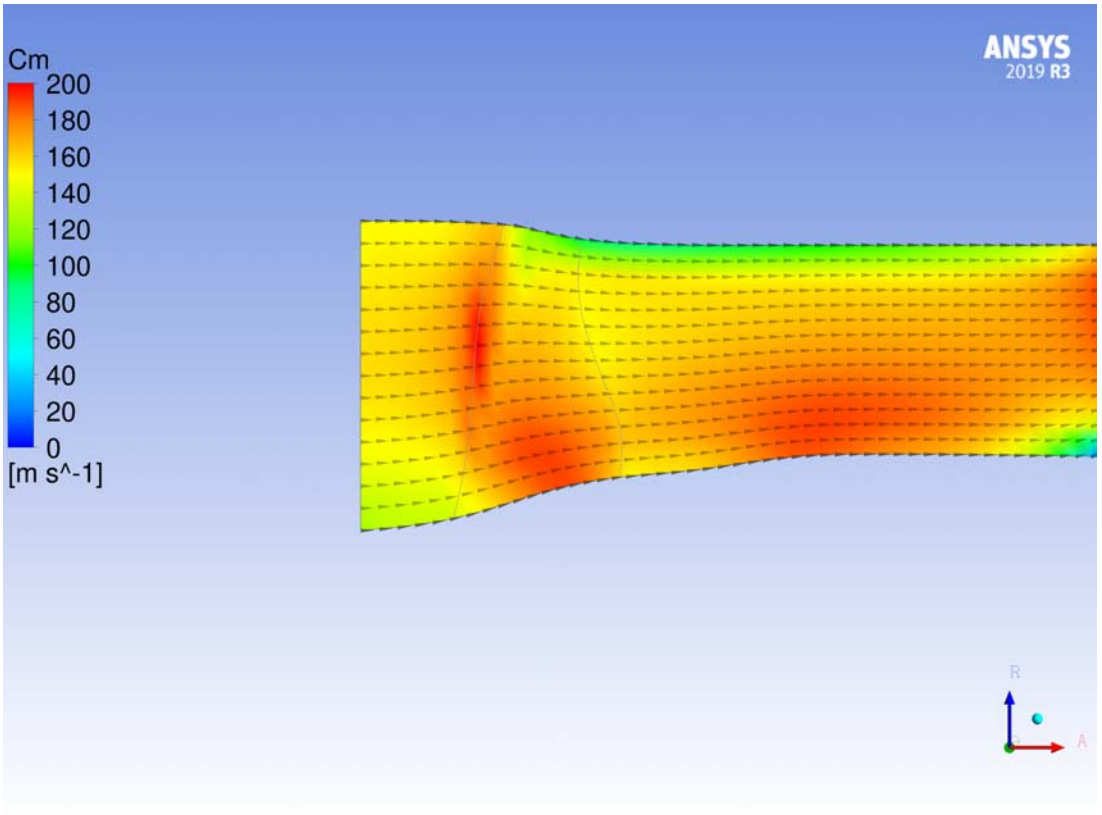

FIGURE 7.19: Cm along the span

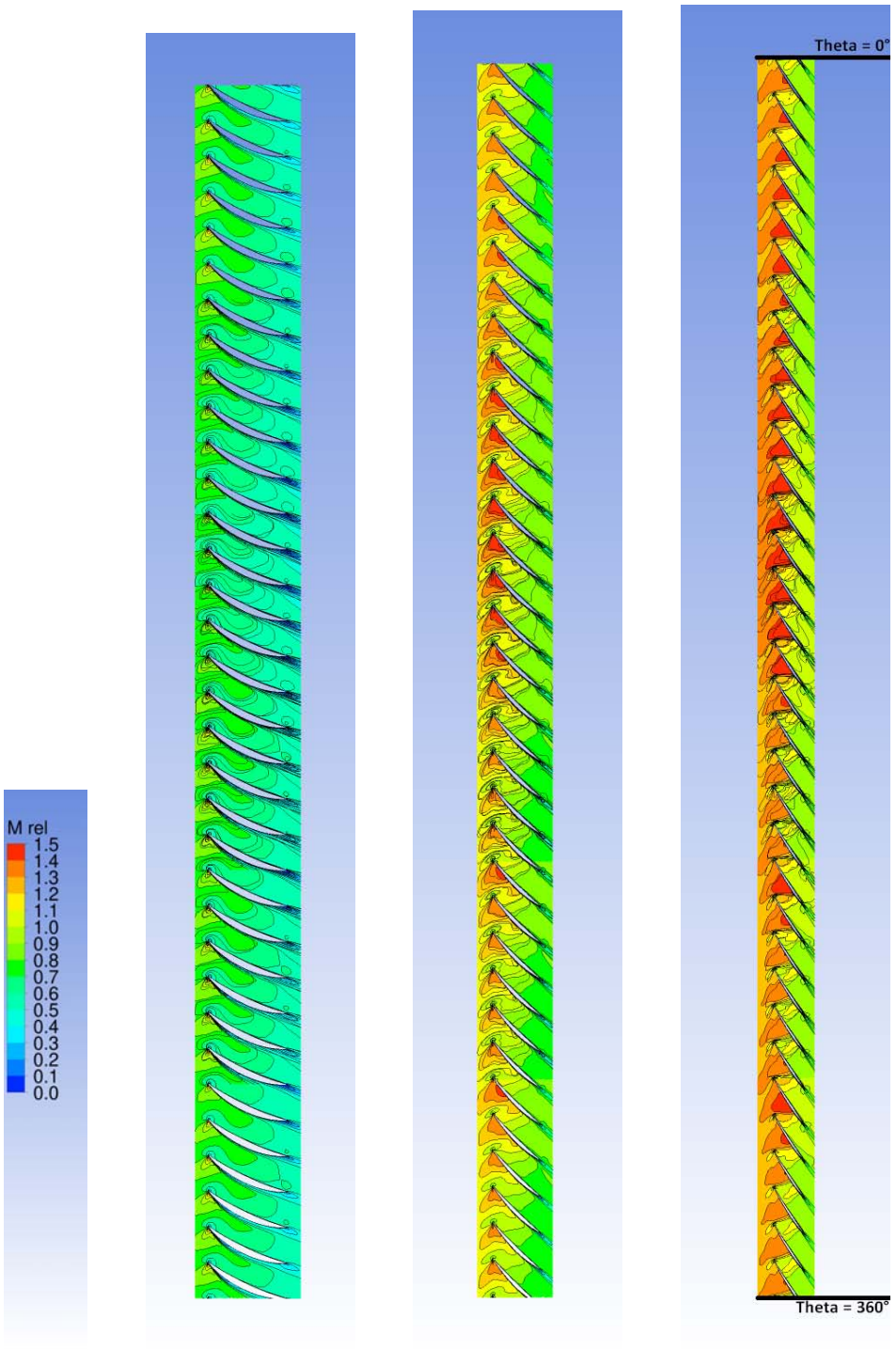

(a) (b) 20% span (c) 50% span (d) 80% span

FIGURE 7.20: Contour of M_{rel} at different span

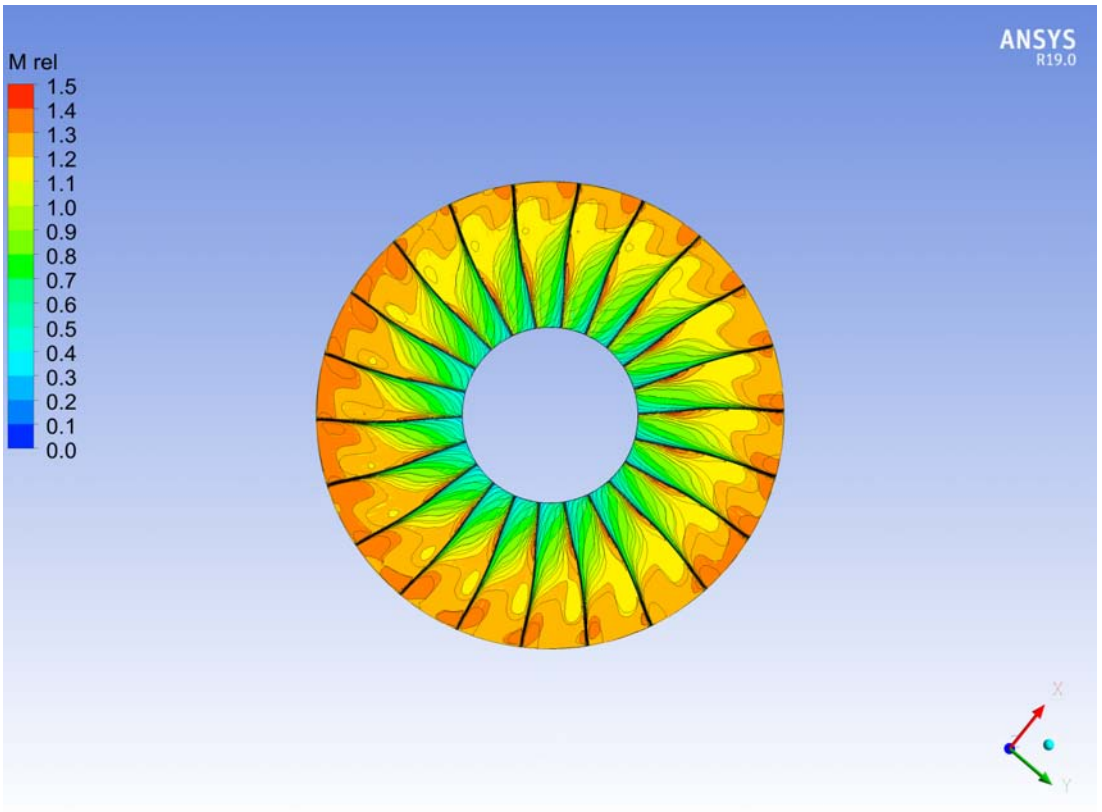

FIGURE 7.21: Relative Mach at blade LE

In the images above it is possible to see in detail the operation of the blade. Fig. 7.20 and Fig. 7.21 are of particular interest from which it is possible to see the position of the shock wave and the progress of the relative match along the span of the blade. Compared to the baseline, the analysed blade has a stronger passing shock wave near the tip. This shock, in fact, is detached from the leading edge of the blade and has an almost normal inclination with respect to the incoming flow. As you can see, the interaction between the severe impact and the boundary layer of the suction side has generated a detachment of the boundary layer with consequent very high losses. Furthermore, there was no further spread of subsonic flow after near normal shock.

7.5 Trade-off

Finally, by analysing the compromise solution it is possible to see how there are significant differences compared to the previous cases. The change in geometry affected both the stacking line and the shape of the profiles. The lean gave, as in the case of the first analysis, an S-shaped profile to the leading edge of the blade. Starting from the hub, in fact, the inclination comes first towards the middle of the span and then backwards. In addition, near the tip you can see a strong deformation in the direction of rotation. As for the sweep, the blade has a large sweep forward from the half-span hub and then has a sweep backwards on the tip. Finally, in the hub section a higher camber and a slightly greater thickness was observed compared to the original design. All these deformations have decreased the flow losses and reduced the intensity of the shock waves, which is the reason why polytropic efficiency has increased. The compression ratio has also raised and this is due to the higher load to which the blade is subjected compared to the baseline. The result is therefore satisfactory to what has been sought. An improvement, albeit slight, of the two objective functions analysed was obtained.

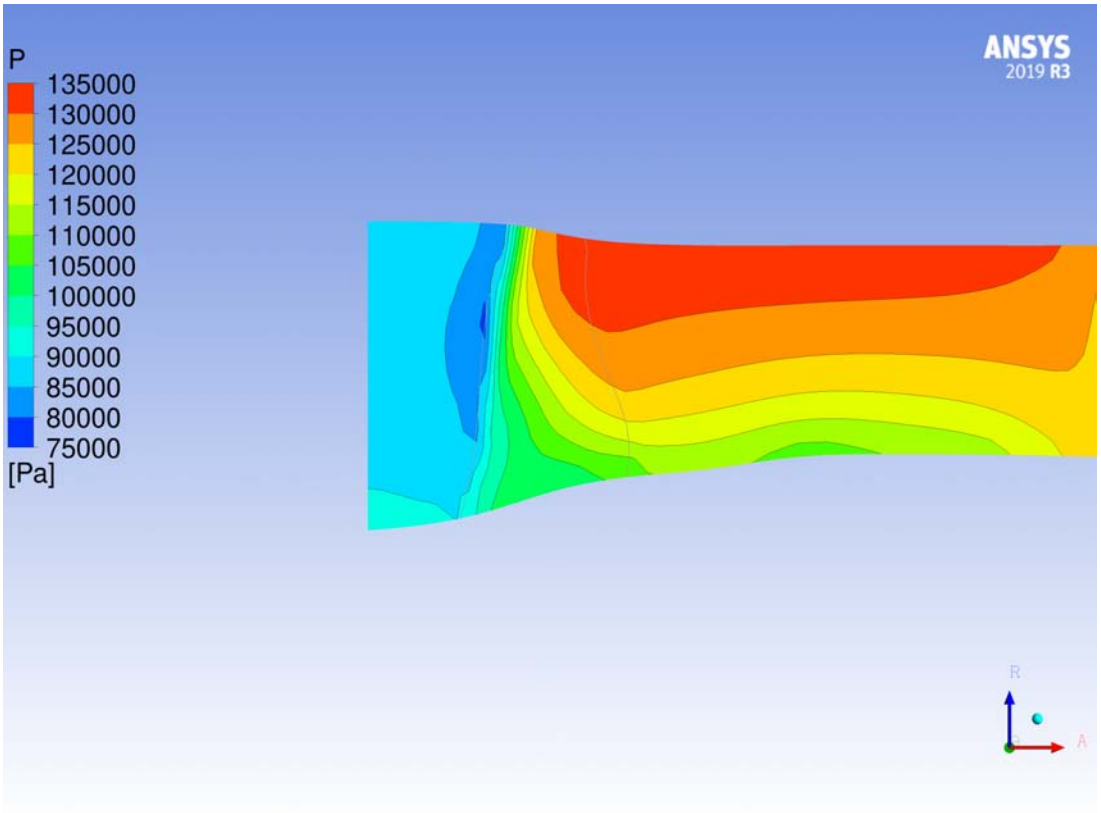

FIGURE 7.22: Static Pressure along the span

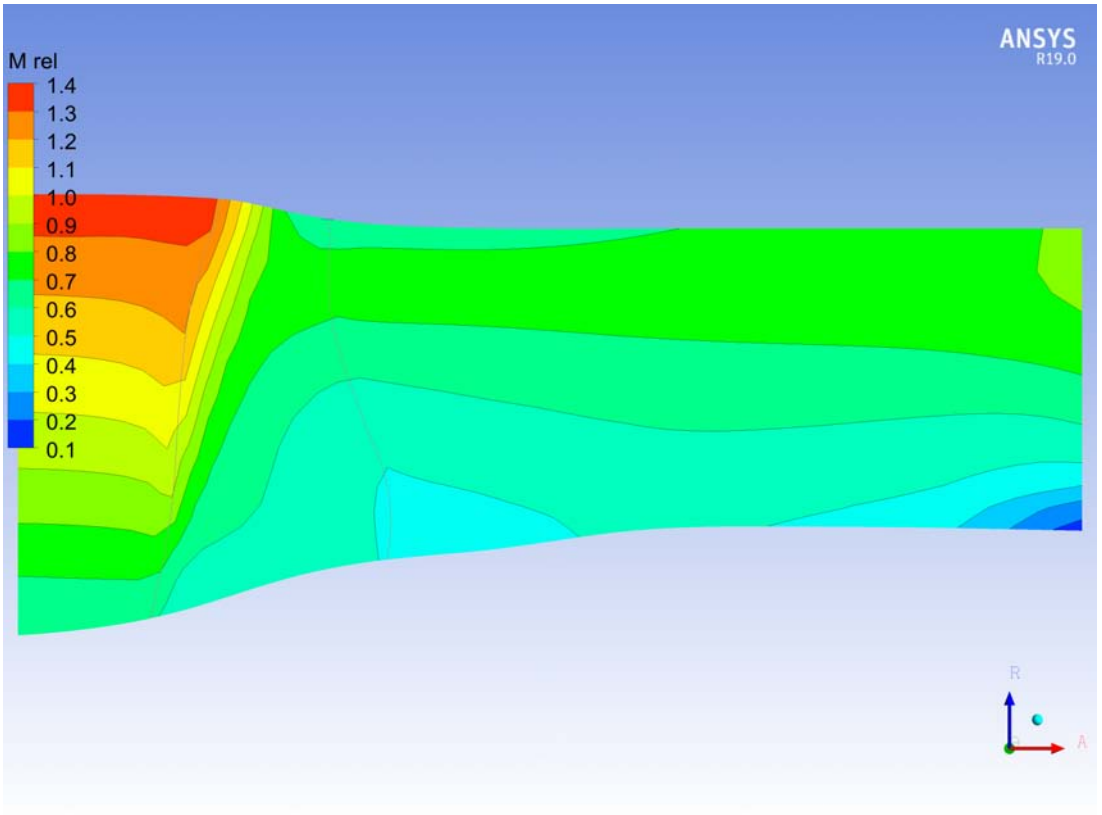

FIGURE 7.23: Relative Mach along the span

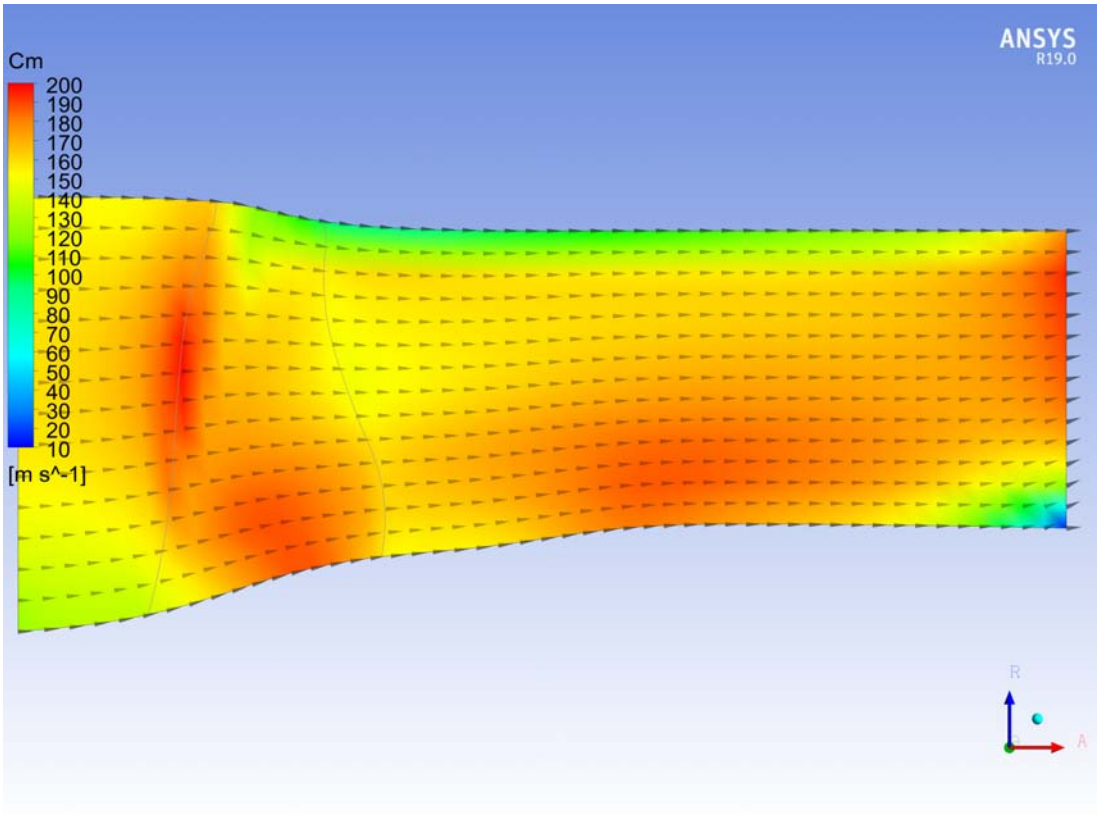

FIGURE 7.24: Cm along the span

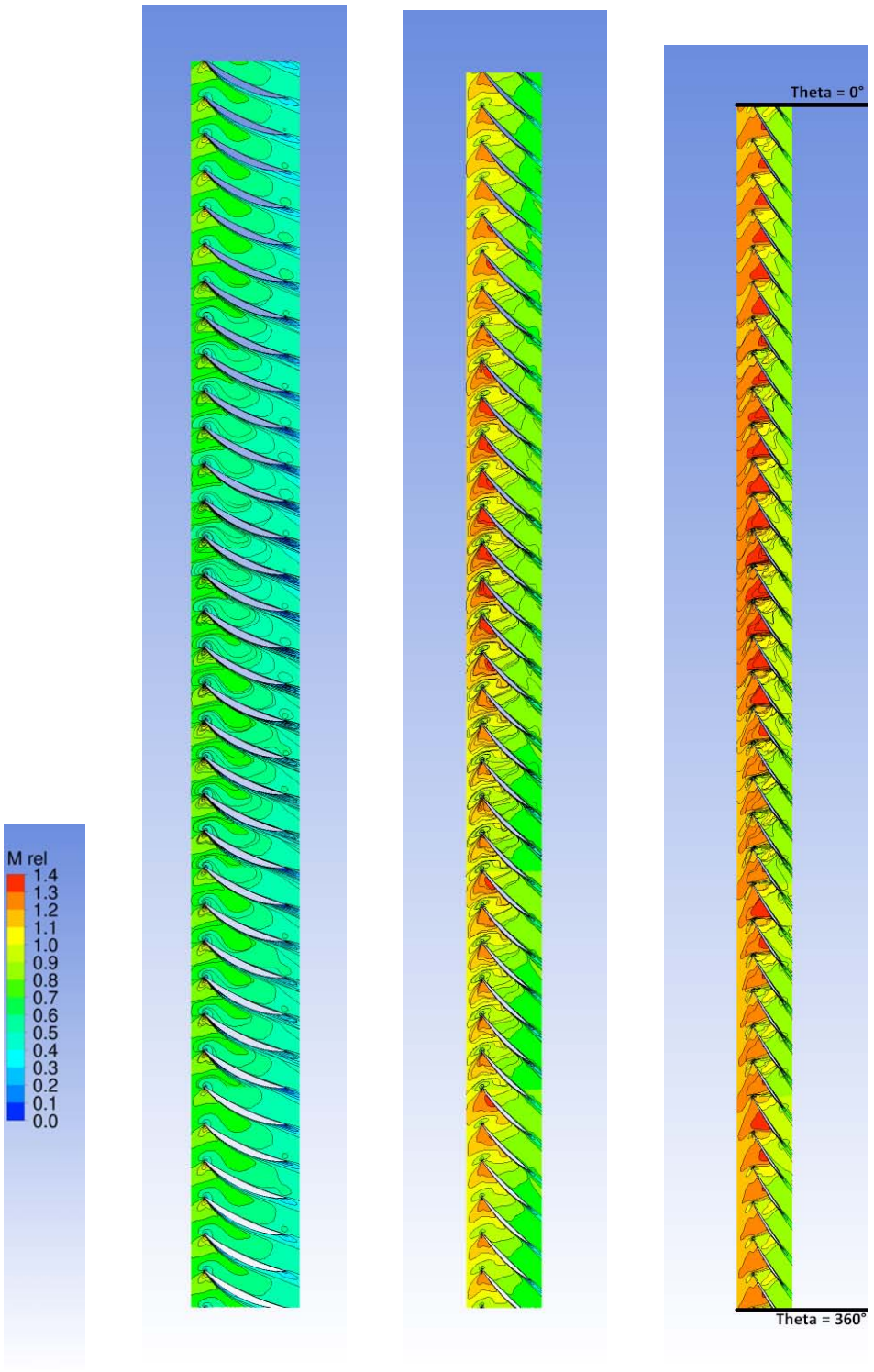

(a) (b) 20% span (c) 50% span (d) 80% span

FIGURE 7.25: Contour of M_{rel} at different span

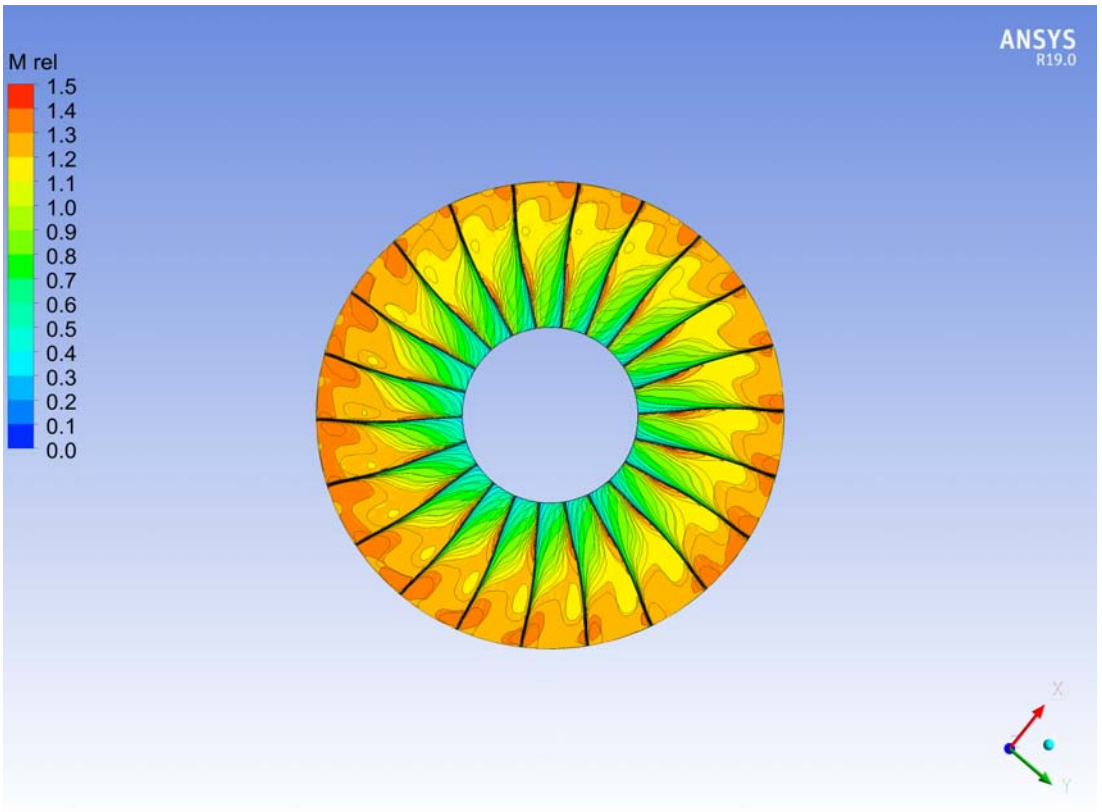

FIGURE 7.26: Relative Mach at blade LE

In the pictures above it is possible to see in detail the operation of the blade. Fig. 7.25 and Fig. 7.26 are of particular interest from which it is possible to see the position of the shock wave and the progress of the relative match along the span of the blade. The oblique shock wave near the tip is similar to the baseline and very similar to geometry with maximum efficiency. The difference from the latter is that the obliquity of the shock wave is slightly less, thus causing greater shock losses. In this case, the interaction between the boundary layer and the shock wave is not as serious as that which occurred for the geometry with maximum compression ratio. The interaction, in fact, is similar to that of the baseline. The sweep introduced, as for the first geometry analysed, is the main reason for the variation of the position of the shock wave and thanks to this variation the losses have been reduced. In fact, the shock wave occurs in an optimal position. Finally, thanks to the modification of the geometry, it is possible to notice how the load has increased along the span of the blade, increasing the compression ratio.

Chapter 8

Conclusion and Future Work

Multi-objective optimization of the blade shape of the NASA Rotor 67 has been successfully performed using an optimizer based on the use of the genetic algorithm combined with a CFD solver. The polytropic efficiency and the total pressure ratio, which were the two objective functions, were maximized at a specific mass flow condition. As it is possible to see, a complete and deep remodelling of the rotor geometry has been achieved thanks to the use of a generalized parameterization structure, which has involved sweep and lean deformations, as well as the modification of the blade sections. As previously mentioned, this parameterization was created and validated by Venturelli [12] during his PhD work. Due to the limited number of CFD assessments, due to the limited time available and the enormous computational cost of the system, the Pareto Front was grouped in a restricted region. Two geometries have distanced themselves from this region. The first geometry has a high compression ratio and a low value of polytropic efficiency. The second geometry, on the contrary, has a high polytropic efficiency value and a low compression ratio value. From the results obtained, three projects were analysed, two of them representative of the maximization of each objective and the third representative of a compromise solution. The results confirm the fact that the optimization process requires many CFD analyses to achieve high- level results. Unfortunately, the computational power was too low for this job and the time available was short. However, the optimal geometries obtained from the created optimization process provide a snapshot of the mechanisms involved in transonic compressors, demonstrating the effectiveness of the entire optimization strategy. Therefore, despite the presence of the s-duct, which complicates the system considerably, it has been shown that an accurate optimization process leads to an

improvement in the overall performance of the fan. The improvements are not large and probable further analyses will not lead to a noteworthy result. Since the system is very complex, in fact, the time required, due to the high computational cost, could be excessive before obtaining a concrete improvement. Furthermore, since the NASA Rotor 67 is already a fan optimized by itself, the chances of considerably improving its performance are very low. Certainly, this enormous work has been of great help in understanding the functioning of the rotor itself and in highlighting the actual potential of the optimization processes. The optimization carried out has only minimally taken into account the structural parameters of the blade and had the sole purpose of improving the selected objective functions. Therefore, it is possible that the geometries obtained are not usable in the practical act, but require more specific studies regarding their solidity and their construction process.

In the future, if there were the possibility of using more powerful means of calculation, it could be interesting to evaluate further analyses and therefore further geometries, perhaps also evaluating other objective functions such as the construction parameters or the operational stresses to which a blade is subjected during the its functioning.

Bibliography

[1] Philip Hill and Carl Peterson. *Mechanics and Thermodynamics of Propulsion*. Wesley Publishing Co., 1992.

[2] Ernesto Benini. *Propulsione Aerea*. Cleup, 2014.

[3] Kevin Brendan Cramer. *Design of a total pressure distortion generator for aircraft engine testing*. PhD thesis, Virginia Tech, 2002.

[4] Ernesto Benini. Dispense del corso di progetto di macchine. .

[5] Jr Anderson and John David. *Fundamentals of aerodynamics*. Tata McGraw-Hill Education, 2010.

[6] Roberto Biollo and Ernesto Benini. Recent advances in transonic axial compressor aerodynamics. *Progress in Aerospace Sciences*, 56:1–18, 2013.

[7] Kenneth L Suder. Blockage development in a transonic, axial compressor rotor. In *ASME 1997 International Gas Turbine and Aeroengine Congress and Exhibition*, pages V001T03A059–V001T03A059. American Society of Mechanical Engineers, 1997.

[8] Saeed Farokhi. *Aircraft Propulsion*. John Wiley & Sons Ltd, 2014.

[9] A. R. Howell and M.A. Fluid dynamics of axial compressors. *SAGE Journal*, 1945.

[10] Anthony J. Strazisar, Jerry R. Wood, Michael D. Hathaway, and Kenneth L. Suder. Laser anemometer measurements in a transonic axial-flow fan rotor. *NASA Technical Paper 2879*, 1989.

[11] Rodrick V. Chima. Viscous three-dimensional calculations of transonic fan performance. *Journal of Turbomachinery*, 1991.

[12] Venturelli Giovanni. Development of numerical procedure for turbomachinery optimization. 2013.

[13] D. Dal Magro. Implementation of uncertainty management techniques in the design of s-ducts intakes. Master's thesis, Universitá degli Studi di Padova, 2019.

[14] C.A. Hah. Numeric modeling of endwall and tip-clearance flow of an isolated compressor rotor. *Jounral Eng. Gas Turbines Power*, 108(1), 1986.

[15] Alberto Meneghin. Three-objective optimization studies of an s-duct. Master's thesis, Universitá degli Studi di Padova, 2020.

[16] Kypros Milidonis, Bernhard Semlitsch, and Tom Hynes. Effect of clocking on compressor noise generation. *AIAA Journal*, 56(11):4225–4231, 2018.

[17] Roberto Biollo and Ernesto Benini. State-of-art of transonic axial compressors, advances in gas turbine technology. *ISBN*, pages 978–953, 2011.

[18] Ernesto Benini. Dispense del corso di propulsione aerea. .

[19] Abate Giada. Aerodynamic optimization of a transonic axial compressor rotor. 2012.

[20] A. K. Sehra and J. L. Kerrebrock. Blade-to-blade flow effects on mean flow in transonic compressors. *AIAA Journal*, 19, 1981.

[21] William Rede Hawthorne. Secondary circulation in fluid flow. *Proceedings of the Royal Society*, 1951.

[22] H. B. Squire and K. G. Winter. The secondary flow in a cascade of airfoils in a nonuniform stream. *AIAA Journal*, 18, 1951.

[23] J. L. Kerrebrock and A. A. Mikolajczak. Intra-stator transport of rotor wakes and its effect on compressor performance. *Journal of Engineering for Gas Turbines and Power*, pages 359–368 (10 pages), 1970.

[24] Marco Tridente. Cfd study on the effect of a transonic fan downstream of an s-shape duct. Master's thesis, Universitá degli Studi di Padova, 2019.

[25] ANSYS Inc. Introduction to ansys fluent, turbulence modeling.

[26] James H. Page, Paul Hield, and Paul G. Tucker. Effect of inlet distortion features on transonic fan rotor stall. *Journal of Turbomachinery*, 140(7): 071008 (11 pages), 2018.

[27] A Naseri, M Boroomand, and S Sammak. Numerical investigation of effect of inlet swirl and total-pressure distortion on performance and stability of an axial transonic compressor. *Journal of Thermal Science*, 25(6):501–510, 2016.

[28] Nicholas Fredrick and Milt Davis. Investigation of the effects of inlet swirl on compressor performance and operability using a modified parallel compressor model. In *ASME 2011 Turbo Expo: Turbine Technical Conference and Exposition*, pages 177–187. American Society of Mechanical Engineers, 2011.

[29] *A Comparison of Several CFD Codes with Experimental Data in a Diffusing S Duct*, 2006.

[30] Steven R. Wellborn, Bruce A. Reichert, and Theodore H. Okiishi. A study of the compressible flow in a diffusing s-duct. Technical report, NASA, 1993.

[31] Andrea Scaramuzzi. Robust design optimisation of s-ducts under uncertainties. Master's thesis, Universitá degli Studi di Padova, 2020.

[32] F. Glover. Tabu search: Part i. *ORSA Journal on Computing*, 1(3):190–206, 1989.

[33] C. Blum and A.Roli. Metaheuristics in combinatorial optimization: Overview and conceptual comparison. *ResearchGate*, 2003.

[34] Jun Li, Hiroshi Tsukamoto, and Nobuyuki Satofuka. Optimization of aerodynamic design for cascade airfoil by means of boltzmann selection genetic algorithms. 2(1):864, 2000.

[35] J. Harinck, Z. Alsalihi, J. P. Van Buijtenen, and R. A. Van den Braembussche. Optimization of a 3d radial turbine by means of an improved genetic algorithm. pages 1003–1042, 2005.

[36] K. C. Giannakoglu and M. K. Karakasis. Hierarchical and distributed metamodel-assisted evolutionary algorithms. pages 111–145, 2006.

[37] M. K. Karakasis, K. C. Giannakoglu, and D. G. Koubogiannis. Aerodynamic design of compressor airfoils using hierarchical, distributed, metamodel- assisted evolutionary algorithms. 2007.

[38] J. Periaux, L. F. Gonzalez, and D. S. Lee. Moo methods for multidisciplinary design using parallel evolutionary algorithms, game theory and hierarchical topology: Theoretical aspects. 2010.

[39] A. Oyama, M.S. Liou, and S. Obayashi. Transonic axial-flow blade shape optimization using evolutionary algorithm and three-dimensional navier-stokes solver. *Journal of Propulsion and Power*, 20:612–619, 2004.

[40] S. Pierret. Multi-objective and multi-disciplinary optimization of three-dimensional turbomachinery blades. 2005.

[41] Y. Lian and M.S. Liou. Multiobjective optimization using coupled response surface model and evolutionary allgorithm. 43(6):1316–1325, 2005.

[42] Y. Lian and N.H. Kim. Reliability-based design optimization of a transonic compressor. 44(2):368–375, 2006.

[43] H. Okui, T. Verstraete, R.A. Van De Braembussche, and Z. Alsalihi. Three-dimensional design and optmization of a transonic rotor in axial flow compressors. *Journal of Turbomachinery*, 135, 2013.

[44] J. Luo, C. Zhou, and F. Liu. Multipoint design optimization of a transonic compressor blade by using an adjoint method. *Journal of Turbomachinery*, 13, 2014.

[45] H. Watanabe and M. Zangeneh. Design of the blade geometry of swept transonic fans by 3d inverse design. 2003.

[46] W.T. Tiow and M. Zanageneh. Application of a three-dimensional viscous transonic inverse method to nasa rotor 67. *Journal of Power and Propulsion*, 216:143–255, 2002.

[47] P. Hu, B. Choo, M. Zangheneh, and M. Rahmati. On design of transonic fan by 3d inverse design method. 2006.

[48] C.H. Law and A.R. Wadia. Low aspect ratio transonic rotors: Part2: Influence of location of maximum thickness on transoinc compressor performance. *Journal of Turbomachinery*, 115:226–239, 1993.

[49] C.A. Hah and A.J. Wennerstrom. Three-dimensional flow field inside a transonic compressor with swept blades. *Journal of Turbomachinery*, 113:241–251, 1991.

[50] A.R. Wadia, P.N. Szucs, and D.W. Crall. Inner workings of aerodynamic sweep. *Journal of Turbomachinery*, 120:671–682, 1998.

[51] C.A. Hah, S.L. Puterbaugh, and A.R. Wadia. Control of shock structure and secondary-flow field inside transonic compressor rotors through aerodynamic sweep. 1998.

[52] J.D. Denton and L. Xu. The effects of lean and sweep on transonic fan performance. *Journal of Turbomachinery*, 2002.

[53] T. Sasaki and F. Breugelmans. Comparison of sweep and dihedral effects on compressor cascade performance. *Transaction of the ASME*, 120:454–463, 1998.

[54] A. A. Giunta and L. T. Watson. A comparison of approximation modeling techniques: Polynomial versus interpolating models. pages 392–404, 1998.

[55] C.S. Ahn and K.Y. Kim. Aerodynamic design optimization of a compressor rotor with navier-stokes analysis. 217(2):179–184, 2003.

[56] E. Benini. Three-dimensional multi-objective design optimization of a transonic compressor rotor. *Journal of Propulsion and Power*, 20(3):559–565, 2004.

[57] C.H. Law and A.R. Wadia. Aerodynamic of swept and leaned transonic compressor-rotors. *Applied Energy*, 84:1012–1027, 2007.

[58] E.M. Mortenson. *Geometric Modeling*, volume Second edition ed. John Wiley & Sons, 1997.

Appendix A

Optimization Framework

The automatic optimization framework is responsible for leading the automatic and reliable optimization process. The aim is to predict any type of noise, internal such as errors from loop programs and external such as problems such as crashes. The entire framework was developed by Venturelli [12] in MATLAB®, Bash scripting and C code, and was subsequently adapted and modified by the author to adapt to the required task. As part of this work, the general conceptual strategy can be summarized in the flow chart shown in Fig. A.1.

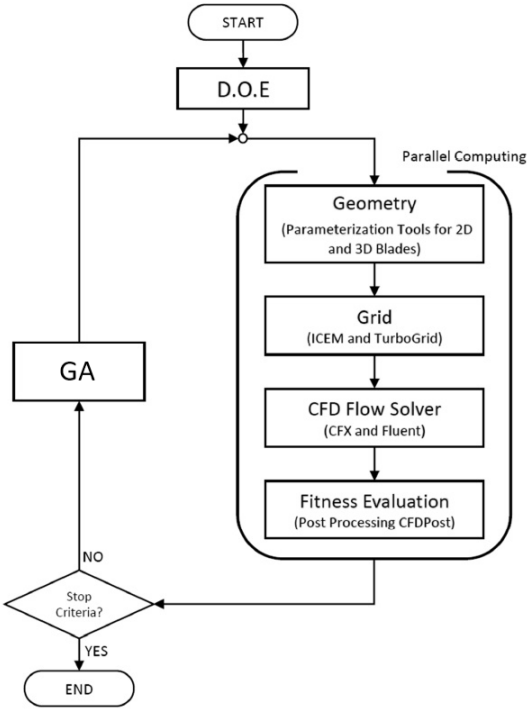

FIGURE A.1: Optimization conceptual strategy

It is composed by a starting procedure as the D.O.E., an optimization engine that is the GA, and the evaluation of the design fitness. The realization of such conceptual strategy in the Delta cluster is reported in the flow chart of Fig. A.2. Each of the three built levels is independent of the others so that an error in one level does not affect the functioning of the others. In particular, the characteristics of the levels are as follows:

- Level 0: refers to the optimization algorithm, which outputs new designs to be evaluated ("Population") and waits for their response ("Fitness")
- Level 1: the "Exchange pool" is the link between the optimizer and the hard computing environment. It represents the locus where requests of the optimization algorithm are converted to design evaluation procedures, in order to calculate design fitness and, in turn, satisfy the algorithm's request
- Level 2: calculations are performed in parallel on the Delta cluster of the University of Cranfield exploiting all available computational power

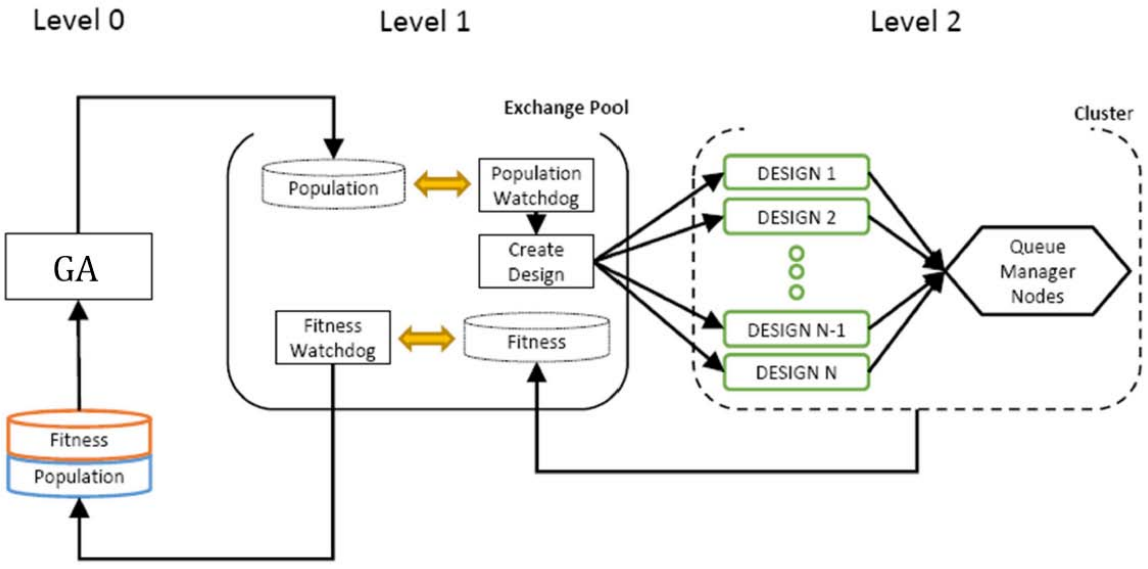

FIGURE A.2: Optimization framework layout

In Fig. A.3 is possible to see how design fitness evaluation is made. The box called "watchdog" is a looped process linked to the most critical process that needs to be monitored. The watchdog lasts until the critical process ends. The purpose of a watchdog is to control and handle any type of error by taking appropriate action. Once each critical process has its own custom watchdog, you can start the optimization process.

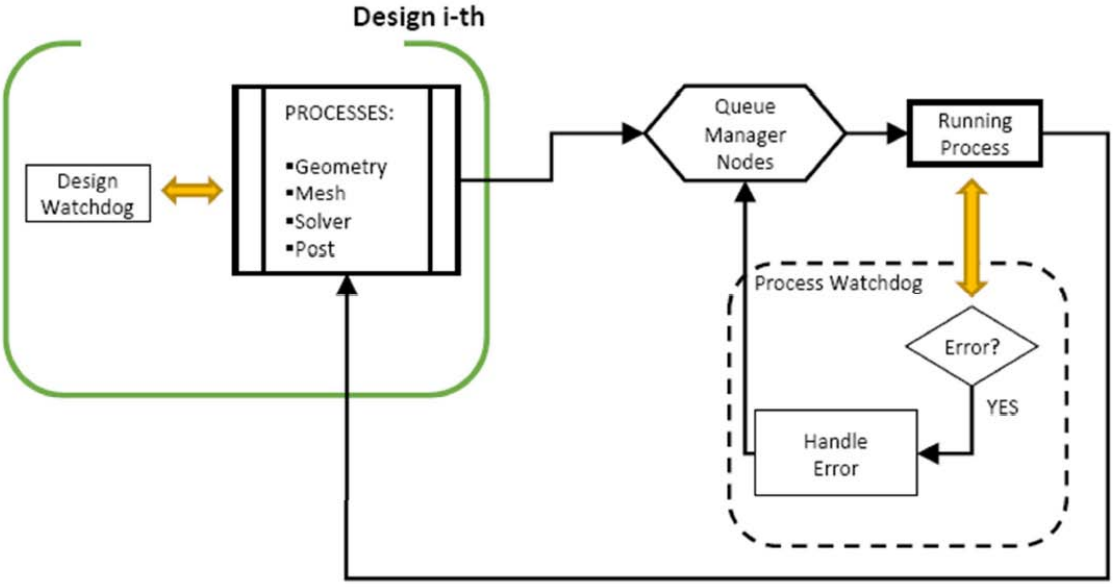

FIGURE A.3: Flowchart Detail of a single design